Final Report

Project[a]:

"Interaction and transport of Actinides in natural clay systems in the presence of humic substances and clay organic matter"

Subproject[b] 6:

"Molecular process understanding of interactions between Lanthanide ions and components of homogeneous and heterogeneous saline systems"

K. Brennenstuhl, K. Burek, S. Eidner, M.U. Kumke[#]

University of Potsdam, Institute of Chemistry, Physical Chemistry

Karl-Liebknecht-Str. 24-25, 14476 Potsdam-Golm

[#]kumke@uni-potsdam.de

[a]Deutscher Titel: Rückhaltung endlagerrelevanter Radionuklide im natürlichen Tongestein und in salinaren Systemen

[b]Deutscher Titel: Teilprojekt 6: Zum molekularen Prozessverständnis der Wechselwirkungen von Lanthanoidionen mit Komponenten homogener und heterogener salinarer Systeme

Das diesem Bericht zugrunde liegende Vorhaben wurde mit Mitteln des Bundesministeriums für Wirtschaft und Technologie und dem Förderkennzeichen 02E11011 gefördert. Die Verantwortung für den Inhalt dieser Veröffentlichung liegt bei den Autoren.

Das Forschungsvorhaben war ein Teilprojekt im Forschungsverbund „Rückhaltung endlagerrelevanter Radionuklide im natürlichen Tongestein und in salinaren Systemen“ und erfolgte in Kooperation mit folgenden Institutionen:

Helmholtz-Zentrum Dresden-Rossendorf, Institut für Ressourcenökologie

Karlsruher Institut für Technologie, Institute für Nukleare Entsorgung

Johannes Gutenberg-Universität Mainz, Institut für Kernchemie

Universität des Saarlandes, Institut für Anorganische und Analytische Chemie und Radiochemie

Technische Universität Dresden, Sachgebiet Strahlenschutz, Professur Radiochemie

Universität Heidelberg, Physikalisch Chemisches Institut

Technische Universität München, Fachgebiet Theoretische Chemie

Abstract

In the project processes related to the fate of radionuclides at high ionic strength *I* (0 mol·L^{-1} < *I* < 4 mol·L^{-1})[c] in clay and salt host rock formations, which are typical for the northern part of Germany, were investigated for temperatures *T* < 353 K using optical spectroscopic methods. The fundamental process understanding, which is necessary for the full exploitation of the analytical data, and the improvement as well as the development of analytical (spectroscopic) "tools" were key aspects of the work performed. In the experiments Lanthanide(III) (Ln(III)) ions were used as natural analogs and were investigated using laser-based spectroscopic techniques, especially time-resolved laser fluorescence spectroscopy (TRLFS) and Raman spectroscopy complemented with sum frequency generation (SFG) spectroscopy. Especially Raman and SFG spectroscopy were used to characterize clay mineral surfaces and interlayers of such for structural effects of Ln(III) ions and low molecular weight organic compounds. Potential organic ligands originating for the clay minerals were investigated. Here, naturally occurring polymers such as humic substances (HS) and low molecular weight organics (LMWO) were investigated. In order to bridge the gap between HS and LMWO also synthetic polymers of a known composition were included in order to consider effects that are related to the macromolecular character of HS. In this context in order to mimic certain properties, a novel polymer (polyvinyl benzoic acid) at two different molar weights was synthesized. In the experiments the influence of the temperature and of the overall background concentration (ionic strength) as well as chemical properties (Na vs. Ca, Mg) were elucidated. In addition to organic ligands also borate as a potential inorganic component in the repository was investigated. For the organic ligands on the one hand side the intrinsic fluorescence was evaluated to determine the complexation of different Ln(III) ions and on the other hand side the luminescence of the Ln(III) was analyzed. The sorption on clay mineral surfaces and the complexation with low molecular weight organic ligands and borate as well as model and natural polymers (e.g., HS) were investigated using different Ln(III) ions as luminescence probes. Especially Europium(III) (Eu(III)) was applied as a luminescence probe due to its outstanding sensing capabilities. The analysis of the spectral luminescence intensity distribution revealed difference in the binding by HS and was used in combination with site-selective excitation to identify the presence of different complexes in the sample. Here, especially measurements at ultra low temperatures proofed to be very valuable due to the outstanding spectral resolving power in the identification of different polyborate complexes. From the luminescence data conditional binding constants and their variation with temperature and ionic strength were determined. Moreover, using different excitation schemes for starting the luminescence mechanistic details on the complexation of Ln(III) by organic ligands and effects of different ions used as background electrolytes were evaluated. While under direct excitation conditions an overall luminescence signal was obtained containing possible contributions from non-complexed Ln(III) ions, a sensitized excitation using the ligand as "light collector" yielded only information on the bound

[c] 0 mol·L^{-1} means no additional ion were added, ionic strength is determined by the concentration of the Ln(III)

part. The data were further evaluated for differences in binding sites using competition experiments with other ions such as Ca(II) and Mg(II) in combination with the NICA Donnan model. For the determination of the average distance between bound Ln(III) ions the inter-lanthanide energy transfer (ILET) was applied as a method of choice for distance determinations in the intermediate range of several nanometers. The ILET was applied to different organic polymer as well as to clay mineral samples. For the ILET a couple of Ln(III) ions, one acting as energy donor and the other as the acceptor, are bound in/on the sample. From the distance (= degree of loading) dependence of the donor luminescence, the average distance of bound metal ions was calculated. The interplay between different lanthanide- and ligand-related radiationless deactivation pathways was investigated using different combinations of Ln(III) ions and low molecular weight organic ligands. In the combinations the Lanthanide specific parameters of energy gap between ground and electronically excited states as well as the redox potential were considered. For the ligands the energy of the ligand's triplet state and the redox potential were taken into account. In a systematic evaluation the contribution of the different parameters was determined. The results underline that a thorough understanding of the complex interplay between the ligand- and lanthanide-related electronic (molecular) properties is indispensible for a correct determination of macroscopic parameters such as binding constants. The effect of low molecular organic compounds on the surface and interfacial properties of clay minerals was investigated using Raman- and SFG spectroscopy. The intercalation of small organics in the interlayer could be clearly identified. The intercalation was determined from the alteration in the vibrational frequencies of different hydroxyl groups. Here, the special sensitivity of SFG spectroscopy and Raman microscopy were used to investigate these effects.

1. Introduction

According to a recent study of the BGR[1] clay layers of the Early Cretaceous in Northern Germany are potentially suited to host a deep underground repository for high level nuclear waste. Compared to clay layers so far investigated in other countries the geochemical boundary conditions are special with respect to the ionic strength and the salt concentration of the pore waters present. In contrast to clays investigated in Switzerland, Belgium or France the intrinsic ionic strength *I* of pore waters in Northern Germany is distintly higher (up to $I = 4\ mol \cdot L^{-1}$). A similar situation would also be found in the near field of salt rock formations, which is an alternative option for an underground repository in Germany, in case of water intrusion. This could start corrosion processes of the metal containers and the specific redox chemistry at high ionic strength conditions need to be understood in order to perform reliable model calculations. So high ionic strength is a key parameter to be taken into account in the risk assessment of potential nuclear waste repositories in Germany. However, the speciation of radionuclides under such high ionic strength conditions is hampered by the fact that the data base is lacking respective thermodynamic core data. Moreover, in the early stages of a repository the temperature in the near field may be distinctly elevated by the heat production of the waste materials (depending on the host rock formation the initial temperatures present can be as high as ~ 200°C for salt and ~ 100°C for clay).[1] In contrast to this particular condition the majority of the investigations were performed and the subsequent thermodynamic data were collected for room temperature conditions.

Therefore, the collaborative project was focused on fundamental process understanding related to the fate of radionuclides at high ionic strength *I* ($0\ mol \cdot L^{-1} < I < 4\ mol \cdot L^{-1}$)[c] in clay and salt host rock formations, which are typical for the northern part of Germany. The sorption to clay minerals at high ionic strength and at elevated temperature ($T < 353$ K) as well as the influence of different components present is the system was of interest. The complexation of Actinides (and Lanthanides as natural analogs) with borate and low molecular weight organic compounds in the presence high salt concentrations (NaCl, KCl, $MgCl_2$, $CaCl_2$) and at elevated temperatures was monitored. In the experiments complementary analytical techniques were used to tackle the challenge related to investigations of diffusion of Actinides, the redox chemistry under high ionic strength conditions and the influence of elevated temperature.

The work carried out at the University of Potsdam focused on the interactions between Ln(III) ions (e.g., Eu(III)) as chemical homologue for trivalent actinide ions – like Americium(III) or Curium(III)) with repository relevant inorganic (Borate) and organic ligands. As organic ligands small molecules such as formiate, acetate, or lactate as well as aromatic carboxylic acids, oligomers, and polymers as models for naturally occurring organics in clay minerals were taken into account. In the project Ln(III) ions were used as natural analogs and were investigated using laser-based spectroscopic techniques, especially time-resolved laser fluorescence spectroscopy (TRLFS) and Raman spectroscopy (complemented with sum frequency generation

spectroscopy). Ln(III) were applied as a luminescence probes due to their outstanding sensing capabilities. The sorption on clay mineral surfaces and the complexation with low molecular weight organic ligands and borate as well as model and natural polymers (e.g., humic substances) was investigated. In addition also the interaction of organic compounds and clay minerals was monitored by Raman microscopy and SFG spectroscopy to monitor the interactions between both from the ligand's point of view.

2. Experimental details

2.1 General experimental details

Lanthanide(III) complexes with model ligands

As model compounds for binding sites in HS, different (hydroxy)benzoic acids were investigated. The relative positions of the hydroxyl- and/or carboxyl group were systematically varied, in order to study the effect of complex formation and of the ligand structure on the luminescence spectra of different Ln(III) ions (Eu(III), Terbium (Tb(III)), Samarium (Sm(III)) and Dysprosium(Dy(III)). All reagents were of analytical grade. All chemicals were ordered from Sigma-Aldrich with the highest purity available.

Ln(III)-complexes with salicylic acid or phthalic acid (see Figure 1S)were prepared from aqueous (using Milli-Q water (Milli-Q Advantage A10, Merck)) stock solution of Ln(III)-salts ($TbCl_3 \cdot xH_2O$, $SmNO_3 \cdot 6H_2O$, $DyNO_3 \cdot 5H_2O$, $EuCl_3 \cdot 6H_2O$) and model ligands with a concentration of $c = 10^{-2}$ mol·L^{-1}. The concentrations as well as the molar ratio of Ln(III) ions and model ligands investigated are summarized in Table 1.

Table 1: Concentrations and molar ratio of Tb(III) /Sm(III) / Dy(III) and ligands.

	Molar ratio	*c* (Ln(III)) / mol·L^{-1}	*c* (ligand) / mol·L^{-1}
Tb(III) salicylic acid	1:99	$1.0 \cdot 10^{-4}$	$9.9 \cdot 10^{-3}$
Tb(III) phthalic acid	1:5	$1.0 \cdot 10^{-4}$	$5.0 \cdot 10^{-4}$
Sm(III) salicylic acid	1:45	$1.0 \cdot 10^{-4}$	$4.5 \cdot 10^{-3}$
Sm(III) phthalic acid	1:3	$1.0 \cdot 10^{-4}$	$3.0 \cdot 10^{-4}$
Dy(III) salicylic acid	1:45	$1.0 \cdot 10^{-4}$	$4.5 \cdot 10^{-3}$
Dy(III) phthalic acid	1:6	$1.0 \cdot 10^{-4}$	$6.0 \cdot 10^{-4}$

From speciation analysis (based on stability constants taken from literature (see Table 1S)) the molar ratios of the prepared solutions were calculated to the point where the solution contains the highest possible amount of Ln(III) complexes with one ligand (see Figure 2S). In Table 2S the calculated species distributions are shown.

The p*H* value was adjusted to a point at which the model ligand was in the single deprotonated form to ensure complexation with the Ln(III) ion. Furthermore, acid conditions were chosen to avoid the formation of Ln(III) hydroxyl complexes as well as carbonates. Speciation diagrams of the model ligands were calculated from pK_a values taken from literature (see Table 2S and Figure 3S). The p*H* of salicylic acid containing solutions was adjusted to 5.0 and of phthalic acid containing solutions to 4.2 with sodium hydroxide and hydrochloric acid. All solutions were stored in the fridge and soonest measured after five days to ensure an adjusted complex equilibrium.

For the Eu(III) solutions containing salicylic acid or phthalic acid as background electrolyte 0.1 mol·L^{-1} sodium perchlorate solution was applied. The concentration of Eu(III) was in both cases $c_{Eu(III)} = 5.7 \cdot 10^{-3}$ mol·L^{-1} and of the model ligands $3.4 \cdot 10^{-2}$ mol·L^{-1}. From speciation analysis based on stability constants taken from literature (see Table 1S) it was calculated that only a very minor concentration of the "free" Eu(III) aquo complex was present (see Table 2S and Figure 4S). To avoid formation of hydroxyl and carbonate complexes the p*H* was adjusted to five with sodium hydroxide and hydrochloric acid. Each solution was equilibrated for approximately five days prior to the luminescence measurements. The samples were stored in the dark at room temperature (RT).

Influence of ionic strength

Aqueous Ln(III) samples were prepared by solving Ln(III) salts in Milli-Q water. The variation of the ionic strength *I* (0.1 mol·L^{-1}, 1 mol·L^{-1} and 4 mol·L^{-1}) was realised by the addition of sodium chloride. Sodium chloride purchased from Aldrich with the highest purity available.

Synthesis of polyvinyl benzoic acid

In a three-necked flask equipped with reflux condenser 1 g (6.7 mmol) 4-vinylbenzoic acid, 10 mL dimethylformamide, 0.189 g (0.67 mmol, short-chain) or 1.89 mg (0.067 mmol, long-chain) of the initiator 4,4'-Azobis(4-cyano pentanoic acid) was mixed together under nitrogen atmosphere. Afterwards the mixture was heated to 65 °C and stirred for 24 hours. The reaction solution was transferred over a syringe filter into 200 mL of diethyl ether. In the next step, the diethyl ether was decanted. The polymer was washed with 200 mL of Diethyl ether, sucked off via Glass frit and dried over three days under high vacuum.

Clay samples

Kaolinite samples were received from Clay Mineral Society. As samples kaolinite Kaolin KGa-1b (low-defect) and Kaolin KGa-2 (high-defect) were used in this study. KGa-2 is a less crystallized, whereas KGa-1b is a well crystallized kaolinite.[2]

Synthesis of intercalation compounds

The synthesis of intercalation compounds of potassium acetate and kaolinite followed a slightly modified instruction of Frost et al.[3] To acetic acid potassium hydroxide was added and subsequently diluted with deionized water to give a 60 % (for some experiments also 30 %) potassium acetate solution. For the intercalation to 1 mL of this solution 0.3 g kaolinite was added and for 72 hours put on an orbital shaker (compact shaker KS 15, Edmund Bühler GmbH, Hechingen, Germany) with a shaking speed of 350 rpm. The resulting suspension was centrifuged (Centrifuge 5804, Eppendorf Vertrieb Deutschland GmbH, Wesseling-Berzdorf, Germany) for 30 minutes at 8000 rpm. The supernatant was decanted and the remaining solid material dried in a desiccator for at least 48 hours over Sicapent®.

For the intercalation of potassium hexanoate, hexanoic acid and potassium hydroxide were neutralized. Afterwards the solution was evaporated to dryness, which gives potassium hexa-

noate. For the intercalation a dimethyl sulfoxide (DMSO) kaolinite (KGa-1b) intercalation compound (rate of intercalation around 71 % from XRD measurements) was used as starting material. From this precursor 0.5 g were added to a solution of 13.5 g potassium hexanoate in 12.5 mL of water. The suspension was stirred for two hours at 50 °C and sucked off through a glass frit. The solid was washed three times with water. Afterwards it was vacuum dried overnight.

The synthesis of the DMSO-KGA-1b intercalation compound followed a synthesis publicized by Li et al., but without any precondition of the kaolinite.[4] In a 100 mL round bottom flask, 4 g KGa-1b, 64 mL DMSO and 15 mL Methanol were mixed. This suspension was heated to reflux at 85 °C for 96 hours. After cooling down to room temperature, the suspension was filtered through a glass frit. The solid material was washed three times with ethanol and dried overnight under vacuum.

Eu(III) LMWC complexes with Kaolin KGa-2

To a Eu(III) solution ($c_{Eu(III)} = 4 \cdot 10^{-4}$ mol·L^{-1}, background electrolyte 0.01 mol·L^{-1} $NaClO_4$)) a low molecular weight compounds (LMWC) (e. g., formic, acetic, propionic, or glycolic acid) with a concentrations between 0 mol·L^{-1} ≤ c_{LMWO} ≤ 10^{-1} mol·L^{-1} was added. Kaolin KGa-2 was added and the p*H* was adjusted to five. After stirring for one hour, the suspension was centrifuged for 30 minutes at 7000 rpm. Solid and supernatant were separated and the solid fraction was dried overnight at 35 °C. With the dried solids, time-resolved luminescence measurements were carried out.

2.2 Methods

Luminescence measurements of Lanthanide(III) complexes with model ligands

The luminescence decay times of Tb(III) complexes in the temperature range between 278 K < *T* < 353 K were recorded by using a Fluoromax 4 spectrofluorometer (*HoribaJobin-Yvon*) coupled to a single photon counting controller (*HORIBA Scientific*) in the multichannel scaling mode. Tb(III) was directly excited with λ_{ex} = 378 nm and the detected emission wavelength was λ_{em} = 542 nm. Luminescence decay time curves of Tb(III) complexes were also measured by indirect excitation of Tb(III) (Tb(III) salicylate: λ_{ex} = 325 nm, Tb(III) phthalate: λ_{ex} = 330 nm). In order to maintain the desired temperature, a thermostat system was used (*LAUDA, Proline RP 845 C*).

Time-resolved laser luminescence spectroscopy measurements of Sm(III), Dy(III) and Eu(III) complexes were performed using a pulsed Nd-YAG Laser (Spectra Physics) combined with an optical parametric oscillator (*GWU Lasertechnik*) for excitation. The luminescence was detected using an iCCD-camera coupled spectrograph (*Andor Technology*). For the Sm(III) and Dy(III) complexes the emission spectra were recorded in the spectral range of 457 nm ≤ λ_{em} ≤ 741 nm, the emission spectra of the Eu(III) complexes were recorded in the range of 575 nm < λ_{em} < 636 nm. For the measurements in the hole temperature range (77 K ≤ *T* ≤ 353 K) an excitation wavelength λ_{ex} = 477 nm was applied to excite the Sm(III) ion

directly ($^4I_{11/2}\leftarrow{}^6H_{5/2}$-transition). For Dy(III) complexes λ_{ex} = 450 nm ($^4I_{15/2}\leftarrow{}^6H_{15/2}$-transition) and for Eu(III) complexes λ_{ex} = 394 nm was chosen ($^5L_6\leftarrow{}^7F_0$-transition). One complete luminescence decay was measured by collecting 100 to 130 luminescence spectra at increasing δt using a step width between 6 μs < Δt < 10 μs for Sm(III) or Dy(III) and of Δt = 50 μs for Eu(III). For one luminescence spectra five laser pulses were accumulated. For the Eu(III) measurements in the time-gated detection scheme, the initial delay time after the laser flash (δt) was varied between 0.4 μs < δt < 30.4 μs (depending on the temperature) in order to discriminate luminescence originating from the luminescence of the $^5D_1\rightarrow{}^7F_0$ transition. In the case of Sm(III) and Dy(III) an initial delay time of δt = 152 μs was used. The time dependence of the Sm(III), Dy(III) and Eu(III) luminescence was analysed based on a box car technique. To adjust the temperature in the range 278 K < *T* < 353 K a thermostat was used (Lauda).

An Oxford Dewar was used for the luminescence decay time measurements of Sm(III), Dy(III) and Eu(III) as well as Tb(III) complexes in the lower temperature range (77 K ≤ *T* ≤ 275 K).

The time-resolved measurements of Tb(III) complexes in the lower temperature range (77 K ≤ *T* ≤ 275 K) were recorded as well with a pulsed Nd-YAG Laser (Spectra Physics) combined with an optical parametric oscillator (*GWU Lasertechnik*). The luminescence was detected with an iCCD-camera coupled spectrograph (*Andor Technology*). The excitation wavelength λ_{ex} = 378 nm (according to $^5G_5\leftarrow{}^7F_6$-transition) was used to excite the Tb(III) ion directly and the emission spectra were recorded in the spectral range of 400 nm ≤ λ_{em} ≤ 739 nm. By collecting 120 luminescence spectra (100 accumulations for one luminescence spectra) at increasing δt while using a step width of Δt = 500 μs a complete luminescence decay was measured. The initial delay time after the laser flash was δt = 1 μs. The time dependence of the Tb(III) luminescence was analyzed by using the boxcar technique.

For luminescence spectroscopy at ultra low temperatures, sample solutions were transferred to quartz tubes (40 mm length x 4 mm o. d. x 2 mm i.d.; volume ca. 100 μL), and sealed with rubber septums. Samples were cooled to ~ 5 K in a lab-built sample holder, mounted on a closed-cycle helium refrigerator (SRDK-205 cryostat; Janis Research Company). The samples were excited using a dye laser (LPD 3002; Lambda Physics, Göttingen, Germany) pumped by a Nd:YAG laser (QuantaRay, Spectra Physics). Coumarin 153 (Radiant Laser Dyes & Accessories GmbH) was used as laser dye. The laser was operated at 20 Hz with a pulse width of 10 ns. The Eu(III) emission was collected at a 90 ^{o} angle relative to the excitation light by two 10 cm F/4 quartz lenses and focused on the entrance slit of a triple monochromator (Spex 1877). For detection an intensified charged-coupled device (iCCD) camera (iStar DH720-25U-03; Andor Technologies) was used in the gated mode. In order to obtain adequate stray light suppression, delay and gate width of the iCCD were set to 1 μs and 10 ms, respectively. The achieved spectral resolution in the emission dimension was 0.1 nm (3 cm^{-1}) in a total spectral detection window of 37 nm. Each emission spectrum was accumulated for 1 s to 5 s, comprising 20 to 100 laser pulses. The excitation wavelength was varied with a scan rate ranging from

0.001 nm/s to 0.05 nm/s, yielding a resolution in the excitation dimension between 0.03 cm^{-1} and 1.5 cm^{-1}. The decay curves were extracted from time series of emission spectra (delay 1 µs, gate width 10 ms) of 200 spectra. For each sample several decay series were recorded, at each excitation wavelength λ_{exc} corresponding to a separate species in the TLS.

Data analysis

Luminescence decays: In case the luminescence decay curves were monoexponential, they were evaluated according to eq. (1)

$$y = y_0 + B \cdot exp\left(-\frac{t}{\tau}\right) \quad (1)$$

y is the measured luminescence intensity at time *t* after the laser flash, *B* is the luminescence intensity at $t = 0$, τ is the luminescence decay time, and y_0 accounts for residual background signal.

From the in-depth analysis of the Eu(III) luminescence, especially when recorded at cryogenic conditions, a wealth of information can be obtained:

$^5D_0 \rightarrow {}^7F_0$ transition energy: The $^5D_0 \leftarrow {}^7F_0$ transition is extremely weak because of parity forbiddance. It gains intensity in cases in which the symmetry of the Eu(III) complex is lowered, for instance due to the formation of non-centrosymmetric complexes or due to vibrational motion of the ligands. For being non-degenerate the $^5D_0 \leftarrow {}^7F_0$ transition is a powerful indicator for the presence of different coexisting complexes in a sample. Moreover, its energy is very sensitive to specific parameters characterizing the complex. Two partly contradicting effects determine the energy of the $^5D_0 \leftarrow {}^7F_0$ transition: i) the nephelauxetic effect and ii) the splitting of the $^7F_1$ transition, which is dependent on the crystal field exerted by the ligands.

Point symmetry group and asymmetry ratio r: Under site-selective excitation conditions the number of STARK levels in the $^5D_0 \rightarrow {}^7F_1$ and $^5D_0 \rightarrow {}^7F_2$ transitions can be used to determine the point symmetry group of the coordination polyhedron.

The integrated intensity of the $^5D_0 \rightarrow {}^7F_2$ transition is especially sensitive to the complex symmetry. The more the local complex symmetry deviates from inversion symmetry the more the parity forbiddance is relaxed. In contrast, the integrated $^5D_0 \rightarrow {}^7F_1$ emission is not affected and can therefore be used as an internal reference. A change of the "asymmetry ratio *r"* (Equation 2) indicates an alteration of the complex symmetry. In general, an increasing deformation of the coordination polyhedron following the exchange of water molecules by other ligands results in a larger *r* value according to:

$$r = \frac{I(\,^5D_0 \rightarrow {}^7F_2)}{I(\,^5D_0 \rightarrow {}^7F_1)} \quad (2)$$

The asymmetry ratio *r* depends on several other parameters, such as i) the polarizability of the ligands, ii) the complex-related concentration of the ligands, and iii) the dielectric constant

of the solvent. Nonetheless, for samples containing the same or very similar ligands, investigated under identical experimental conditions, *r* may be used as a discriminator for different species present in the sample.

Number of water molecules in the first coordination sphere: A major radiationless deactivation pathway of Eu(III) is related to the OH groups present in the first, but also (to a minor extent) in the second coordination sphere of the complex. It has been established that the number of water molecules n_{H2O} in the first coordination sphere of Eu(III) can be determined from luminescence decay time measurements τ_{obs}. The well-known empirical equations of HORROCKS et al. and KIMURA et al. have been extended to account for additional quenching contributions from other ligands and from OH groups in the second coordination sphere with the terms 0.25 and 0.4 n_{OH}, respectively.

$$n_{H_2O} = 1.2\left(\frac{1ms}{\tau_{obs}} - 0.58 - 0.25 - n_{OH} \cdot 0.4\right) \quad (3)$$

This formula was derived at room temperature conditions. Since no influence of temperature on the fluorescence decay time was observed ($\tau_{Eu(H_2O)_{8-9}^{3+}}$ = 100 µs ± 10 µs at 298.15 K and 106 µs ± 10 µs at 4.7 K) it is concluded that the quenching efficiency of OH vibrations is not altered with temperature and thus eq. (3) can also be used at 4.7 K.

The equation takes only the effect of X-H vibrations as possible acceptors for a radiationless energy transfer into account. The presence of (organic) ligands can add additional options for a radiationless deactivation. Especially the triplet state and the redox properties of the ligand may have to be taken into account. In general, the experimental observed luminescence decay time is determined by the rate constants of the different deactivation processes. Here, the fastest process rules the observed decay kinetics. The nature of this process is strongly depending on the particular ligand. The general expression for the luminescence decay time of a Ln(III) complex is:

$$\tau_{Ln(III)\ complexes} = \frac{1}{k_r + k_{pet} + k_{ebt} + (n-x)\cdot k_{OH} + \sum_j k_j^{'nr}} \quad (4)$$

Here, the rate constants k_x are related to the respective processes (r = radiative, pet = photo-induced (charge) electron transfer, ebt = energy back transfer, OH = OH quenching, nr = other non-radiative deactivation processes).

The contribution of the different ligand-related processes can extracted from luminescence decay time data of the respective Ln(III) complex and the Ln(III) aquo complex ($[Ln(H_2O)_n]^{3+}$):

$$\frac{1}{\tau_{Ln(III)\ complexes}} - \frac{1}{\tau_{[Ln(H_2O)_n]^{3+}}} = k_{pet} + k_{ebt} - x \cdot k_{OH} \quad (5)$$

In aqueous solution only Sm(III), Dy (III), Tb(III) and Eu(III) show luminescence. Some photophysical parameters of these ions are listed in Table 2.

Table 2: Luminescence deacy times τ of the Ln(III) ions in water (taken from [5]) and life time of the radiative deactivation τ_{rad} (taken from [6]) and the emitting state of selected Ln(III) ions.

Lanthanide(III) ion	τ / µs	τ_{rad} / µs	emitting state
Dy^{3+}	2.5	1850	$^4F_{9/2}$
Tb^{3+}	430	9020	$^5D_4$
Sm^{3+}	2.7	6260	$^4G_{5/2}$
Eu^{3+}	110	9670	$^5D_0$

Temperature dependence of τ - Arrhenius data evaluation

The luminescence decay times τ of the Ln(III) complexes were measured in the temperature range of 77 K < T < 353 K. The experimental rate constants $k = 1/\tau$ were evaluated by the Arrhenius equation to determine the activation energy E_a of the overall rate determining process:

$$\ln k = \ln A - \frac{E_a}{R \cdot T} \qquad (6)$$

In case of Ln(III) in complexes with organic ligands k was determined according to eq. (6) in order to analyse the temperature dependence of the ligand-related deactivation processes.

Energy transfer

The occurrence of the non-radiative transfer of energy is a well-known photophysical phenomenon. Depended on the mechanism it is differentiated between an exchange of electrons and a resonant energy transfer. The exchange (or Coulomb) interaction requires an overlap of the involved orbitals and happens on short distances, whereas the resonant mechanism is based on a dipole-dipole interaction between an electronically excited donor and acceptor in its ground state. The efficiency of the energy transfer η depends on the distance R between donor and acceptor

$$\eta = \frac{R_0^6}{R^6 + R_0^6}. \qquad (7)$$

The distance R_0 is called the Förster distance, where the efficiency of the energy transfer is 0.50. The R_0 value is determined by the luminescence quantum efficiency of the donor, the overlap integral of donor's emission spectrum and acceptor's absorption spectrum as well as the refractive index of the surrounding medium, and by the orientation factor κ^2. Horrocks and coworkers calculated Förster distances for different donor/acceptor pairs.[7] They found a Förster distance of 8.53 Å (9.12 Å) for the pair Eu(III)/Nd(III) (Tb(III)/Nd(III)) in solution. The

energy transfer efficiency can be calculated from luminescence decay time τ or luminescence intensity *I*.

$$\eta = 1 - \frac{I_{\mathrm{DA}}}{I_{\mathrm{D}}} = 1 - \frac{\tau_{\mathrm{DA}}}{\tau_{\mathrm{D}}} \tag{8}$$

Here, the index "DA" means donor's luminescence intensity *I* or luminescence decay time τ in presence of an acceptor and "D" reflects *I* or τ in absence of an acceptor. By knowing the Förster distance R_0 distances of suitable Ln(III) ions can be deduced from stationary or time-resolved luminescence measurements.

Complexation of Lanthanide(III) ions by humic substances

The complexation of Ln(III) ions by HS can be described by a simple 1:1 complex formation

$$\mathrm{Ln}^{3+} + \mathrm{HS}^{y-} \leftrightharpoons [\mathrm{LnHS}]^{3-y}.$$

For a reaction like this, a mass action law can be formulated

$$\beta = \frac{c([\mathrm{LnHS}]^{3-y})}{c(\mathrm{Ln}^{3+}) \cdot c(\mathrm{HS}^{y-})}. \tag{9}$$

In the equation above $c([\mathrm{LnHS}^{3-y}])$, $c(\mathrm{Ln}^{3+})$ and $c(\mathrm{HS}^{y-})$ are the concentrations of the complex formed, the concentration of the Ln(III) ions in solution and the concentration of free binding sites in the HS, respectively. Due to the formation of a complex between Ln(III) ions and HS, the intrinsic fluorescence of HS is quenched. The quenching of the intrinsic fluorescence can be used to derive conditional complexation constants β from titration experiments following an approach of Ryan and Weber.[8,9] In these experiments the concentration of the Ln(III) ion is subsequently increased and the fluorescence intensity is measured. The intrinsic fluorescence intensities at a certain Ln(III) concentration is given relative to the intrinsic HS fluorescence, when no Ln(III) ions are present. From these I_{rel} the conditional complexation constants β can be derived using applying following equation.

$$I_{\mathrm{rel}} = 1 + \frac{I_{\mathrm{ML,rel}} - 1}{2\beta c_{\mathrm{L}}} \left(\beta c_{\mathrm{L}} + \beta c_{\mathrm{M}} + 1 - \sqrt{(\beta c_{\mathrm{L}} + \beta c_{\mathrm{M}} + 1)^2 \; - 4\beta^2 \, c_{\mathrm{L}} c_{\mathrm{M}}} \right) \tag{10}$$

In this equation $I_{\mathrm{ML,rel}}$ is the relative remaining intrinsic HS fluorescence at high Ln(III) ion concentrations, c_{M} is the total Ln(III) ion concentration and c_{L} the total number of binding sites, which is given by the third of the number of charges[d] in the HS at a given p*H* value. The charge density was calculated from a modified Henderson-Hasselbalch equation.[10]

$$\boldsymbol{Q}_{\mathrm{tot}} = \frac{\boldsymbol{Q_1}}{\mathbf{1} + (\boldsymbol{K_1}[\boldsymbol{H}^+])^{1/\boldsymbol{n_1}}} + \frac{\boldsymbol{Q_2}}{\mathbf{1} + (\boldsymbol{K_2}[\boldsymbol{H}^+])^{1/\boldsymbol{n_2}}} \tag{11}$$

[d] Due to coordination of one Ln(III) ion, its three positive charges have to be compensated.

The parameters K_1, K_2, n_1, n_2, Q_1 and Q_2 are available from the International Humic Substance Society (IHSS) and are listed in Table 3.

Table 3: p*H* titration and elemental composition parameters of some HS under investigation given by the IHSS [10]. Abbreviations: SR – Suwannee River, PP – Pahokee Peat, HA – humic acid, FA – fulvic acid.

	C content / %	Q_1 / meq/g·C	lg(K_1)	n_1	Q_2 / meq/g·C	lg(K_2)	n_2
SRHA	52.63	9.74	4.35	3.3	4.48	10.44	1.73
PPHA	56.37	9.64	4.22	3.2	0.94	9.86	1
SRFA	52.44	11.66	3.76	3.24	2.05	9.84	1.45
PPFA	50.45	14.22	3.99	3.33	0.76	9.57	1

Refractive index

The refractive index was measured using a multi-wavelength refractometer (DSR-λ, Schmidt+Haensch) in the wavelength range of 400 nm < λ < 1000 nm. The measurements were carried out at 20 °C as well as 35 °C and data points were taken at seven wavelength (403,3 nm; 495,9 nm; 598,7 nm; 669,9 nm; 742,3 nm; 842,8 nm; 945 nm). The experimental data were interpolated with the help of a Cauchy equation and evaluated by a self-written program in LabView[e].

Vibrational spectroscopy measurements

Theoretical background

Due to the interaction of an electromagnetic wave with matter, the electric field ***E*** can induce a dipole momentum μ in the matter.[11]

$$\boldsymbol{\mu} = \boldsymbol{\mu_0} + \boldsymbol{\alpha E} + \boldsymbol{\beta_{SFG} E^2} + \boldsymbol{\gamma E^3} + \cdots \qquad (12)$$

The strength of the induced dipole moment depends on the polarizability α, and the first and second order hyperpolarizabilities β_{SFG} and γ, respectively. A static dipole momentum is reflected by $\boldsymbol{\mu}_0$. In a bulk phase, the single induced dipole momenta give a macroscopic property, the polarization ***P***, which can be expressed by

$$\boldsymbol{P} = \boldsymbol{\varepsilon_0}\left(\boldsymbol{\chi^{(1)} E} + \boldsymbol{\chi^{(2)} E^2} + \boldsymbol{\chi^{(3)} E^3} + \cdots\right). \qquad (13)$$

$$\boldsymbol{P} = \boldsymbol{P^{(1)}} + \boldsymbol{P^{(2)}} + \boldsymbol{P^{(3)}} + \cdots$$

Here, ε_0 is the vacuum permittivity, $\chi^{(1)}$ are the first order (linear) susceptibility as well as $\chi^{(2)}$ and $\chi^{(3)}$ the non-linear second and third order susceptibilities, respectively. Non-linear effects can only be observed, when strong electric fields are applied. For a sum-frequency generation (SFG) experiment, two electric fields resulting from visible and IR laser radiation have to overlap in space and time on the desired sample. The electric field felt by the matter is

[e] The programm in LabView was written by Marvin Münzberg

$$\boldsymbol{E} = \boldsymbol{E}_{\mathrm{IR}} \cos(\omega_{\mathrm{IR}} t) + \boldsymbol{E}_{\mathrm{vis}} \cos(\omega_{\mathrm{vis}} t) \tag{14}$$

with $\boldsymbol{E}_{\mathrm{IR}}$ and $\boldsymbol{E}_{\mathrm{vis}}$ being the electric field of the IR light with a frequency ω_{IR} and the electric field of the vis light ω_{vis}, respectively. For SFG only the second term in eq. (13) has to be considered. By inserting the expression for $\boldsymbol{E}$ given in eq. (14) into $\boldsymbol{P}^{(2)}$ and solving the quadratic dependence of $\boldsymbol{E}$, gives four different electric fields. One of them is a static one, a second gives the doubled frequency, a third the difference frequency and the fourth the sum of both incident electric fields. For SFG, the fourth term is of importance.

The second order susceptibility $\chi^{(2)}$ is the macromolecular average of the molecular hyperpolarizability β_{SFG}, which is given by[11]

$$\chi^{(2)} \propto \beta_{\mathrm{SFG}} \propto \frac{A_{\mathrm{K}} M_{\mathrm{IJ}}}{\omega_{\nu} - \omega_{\mathrm{IR}} - \mathrm{i}\Gamma}. \tag{15}$$

In the above equation, A_{K} is the IR and M_{IJ} the Raman transition momentum, respectively. The molecular vibration frequency is denoted with ω_{ν} and the IR frequency with ω_{IR}. The value Γ^{-1} is the relaxation time of the involved vibrational excited state. As closer ω_{IR} is to ω_{ν} the higher is the value of β_{SFG} and hence the SFG signal intensity I_{SFG} for a single transition

$$I_{\mathrm{SFG}} \propto I_{\mathrm{IR}} I_{\mathrm{vis}} \left| \chi^{(2)} \right|^2 \tag{16}$$

as it is proportional to the square of $\chi^{(2)}$ and direct to the intensities of the laser beams in the visible I_{vis} and infrared I_{IR} region of the spectrum.[12] For media with a center of inversion $\chi^{(2)}$ will vanish.[13] A disordered (bulk) phase has inversion symmetry and gives thereby no SFG signal. Only at surfaces and interfaces the symmetry is broken and SFG signals will appear. For that reason SFG spectroscopy is extremely interface sensitive. Another prerequisite arises from eq. (15). Only vibrational transitions, which are Raman and IR allowed, will give rise to a SFG signal.

Raman spectroscopy

Raman spectra were recorded using a confocal Raman microscope (alpha 300RA, WITec GmbH, Ulm, Germany). The excitation was achieved by fiber-coupled single mode laser operating at 532 nm. The excitation light was focused on the sample by a 100x objective. The scattered light was collected through the same objective, guided through an optical fiber to the spectrograph and was measured with a CCD camera. The integration time was adjusted dependent on the signal level and lies typically between 0.5 s and 180 s. To increase the signal-to-noise ratio, the final spectrum results from the accumulation of 3 to 15 single spectra. The

received spectra were processed (baseline correction, cosmic ray removal) with an instrument specific software, WITec Control.

SFG spectrometer

The SFG measurements were carried out on a commercial available SFG spectrometer (EKSPLA, Vilnius, Lithuania). The setup is based on the 1064 nm output of a Nd:YAG laser with a pulse duration ≤ 30 ps and a repetition rate of 10 Hz, which is directed into a harmonic unit. Here, part of the incident light is frequency doubled (second harmonic, 532 nm) and partly coupled out. The other part of the second harmonic and the remaining fundamental is guided into an optic-parametric oscillator and an optic-parametric amplifier, which convert the fundamental and second harmonic by non-linear processes to tunable infrared light (2.3 µm ≤ λ ≤ 10.0 µm).

In a typical experiment, the vibration of the OH region of the kaolinite was scanned from 3550 cm^{-1} to 3750 cm^{-1} with an increment of 1 cm^{-1}. To increase the signal-to-noise ratio of the SFG signal at each step, the signal was accumulated ten times.

XRD measurements

X-ray diffraction measurements (XRD) of the kaolinite samples were carried out at an X-Ray Powder Diffractometer D5005 with a Copper anode (Siemens/Bruker) by Dr. C. Günther, Institute of Earth- and Environmental Sciences at the University of Potsdam.

3. Results and discussion

3.1 Influence of temperature and ionic strength on the luminescence of Lanthanide(III) complexes

Due to the outstanding selectivity and sensitivity, luminescence techniques are powerful analytical tools in speciation analysis of Actinides (or Lanthanides as natural analogous). Based on spectroscopic data, especially kinetic data, complexation constants and stoichiometric information are determined. However, in the data evaluation care has to be taken that the fundamental photophysics underlying the observed luminescence signals is fully understood before conclusions on the complexes are drawn. Especially the interplay between the electronic systems of the Ln(III) and the ligands is important. Although the f-electrons of the Lanthanides do not (or only to a very small extend) contribute to the binding of ligands, the luminescence of the Lanthanides, which originated from transitions within the f-electron multiplet, can be distinctly influenced. In water the Ln(III) form aquo complexes (depending on the p*H* of the solutions other complexes may also be formed). Upon complexation of an organic (or inorganic) ligand, water is released from the first coordination sphere. Depending on the ligand and its complexation properties, one or two water molecules may be release. Because of the effective luminescence quenching by water molecules in the first (but also to a lesser extent by water molecules in higher) coordination spheres, it is expected that the Ln(III) luminescence quenching is decreased upon binding of an organic ligand resulting in higher luminescence efficiency and increased luminescence decay times. In addition to the reduced luminescence quenching the exchange of water molecules with organic ligand(s) is also altering the symmetry of the complexes which subsequently affects the spectral intensity distribution observed for Eu(III). Here, alteration of the ligand field is reflected in the intensity and spectral positions of the Stark levels. For a qualitative and especially for a quantitative evaluation of spectroscopic parameters in speciation analysis the electronic interplay between Ln(III) ion and ligand(s) needs to be taken into account.

Low molecular organic compounds such as glycolic acid and salicylic acid (see Figure 1S) were used as model compounds for i) low molecular organics found (released) in (from) clays and ii) building block of natural organic matter (e.g., HS). In the experiment the electronic (and redox) properties were varied by the change of the ligands as well as of the Ln(III) ion. The organic ligands investigated varied in their triplet energies and in their overall photochemistry. The Ln(III) ions were selected for the differences in the energy gap between the highest energy level of the electronic ground state and the lowest energy level of the first excited state (see Table 4).

Table 4: Energy values of the first excited electronic level and energy gap values for Ln(III) ions.[14–17]

	Sm(III)	Eu(III)	Tb(III)	Dy(III)
Energy of first excited electronic level / cm^{-1}	17924	17200	20500	21200
energy gap ΔE / cm^{-1}	7400	12300	14800	7850

Based on reported binding constants the speciation distributions for the different ligand-Ln(III) combinations were calculated. Based on the calculation the sample composition was adjusted. In order to minimize the complexity of the samples, compositions in which mainly the Ln(III) aquo complex and the 1:1 complex with the ligand was present were chosen. Ionic strength (0 mol·L^{-1} < I < 4 mol·L^{-1})[c] and temperatures (77 K < T < 353 K) were varied and the effect on the luminescence decay kinetic was monitored for Ln(III) = Eu(III), Tb(III), Sm(III) and Dy(III).

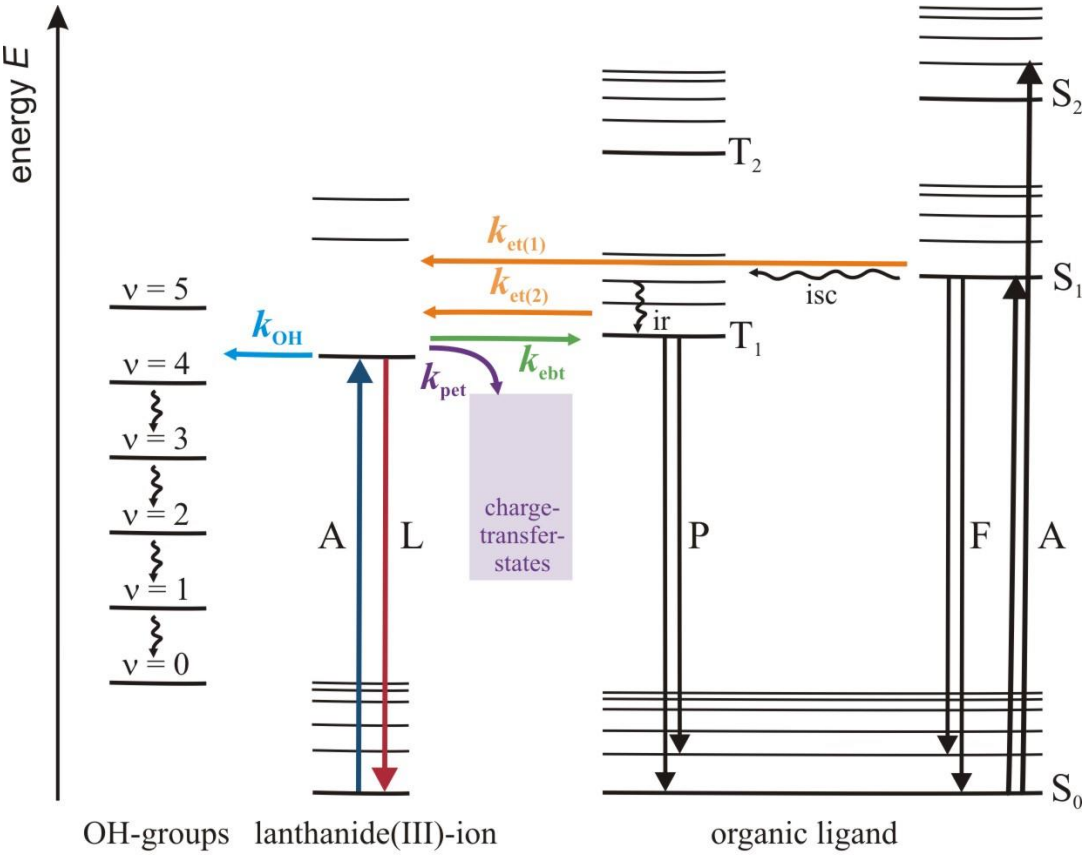

Figure 1: Summary of the possible intra-complex deactivation (quenching) processes for Ln(III) ions. Shown is the complex interplay between relative energy difference and quenching process determining the overall luminescence of the Ln(III) complex. Considered are the energy difference between i) Ln(III)-related energy levels, ii) ligand and Ln(III) levels, including water, and iii) the redox properties of the partners (A – absorption, L – luminescence, P – phosphorescence, F – fluorescence, S – singulet state, T – triplet state, ir – inner relaxation, isc – intersystem crossing, *k* – rate constant of: OH – quenching by OH-vibrations, ebt – energy back transfer and pet – photo induced electron transfer).

In Figure 1 an overview of the different intra-complex radiationless deactivation processes to be considered for Ln(III) complexes with organic ligands is shown. Three major additional pathways for radiationless deactivation need to be taken into account: i) deactivation by OH-vibrations (but also to other functional groups such as NH with suitable vibrational energies may be considered), ii) energy (back) transfer to the ligand (e.g., to ligand triplet state), and iii) photoinduced redox reaction between Ln(III) and ligand (e.g., photoinduced electron or

charge transfer between ligand and Ln(III)). Case i) and ii) are both radiationless energy transfer processes. The contribution of the different intra-Ln(III) and complex-related radiationless deactivation processes is determined by the corresponding rate constants and here the fastest process(es) will dictate the observed overall deactivation. Hence, the specific combination of Ln(III) and ligand each having specific intrinsic electronic properties has to be considered in the interpretation of the spectroscopic data during speciation analysis. In order to evaluate the different radiationless deactivation pathways and to show the consequences on the data interpretation, Ln(III) and ligands were combined to foreground specific deactivation processes.

Direct excitation conditions

Case i) deactivation via OH-vibrations in aqueous solution

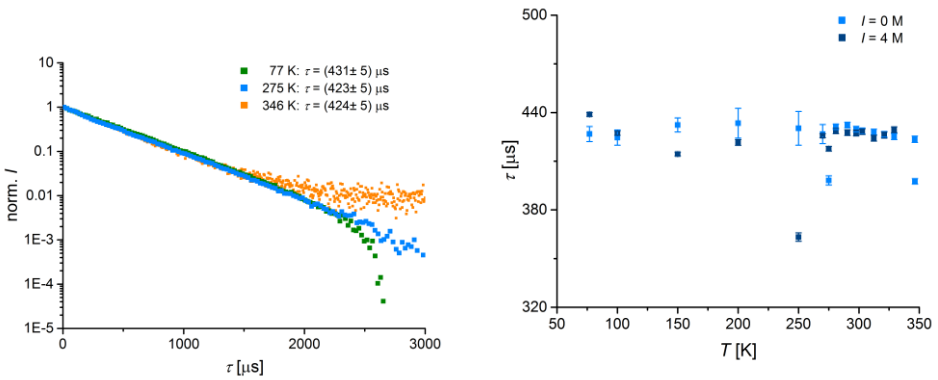

Figure 2: (left) Luminescence decay kinetics of $[Tb(H_2O)_8]^{3+}$ at different temperatures (λ_{ex} = 378 nm, λ_{em} = 542 nm). (right) Luminescence decay time of $[Tb(H_2O)_8]^{3+}$ at different temperature for low and high ionic strength conditions.

The influence of temperature and ionic strength on the luminescence decay time was investigate for Ln(III) = Eu(III), Tb(III), Dy(III), and Sm(III) aquo complexes. In Figure 2 the influence of temperature and of ionic strength on the luminescence decay kinetics (and decay time) of the Tb(III) aquo complex is shown. The luminescence decay time was determined for a temperature interval of around ΔT = 300 K and no systematic influence was found. The experiments was also carried out with samples at different ionic strength (0 mol·L^{-1} < I < 4 mol·L^{-1})[c]. From the results (see Figure 2 (right)) no temperature influence could be deduced. Moreover, the comparison between the luminescence decay times at the different ionic strength shows that it has also no influence on τ. Same results were obtained for the other Ln(III) ions investigated. From the luminescence measurements of the Ln(III) aquo complexes it can be concluded that the luminescence quenching efficiency of the water molecules in the first (and second) coordination sphere of the Ln(III) ions is not altered by the ionic strength. So additional Coulomb effects due to high concentration of ions in the water phase (e.g., change in the vibrational frequencies due to water cluster formation etc.) are not reflected in an altered luminescence behavior of the Ln(III) ions here. For the different Ln(III) the experimentally determined luminescence decay times of the corresponding aquo complexes are summarized in Table 5.

Table 5: Luminescence decay times of the different Ln(III) aquo complexes. Shown are the average values calculated based on the results obtained for measurements in the temperature range of 77 K < *T* < 353 K and for ionic strengths of 0 mol·L^{-1} c < *I* < 4 mol·L^{-1}.

Ln(III) aquo complex	Luminescence decay time τ / µs
Tb(III)	425 ± 5
Eu(III)	110 ± 3
Sm(III)	2.9 ± 0.3
Dy(III)	2.9 ± 0.3

The comparison of the luminescence decay times determined for the different Ln(III) aquo complexes showed that the fastest luminescence decay kinetics are observed for Sm(III) and Dy(III). Both Ln(III) are characterized by a small energy difference ΔE between the lowest energy level of the first excited state and the highest energy level of the ground state (see also Figure 8). For both Ln(III) ΔE is in the range around 7500 cm^{-1}. On the other hand Tb(III) is characterized by a $\Delta E \sim 14800$ cm^{-1} and Eu(III) by a $\Delta E \sim 12300$ cm^{-1}. As a consequence the related rate constants for the radiationless energy transfer to the OH-vibrations of water is very high in case of Sm(III) and Dy(III) compared to Tb(III) or Eu(III). Using Fermi`s golden rule for the estimation of the rate constants the Franck Condon factor and the density of states in the accepting electronic system are of relevance. For the system of Ln(III) (donor) and H_2O (acceptor) the decreasing Franck Condon factor may be considered as the major factor ruling the rate constant.

Case ii) deactivation via energy (back) transfer (ebt) to ligand

In the next step the luminescence kinetics of Ln(III) in complexes with different organic ligands were investigated. A spectrum of different low molecular weight carboxylic acid was applied in the experiments. Here, the electronic properties of the ligands were varied with respect to the presence of additional hydroxylic (or comparable functional groups like NH and SH) and of aromatic structure. Especially the latter parameter defines the relative position of the ligand-related triplet states, which may serve as a "sink" in case of an energy back transfer (ebt) for the Ln(III) to the ligand. In order to become effective the rate constant for the ebt has to compete with the other deactivation processes such as quenching by OH-vibrations (vide supra). In the experiments low molecular weight organic ligands with different triplet energies were selected to probe the contribution of this deactivation process.

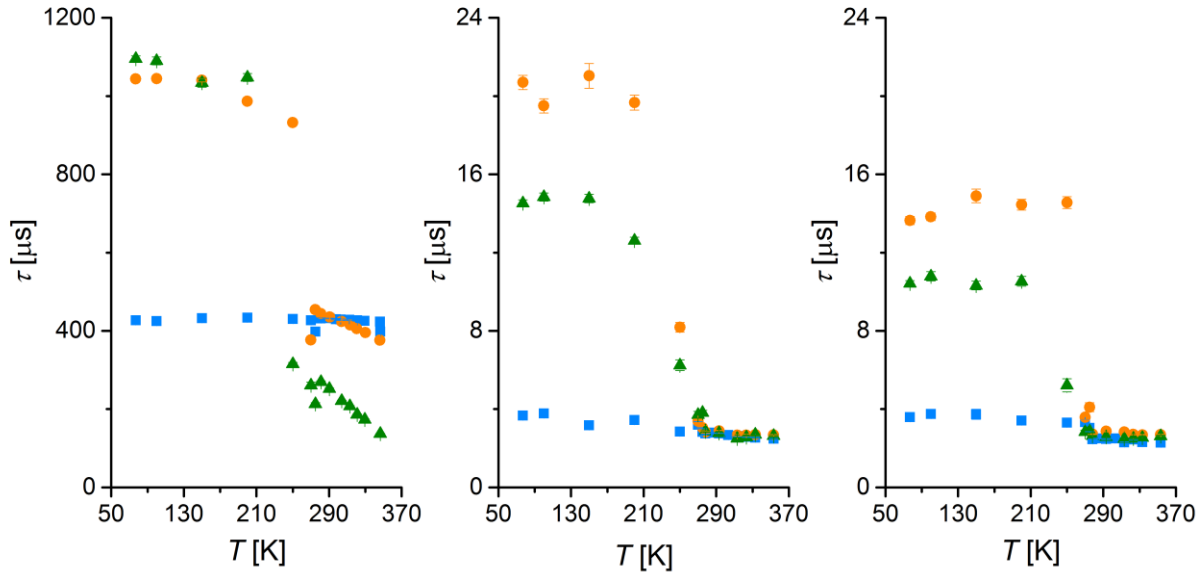

Figure 3: Luminescence decay times of Tb(III) (left, λ_{ex} = 378 nm , λ_{em} = 542 nm), Sm(III) (middle, λ_{ex} = 477 nm, λ_{em} = 592 nm), and Dy(III) (right, λ_{ex} = 450 nm, λ_{em} = 570 nm) in the temperature range 77 K < *T* < 353 K (orange circles: phthalate (p*H* = 4.2); green triangles: salicylate (p*H* = 5.0); blue squares: H_2O).

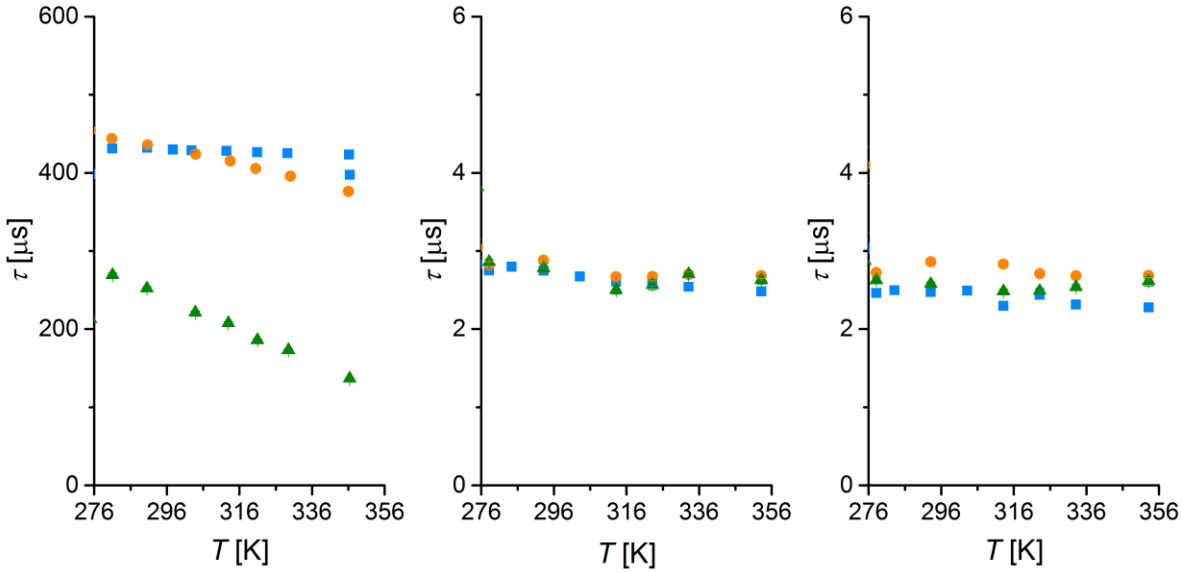

Figure 3a: Luminescence decay times of Tb(III) (left, λ_{ex} = 378 nm , λ_{em} = 542 nm), Sm(III) (middle, λ_{ex} = 477 nm, λ_{em} = 592 nm), and Dy(III) (right, λ_{ex} = 450 nm, λ_{em} = 570 nm) in the liquid phase (orange circles: phthalate (p*H* = 4.2); green triangles: salicylate (p*H* = 5.0); blue squares: H_2O) at temperatures between 276 K < *T* < 353 K.

In Figure 3 the luminescence decay times of the Ln(III) = Tb(III), Sm(III), and Dy(III) in complexes with salicylate and phthalate are shown determined in the temperature range of 77 K < *T* < 353 K. Depicted are also the τvalues found for the respective Ln(III) aquo complexes. In contrast to the Ln(III) aquo complexes the phthalate and salicylate ligands have a distinct

influence on the overall temperature dependence of τ and moreover, depending on the combination of Ln(III) and ligand the differential change with temperature is different. The most pronounced change was observed for salicylate in combination with Tb(III).

For Sm(III) and Dy(III) two clearly separated region can be identified in Figure 3. For temperatures below the freezing temperature of the solutions (around T = 270 K) the luminescence decay times were i) longer compared to the Ln(III) aquo complex and ii) for complexes with phthalate compared to salicylate longer τ were determined (Figure 3 (middle and right)). In the solid phase the luminescence decay times of the complexes were increased because water molecules are removed from the first coordination sphere and substituted by the coordinating group (e.g., carboxylic group) of the ligands. It can be assumed that one carboxylic group will replace two water molecules. Therefore, phthalate is potentially more effective because four water molecules are removed from the Ln(III) coordination, in case of salicylate only two water molecules (three if the hydroxylic group also contributes). This is reflected in the overall larger τ found for the Ln(III) complexes with phthalate (see Figure 3). For the liquid phase samples of Sm(III) and Dy(III) no differences to the corresponding Ln(III) aquo complexes were found (see Figure 3a). Here, the kinetic lability of Ln(III) complexes may determine the overall quenching. Due to a fast ligand exchange in combination with a very efficient OH-quenching (large Franck Condon factors, vide supra) the observable luminescence decay time is significantly reduced. Since Sm(III) as well as Dy(III) have an energy gap of 7000 $cm^{-1} < \Delta E <$ 8000 cm^{-1}, the energy difference to the ligand-related triplet state is large (several thousand cm^{-1}, see Figure 8 and Table 6) and subsequently a (thermally activated) energy transfer from the electronically excited Ln(III) (= Sm(III), Dy(III)) to the ligand triplet state is not operative.

Table 6: triplet energies E_T of the ligands.[18,19]

	E_T /cm^{-1}
salicylic acid	23800
phthalic acid	27400

Complexes of phthalate and salicylate with Tb(III) show divergent trends. For the solid phase i) only a weak temperature dependence at T < 270 K and ii) only minor differences between both ligands are found for the luminescence decay times. The quenching by water molecules is due to its unfavorable Franck Condon factor (vide supra) less efficient (compared to Dy(III) or Sm(III)). For the higher temperatures the differences between salicylic and phthalic acid again become evident (see Figure 3a). Since the triplet energy of the salicylic acid is smaller compared to phthalic acid, also the energy difference between Tb(III) excited states and triplet states in salicylic acid is smaller. This leads to a more efficient energy transfer and subsequently to a higher quenching influence. Because of the unfavorable coupling to OH-vibrations, the energy transfer to ligand triplet states comes into play for Tb(III) complexes.

For the temperature range of 278 K < *T* < 353 K the influence of the ionic strength (0 mol·L^{-1} < *I* < 4 mol·L^{-1})^{c} on the observed luminescence decay kinetics was investigated. In Figure 4 the luminescence decay times of Tb(III) and Dy(III) salicylate complexes are shown.

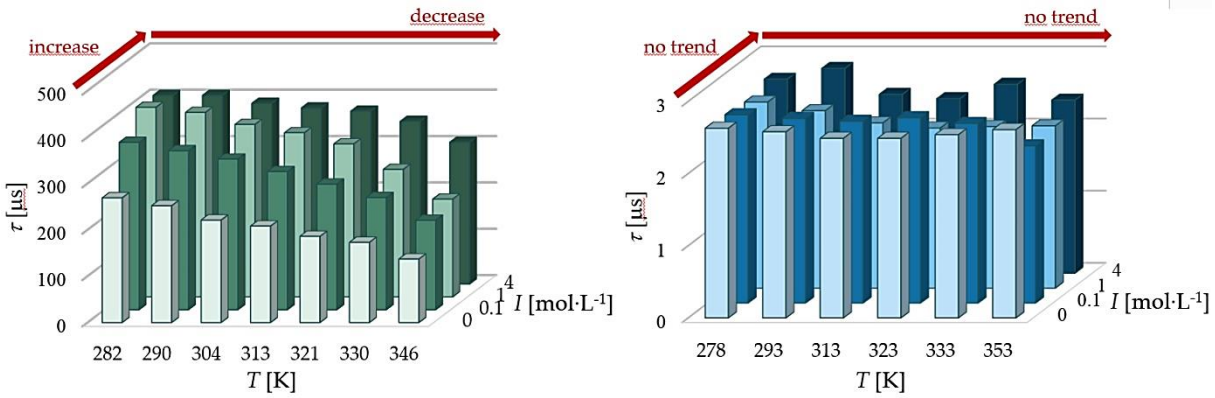

Figure 4: Luminescence decay times of salicylate complexes with Tb(III) (left) and Dy(III) (right) for the temperature range of 278 K < *T* < 353 K at different ionic strength (0 mol·L^{-1} < *I* < 4 mol·L^{-1})^{c}.

While for Dy(III) no further influence of the ionic strength was found, for the Tb(III) salicylate an increase in the luminescence decay time with increasing ionic strength was found. This increase could be caused by a shift of the Tb(III) complex equilibrium to a higher amount of Tb(III) aquo complexes, for what interactions between sodium ions and salicylate ligands are responsible and as a result less salicylate was coordinated by Tb(III). Because of the missing influence of salicylate on the luminescence decay time of Dy(III) in comparison to the Dy(III) aquo complexes this shift could not be observed.

An Arrhenius analysis of the luminescence decay times further underlines the differences in contributions of the radiationless energy transfer processes for Ln(III) aquo complexes and for Ln(III) complexed by organic ligands, respectively. While for Ln(III) aquo complexes the general high efficiency of the OH-quenching is reflected by a very low activation barrier, for Ln(III) complexed by organic ligands the contribution of an energy back transfer to the ligand may have to be considered (see Figure 5 (left)). In case of Tb(III) this deactivation process can compete with the OH related quenching. In this case the quenching is characterized by a different activation barrier. For Dy(III) and Sm(III) still the OH-related quenching is the major deactivation pathway and subsequently the determined activation energy is low (see Figure 5 (right)).

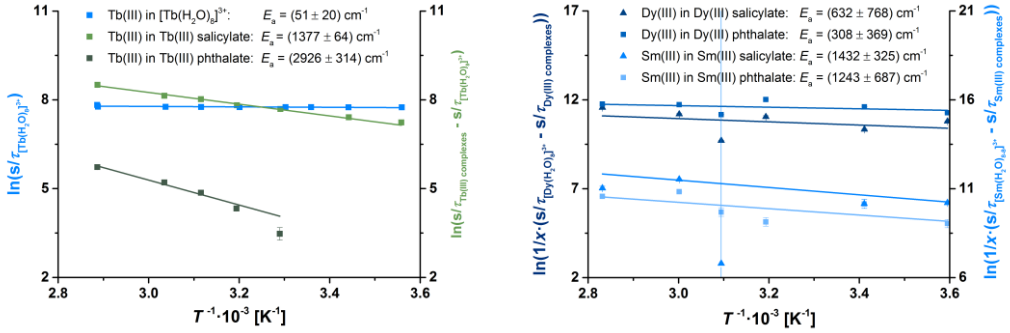

Figure 5: Arrhenius data evaluation for Tb(III) (left) as well as Sm(III) and Dy(III) (right) in aquo complexes as well as in complexes with organic ligands

Indirect excitation conditions

The experiments were performed under direct excitation of the Tb(III). In order to support the conclusions drawn with respect to the thermally activated energy back transfer via the ligands tiplet state (vide supra), additional experiments under indirect excitation conditions were carried out.

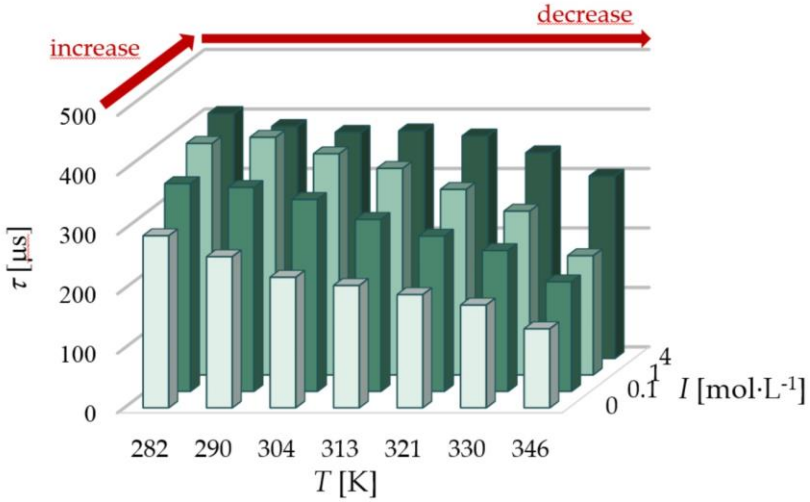

Figure 6: Dependence of the luminescence decay time of Tb(III) in complexes with salicylic acid in the temperture range 278 K < *T* < 353 K for different ionic strength *I*. The decay times were determined from luminescence kinetics measured under sensitized excitation conditions (λ_{ex} = 325 nm) (For comparison with direct excitation of Tb(III) at λ_{ex} = 378 nm see also Figure 4).

In Figure 6 luminescence decay times for Tb(III) in complexes with salicylic acid determined for indirect excitation (λ_{ex} = 325 nm) are summarized. Like in the case of direct excitation (see Figure 4) τ decreased with increasing temperature. Due to the reduced formation of complexes at higher ionic strength this effect was decreased and almost diminished at I = 4 mol·L^{-1}.

In Figure 7 (left) the luminescence decay times for Tb(III) in complexes with salicylate and phthalate under indirect excitation conditions are shown. In the experiment the ligands were

used as sensitizers which transfer the energy in a subsequent step effectively to Tb(III). Because the absorption coefficients of the organic ligands are significantly higher compared to the intrinsic Tb(III) absorption coefficients, the sensitization in general is an excellent approach for sensitive luminescence detection of such complexes.

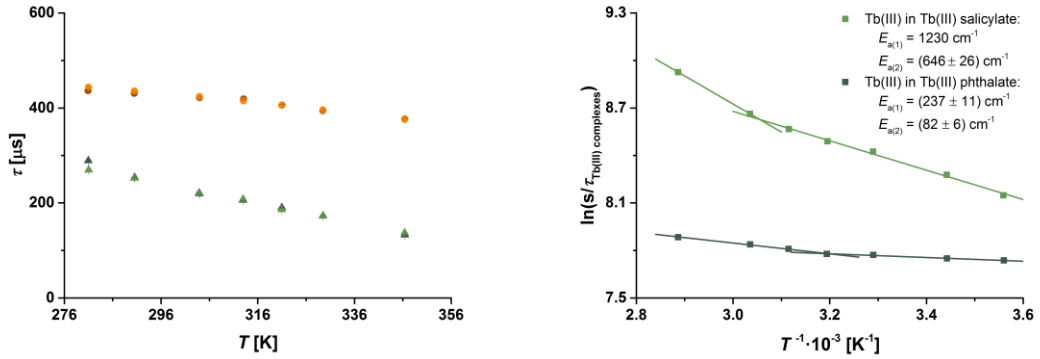

Figure 7: (left) Luminescence decay times of Tb(III) in complexes with salicylate (green triangles) and phthalate (orange circles) (λ_{em} = 545 nm). The decay kinetics were measured for direct (light symbols, λ_{ex} = 378 nm) and indirect (dark symbols, excitation of salicylate with λ_{ex} = 325 nm and of phthalate with λ_{ex} = 330 nm) excitation via the respective ligand for the temperature range of 276 K < *T* < 353 K. (right) Results of the Arrhenius data evaluation for indirect excitation conditions for salicylate and phthalate as ligands for Tb(III).

In Figure 7 the results obtained for direct and indirect excitation condition are compared and it can clearly be seen that there is no difference in the luminescence decay time. Consequently, also the respective Arrhenius data evaluation (Figure 7 (right)) yielded activation energies which were in excellent agreement with data obtained for direct excitation conditions (vide supra). This finding excludes an effective involvement of radiationless deactivation via a charge-transfer (metal-to-ligand or ligand-to-metal charge transfer) reaction, since in this case the direct excitation of the ligand would alter the respective ligand-related redox properties drastically and a different luminescence decay time could be expected. The fact that no difference is observe between both excitation schemes is a supporting evidence that the processes contributing to the depopulation of the Tb(III)-$^5D_4$ state are identical.

In Figure 8 the different radiationless energy transfer pathways (case i) and ii)) contributing to the observed overall reduction of the luminescence decay time of Ln(III) complexes are summarized. The interplay between the different deactivation processes is responsible for the effective overall luminescence decay kinetics and determined by the fastest of such (vide supra).

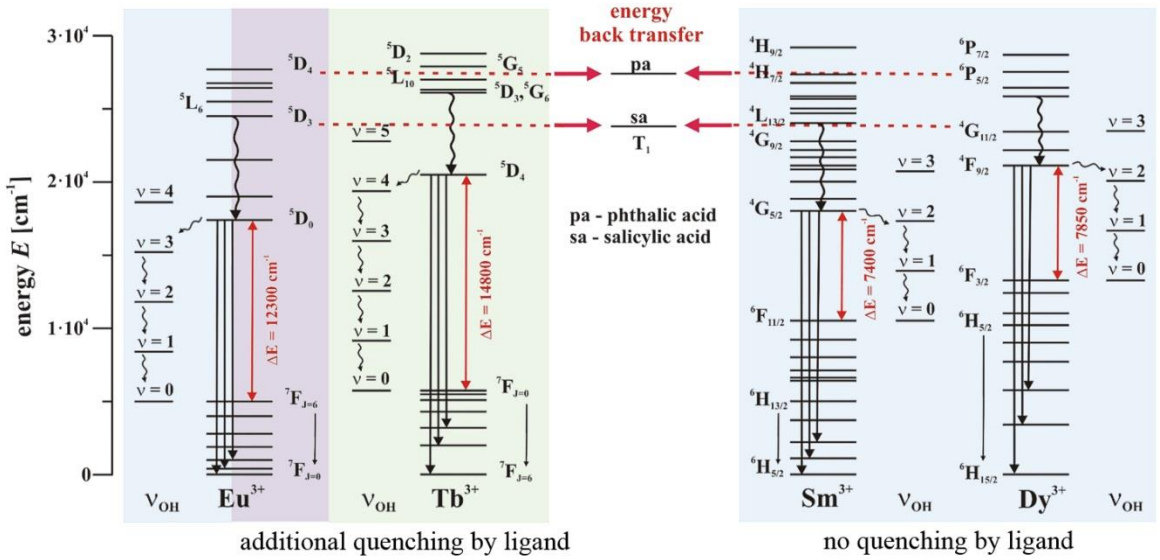

Figure 8: Schematic overview of the Ln(III) energy levels in relation to (overtone) water vibrations or the energy of triplet states of ligands used in the project (energy values taken from [16,17]).

Case iii) deactivation via an intra-complex photoinduced electron transfer (pet) reaction

In addition to radiationless energy transfer processes also the option of an electron transfer (or charge transfer) from ligand to the Ln(III) ion or vice versa should be taken into account. Among the investigated Lanthanides Europium can be found in the oxidation state +II and +III, although under normal conditions for the complexes investigated in aqueous solution only the +III form is observed. This is true for complexes formed and analysed in the electronic ground state. The situation if one of the components (Eu(III) or organic ligand) is in an electronically excited state could be different.

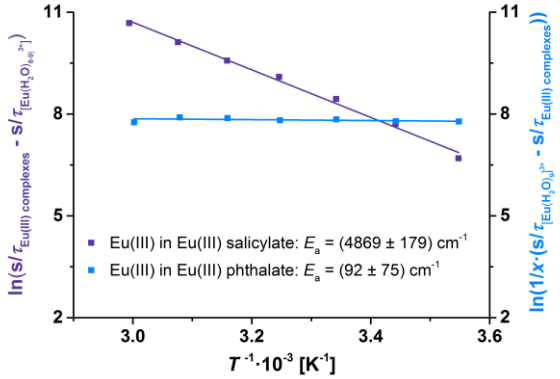

Figure 9: Arrhenius data evaluation of the corrected luminescence decay constants for Eu(III) complexed by salicylate (violett squares) and phthalate (blue squares) (λ_{ex} = 394 nm, λ_{em} = 618 nm).

In Figure 9 the Arrhenius data evaluation of the corrected luminescence decay times for Eu(III) in complexes with salicylate and phthalate is shown. It can be seen that for the two organic ligands a distinctly different temperature dependence was observed. While for the phthalate complexes (almost) a very small activation energy is calculated (resembling the case, in which the remaining water is involved like in the case of Sm(III) or Dy(III), vide supra), for salicylate a

much larger activation energy was determined. Based on transient absorption spectroscopy data for Eu(III) salicylate complexes it was shown that the solvate electron, which can be observed in aquous salicylate solutions upon pulsed laser excitation, is fully quenched.[20] In addition, the Eu(III) luminescence decay time of Eu(III) complexed by salicylate is reduced compared to the Eu(III) aquo complex.[21] Therefore, it is attractive to attribute the observed luminescence quenching by salicylate to an photoinduced electron transfer, in which the Eu(III) is reduced by the photoexcited salicylate to Eu(II). The obtained Eu(II) complex is not stable in aquous solution and decays radiationless further to the starting conditions (Eu(III) salicylate complex).

In summary, the luminescenece decay time is deterimined by a sum of different radiationless deactivaiton processes, of which the fastest determines the overall observed luminescence decay (see eq. (4)).

In order to evaluate luminescecence decay time data properly, the rate determining process needs to be identified. The rate-determining process is a consequence of the interplay between different factors defined by the ligand and the Ln(III) ion. In Figure 10 a summary of the rate-determining processes for the different Ln(III)-complexes investigated is given. In the evaluation of luminescence decay data the presence of rate determining processes has to be introduced. As an example, for Eu(III) the calculation of water molecules based on the empirical Horrocks equation should be modified according to:

$$n_{H_2O} = A \cdot \left(\frac{1}{\tau^{\#}_{H_2O}} - \frac{1}{\tau_{D_2O}} - X \right) \qquad (17) \qquad \text{with} \qquad \frac{1}{\tau^{\#}_{H_2O}} = \frac{1}{\tau_{D_2O}} - k_{pet} \qquad (18)$$

The parameter *X* contains additional contributions, e.g., of ligands in the second coordination sphere (see also eq. (4)).

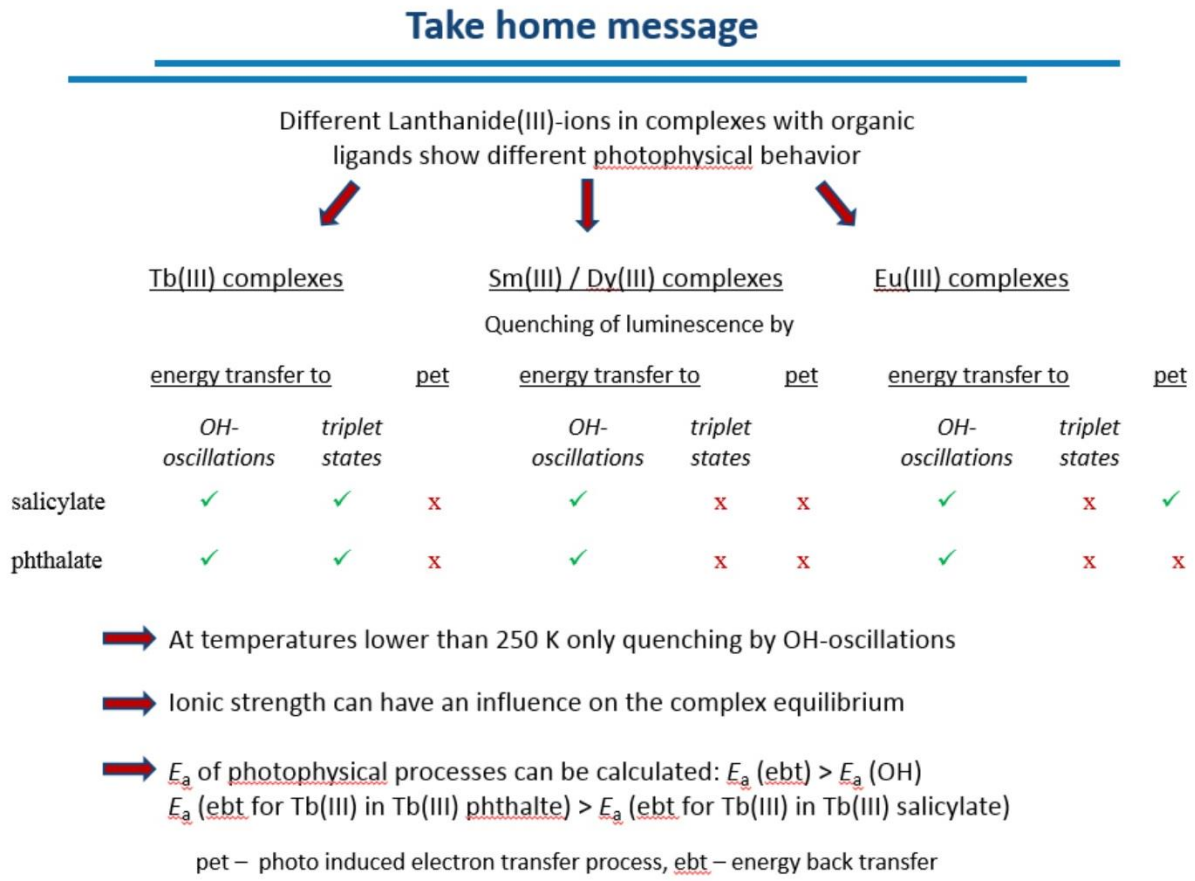

Figure 10: Summary of the contributions of the different radiationless deactivation processes operative in the investigated Ln(III) complexes.

3.2 Refactive index of salt solutions up to *I* = 4 mol·L^{-1}

The refractive index of water containing i) NaCl, ii) $NaClO_4$, and iii) $CaCl_2$ was determined for different ionic strength, different p*H*, and two different temperatures in the wavelength range of 400 nm < λ < 1000 nm (see Figure 11).

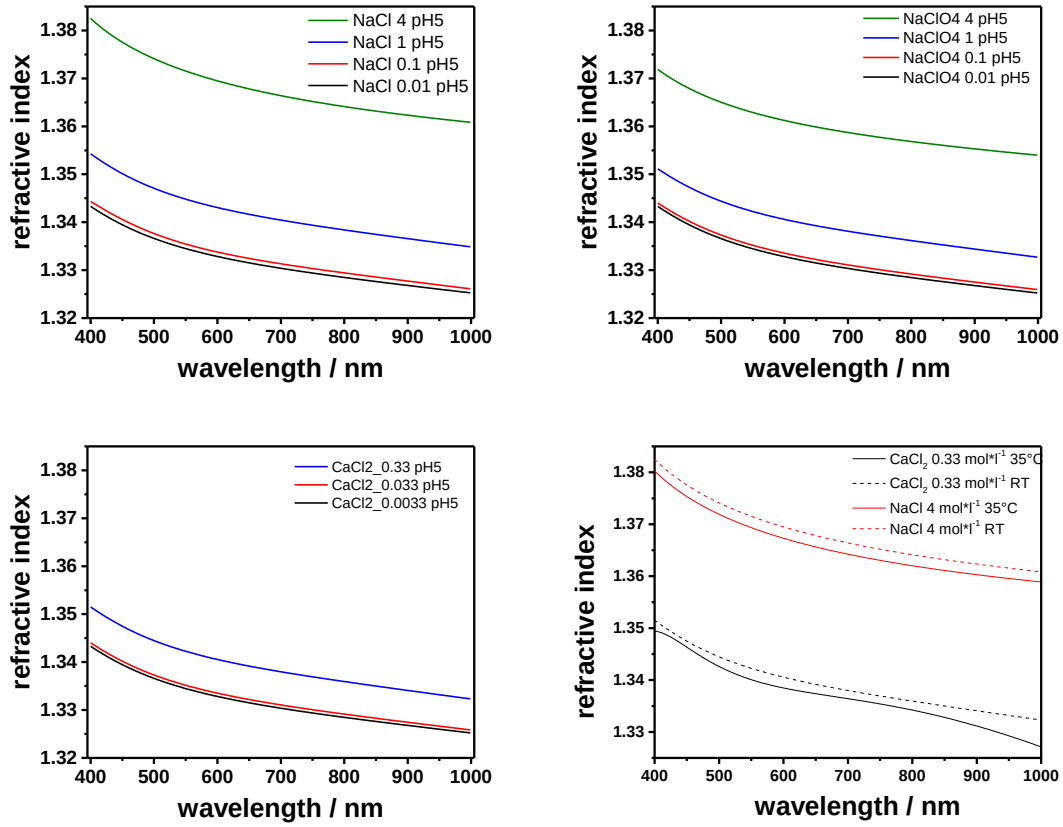

Figure 11: Refractive index of water containing different salts. (Bottom, right) Influence of temperature on the refractive index of solutions containing high concentrations of $CaCl_2$ or NaCl.

The comparison of the salts showed only minor differences in the absolute value for the same ionic strength. On the other hand, the overall ionic strength of the solution had a distinct influence on the refractive index. Especially for high ionic strength solutions the refractive index significantly increased in the monitored spectral range. Moreover, also the temperature of the solution is effecting the refractive index *n* of the solution, however only to a smaller extend comparing the influence of the ionic strength.

These findings have implications on luminescence parameters and subsequently on the quantitative evaluation of such when data of different ionic strength (or salt concentration) are compared quantitatively.

Two frequently used luminescence parameters in speciation analysis are luminescence quantum yield Φ_L (or for simplification often the luminescence intensity) and the luminescence decay time τ. Both parameters are connected by

$$\Phi_L = \frac{\tau}{\tau_0} \tag{19}$$

τ_0 (and τ) are defined by the Einstein coefficients A_{21} and B_{12}, respectively. Taking the theory into account the rate constant for the luminescence k_L can be written as

$$k_L = \frac{1}{\tau_L} = \frac{8000 \cdot \pi \cdot c_0 \cdot \ln 10}{N_A} \cdot \frac{n_L^3}{n_{abs}} \cdot \frac{g_{ex}}{g_L} \cdot \left\langle \nu^{-3} \right\rangle^{-1} \cdot \int \frac{\varepsilon(\nu)}{\nu} \cdot d\nu \tag{20}$$

Depending on the difference between excitation and emission wavelength the dispersion may be neglected. In that case a rough approximation according to Strickler and Berg for the luminescence decay time can be performed:

$$\frac{1}{\tau_L} = 2.88 \cdot 10^{-9} \cdot n^2 \cdot \int \frac{(2 \cdot \nu_c - \nu)^3}{\nu} \cdot \varepsilon(\nu) \cdot d\nu \tag{21}$$

From eq. (21) a quadratic dependence of the reversed luminescence decay time on the refactive index n is predicted. By looking at the extreme values for I = 0.1 mol·L^{-1}and 4 mol·L^{-1}, respectively, a change in τ of 5 - 10% can be expected due to the variation in the refractive index. So, for decay time based speciation this needs to be taken into account when results of different ionic strength samples are compared. Sine τ is correlated with the luminescence quantum efficiency (and therefore, also with intensity) via eq. (19) this affects also this luminescence parameter.

Based on the data acquired (see Figure 11) this correction can be easily carried out, which will help to further improve the precision of luminescence based speciation.

3.3 Complexation of Lanthanides by borate

Borates have been identified as a potential ligand in nuclear waste repositories. Especially in salt formations, which are one of the major geological formations evaluated. In addition to mineral as natural sources, boron is also a constituent of materials used in the nuclear technology process (e.g., borosilicate glass coquilles; boron as part of the cooling water becomes part of the spent nuclear fuel inventory to be stored). Therefore, the formation of boron complexes with Lanthanide complexes was investigated. In aqueous systems $B(OH)_3$ and polyborates are potential interaction partners for metal ions such as Ln(III). The aqueous chemistry of $B(OH)_3$ is complex, while at concentrations $c < 0.025$ mol·L^{-1} only boric acid and its different anions is found, at higher concentrations (and depending on the p*H* of the solution) a number of different polyborates are formed and dominantly found in the system (see Figure 12).

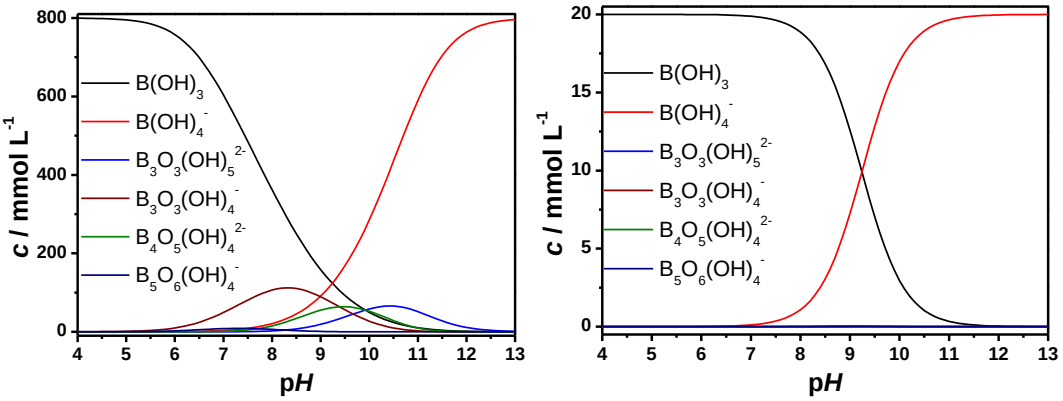

Figure 12: (left) speciation of borate for c = 0.8 mol·L^{-1} and (right) for c = 0.02 M based on data taken from [22] and calculated using ChemEQL 3.0[23].

In Figure 13 the luminescence spectra of Eu(III) at increasing borate concentrations (0 mol·L^{-1} < c(BS) < 0.02 mol·L^{-1}) are shown. In this concentration range (and p*H*) no formation of polyborate species is expected (s. also Figure 12 (left)). In the left part of Figure 13 the Eu(III) luminescence spectra are depicted. It can be seen that the spectral intensity distribution is not change by the presence of borate up to concentrations of 0.02 mol·L^{-1}. This was found for all samples investigated at p*H* < 7.

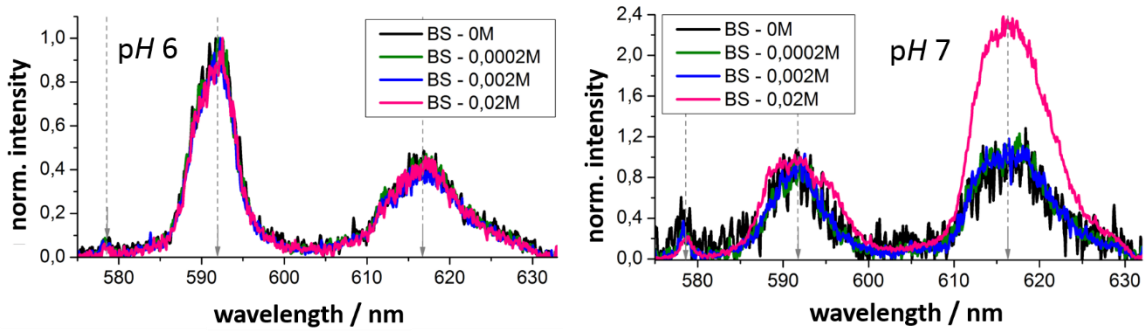

Figure 13: Luminescence spectra of Eu(III) (λ_{ex} = 394 nm, c(Eu(III) = 0.4 mmol·L^{-1}) in the presence of increasing borate (BS) concentration at two p*H* values.

At p*H* = 7 at the highest borate concentration investigated an alteration in the spectral intensity distribution was observed (see Figure 13 (right)), which indicates that the coordination sphere of Eu(III) is changed by the complexation of borate. Based on measurements of the luminescence decay kinetics the corresponding decay times were determined for different borate concentrations and p*H*.

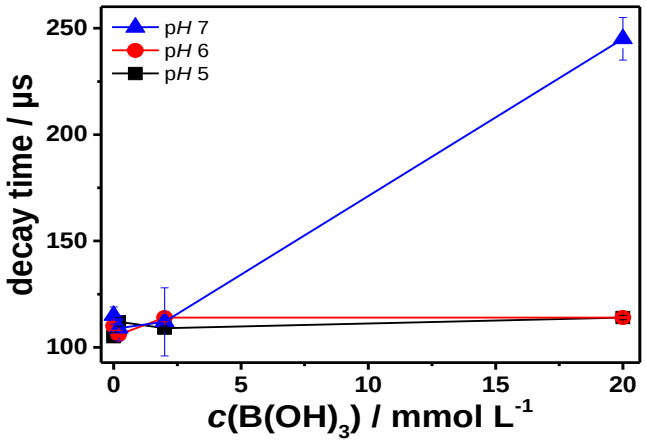

Figure 14: Luminescence decay time τ of Eu(III) (λ_{ex} = 394 nm, λ_{em} = 613 nm) in the presence of borate at three different p*H* (after three days of equilibration).

From Figure 14 can be concluded that also the luminescence decay kinetics of Eu(III) is not altered due the presence of borate in the investigated concentration range for p*H* < 7. Only at p*H* = 7 and high borate concentration a distinct alteration of τ was found, which perfectly corroborates the results of the spectra analysis. Based on the empirical relationship (see e.g., eq. (17)) the number of water molecules substituted by the borate in the first coordination sphere of Eu(III) was estimated to 2 - 3. However, the possible influence of the borate itself on the Eu(III) luminescence decay kinetics has to be kept in mind (vide supra for the detailed discussion of ligand-related radiationless deactivation). Here, further research is necessary.

For p*H* = 7 also the aging of the samples was investigated. In Figure 15 (left) the alterations observed in the spectral intensity distribution after five days are shown. Compared to Figure 13 (right) additional spectral features are observed. In addition the spectral intensity distribution changes also the luminescence decay kinetics were altered. Here, a further increase with longer contact time was found, e.g., for the sample containing 20 mmol·L^{-1} boric acid (p*H* = 7) the luminescence decay time increased to τ = 380 µs after one week equilibration time. These samples were stored under ambient conditions. In order to test the influence of CO_2 experiments with samples prepared with and without CO_2 were investigated.

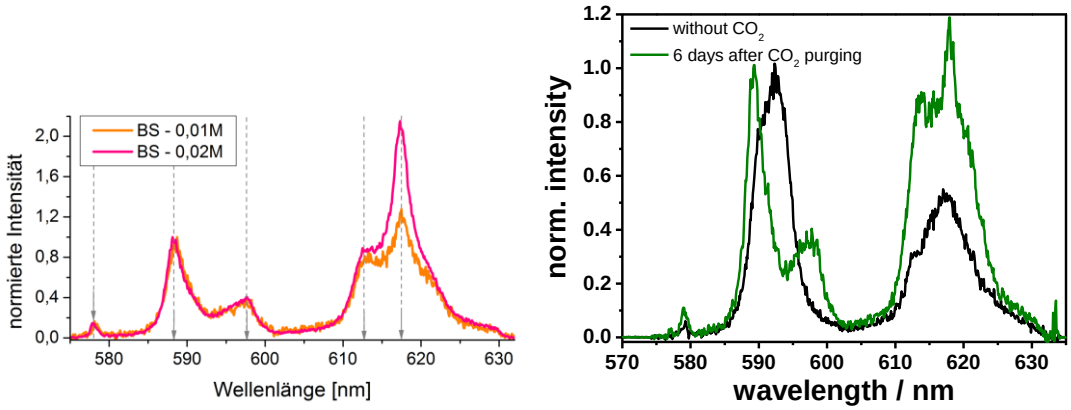

Figure 15: (left) Eu(III) luminescence spectra (λ_{ex} = 394 nm, p*H* = 7, RT) of Eu(III) borate solutions after five days of contact time under ambient conditions are shown. (right) Influence of CO_2 on the Eu(III) luminescence spectra in the presence of borate (*c* = 0.02 mol·L^{-1}, p*H* = 7).

In Figure 15 (right) the effect of CO_2 after six days of contact is shown. The comparison with the spectra on the left shows a strong resemblance and makes it tempting to attribute the observed spectral changes to the formation of mixed complexes between Eu(III), borate, and CO_2, respectively. For the aged samples also a slow precipitation of a white solid over weeks was observed indicating that a water insoluble complex is formed. At p*H* =7 (and below) at concentrations *c* < 0.02 mol·L^{-1} borate is a weak ligand and cannot compete with other ligands like low molecular weight organic acids. This has been shown in competition experiments with glycolic acid as a model ligand.

In collaboration with the Technical University of Dresden and the Helmholtz Center Dresden Rossendorf also the interaction of Eu(III) with polyborates at p*H* < 6 was investigated. Here, site-selective luminescence spectra recorded at *T* = 5 K proved to be especially valuable in the identification of different Eu(III) polyborate complexes formed in the investigated system. For a detailed description of experiments performed please referrer to the report of the Technical University of Dresden.[24] As an example in Figure 16 the different luminescence spectra (at room temperature and under site-selective excitation conditions at *T* = 5 K) of solid Eu(III) borate samples obtained from the solutions are shown.

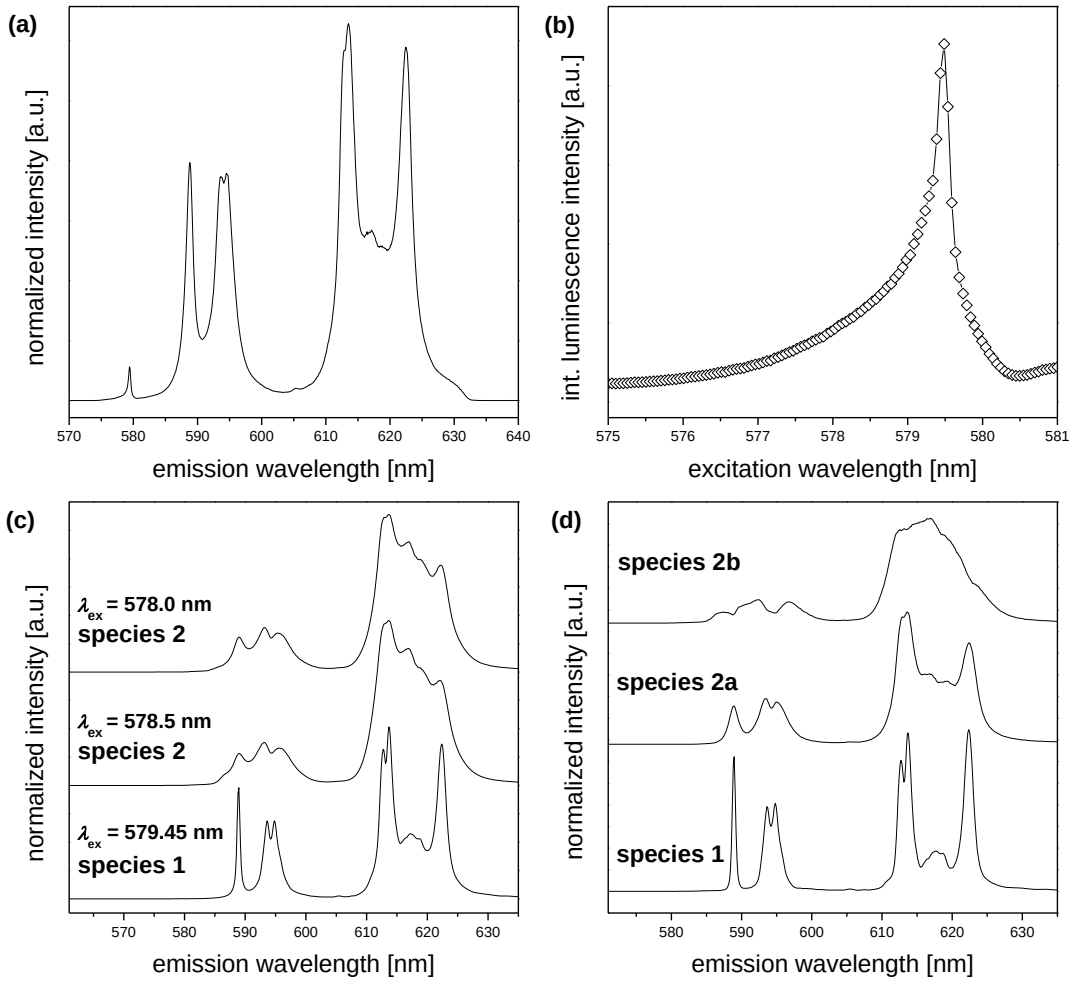

Figure 16: Solid-state luminescence spectra of the solid Eu(III) borate: (a) emission spectrum recorded at RT (λ_{ex} = 394 nm), (b) excitation spectrum at *T* = 5 K, (c) emission spectra (λ_{ex} = 578.0 nm, 578.50 nm and 579.45 nm, respectively, *T* = 5 K), (d) emission spectra determined from the PARAFAC analysis of the time-resolved spectra at *T* = 5 K (λ_{ex} = 578.50 nm and 579.45 nm, respectively).

In summary, the possible impact of borate on the mobilization of Actinide(III) ions in a nuclear waste repository is expected to be small. Based on the results, borates have only a minor mobilization potential for trivalent Actinides in the slight acidic to neutral p*H* range since the complexation is very weak - especially in comparison to other ligands, *e.g.*, carbonate, hydroxide and other organic compounds present in the system. Moreover, due to the formation of solid (poly)borate phases already at slight acidic p*H* the immobilization of trivalent Actinides will be supported. Future research is required to investigate the actinide-borate interactions in the alkaline p*H* range in detail.

3.4 Interactions of Europium(III) with natural occurring polymers

Organic material, especially polymeric organic material is an important complexing agent as natural organic polymers, like humic substances (HS), are ubiquitous in the environment. The ground and pore waters in North Germany lower cretaceous clays have relatively high salt concentrations.[25] In the following the complexation of Eu(III) as Ln(III) ion by different HS in solutions with different background electrolytes and different electrolyte concentration was investigated.

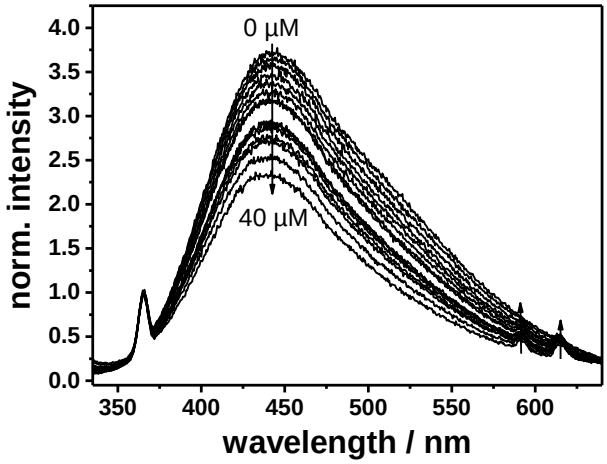

Figure 17: Typical fluorescence of a humic substance. Shown is a fluorescence spectrum of Pahokee Peat Fulvic Acid with a concentration of 10 mg·L^{-1} in 0.5 mol·L^{-1} NaCl solution at p*H* = 5. Excitation was at λ_{ex} = 325 nm. The arrows indicates the changes upon increasing Eu (III) concentration from 0 µmol·L^{-1} to 40 µmol·L^{-1}.

Figure 17 shows a typical fluorescence spectrum of HS. By increasing the Eu(III) concentration from 0 µmol·L^{-1} to 40 µmol·L^{-1} the intrinsic HS fluorescence intensity is quenched. Around 600 nm two peaks (located around 592 nm and 615 nm) show increasing intensity with increasing Eu(III) concentration. These two peaks arises from the luminescence of the Eu(III) ions, which is excited via HS molecules. From this measurement, the conditional complexation constant can be derived using eq. (10).

To calculate conditional binding constants by the use of eq. (10), the measured fluorescence intensity at every Eu(III) concentration is added up from 425 nm to 475 nm and divided by the integrated fluorescence intensity in absence of Eu(III). This approach gives plots as shown in Figure 18. By non-linear least square fitting of eq. (10) to the data, values for the conditional complexation constant and the remaining fluorescence $I_{ML,rel}$ could be derived. In Figure 18 experimental data (points) and the result of the fitting procedure (straight lines) for the complexation of Eu(III) ions by Pahokee Peat Fulvic Acid are shown.

These measurements were conducted for the humic acid (HA) and fulvic acid (FA) fraction of Pahokee Peat (PP) and Suwannee River (SR) humic substances. In the investigation mainly two different ionic strengths (0.5 mol·L^{-1} and 3.0 mol·L^{-1} NaCl) at different temperatures (room temperature, 35 °C and 50 °C) were considered.

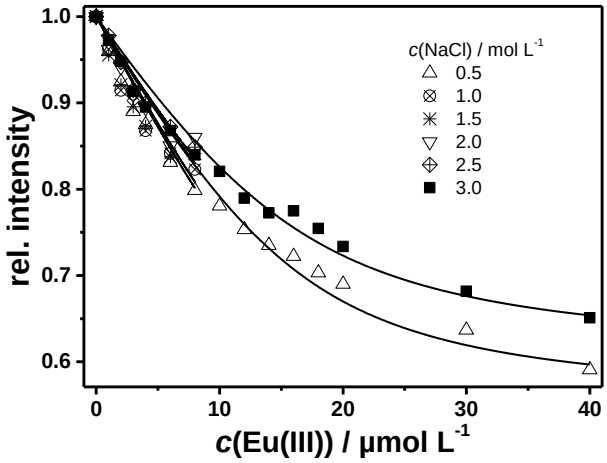

Figure 18: Plot of the relative intrinsic fluorescence intensity of Pahokee Peat Fulvic Acid at p*H* = 5 as function of the Eu(III) concentration and different concentrations of NaCl as background electrolyte as given in the legend. The straight lines are the results of a non-linear least square fitting of eq. (10) to the data.

The complexation of Eu(III) ions by SRFA and SRHA as well as PPFA and PPHA was investigated by stationary fluorescence measurements in dependence of ionic strength and temperature. From Figure 19 it clearly can be seen, that the complexation is stronger for PP than for SR as the lg β values are one unit higher for PP. For the effect of temperature and ionic strength no clear trends were found. Neither an increase of ionic strength from 0.5 mol·L^{-1} to 3.0 mol·L^{-1} nor of temperature from 22 °C to 50 °C gave a pronounced effect on the conditional complexation constants.

A crucial parameter is – besides the very fundamental assumption of a 1:1 complexation – the concentration of the ligand / binding sites in the HS. The approach was to calculate this concentration from the charge density of the HS at the given p*H*. But this charge density is known only at room temperature. The calculation of complexation constants requires in principle knowledge about the activities of ligands and metal ions. In this approach, concentration are used instead. Theories, like SIT[f] or Pitzer, allow to calculate activity coefficients for ions in solution. But these attempt will fail for HS as HS are complex mixtures of an unknown number of pieces.

In the following, the interaction of HS with Ln(III) ions will be investigated on a more mechanistic level. In addition to Eu(III) also Lanthanum(III) (La(III)) and Neodymium(III) (Nd(III)) were included in the study. The aim was to derive average distances between complexed Ln(III). Hereby, a more intrinsic parameter is at hand, which will help to describe the interaction on a molecular level.

[f] Specific Interacion Theory

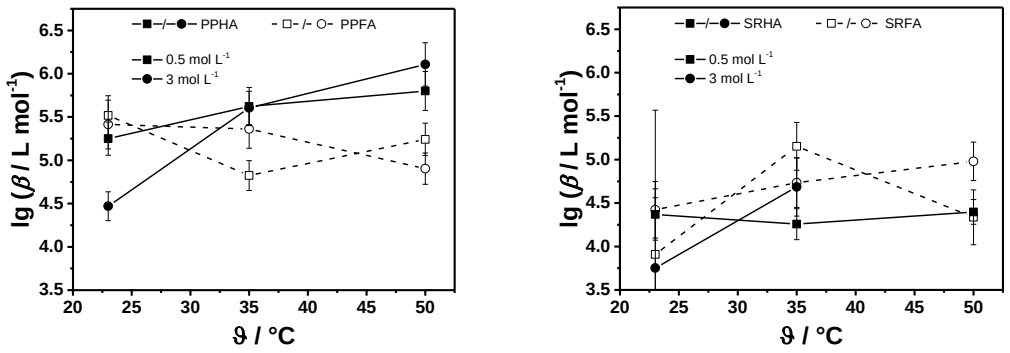

Figure 19. Conditional constants for the complexation of Eu(III) ions by the FA and HA fractions of PP (left) and SR (right). The concentration of the humic substance was 10 mg·L^{-1} at p*H* = 5.

As representative, HA from the Gorleben site – Gohy573 FA and Gohy573 HA – were chosen. The question was, how the composition of the background electrolyte influences the interaction of the Ln(III) ions with Gohy573 HA and Gohy573 FA, respectively. As background electrolyte NaCl and $MgCl_2$ were used. At the beginning of the investigations it was recognized, that the $MgCl_2$ influences the intrinsic fluorescence of the humic material. This also showed up by addition of Eu(III) ions to solutions containing Gohy573 FA or HA and $MgCl_2$ as background electrolyte. Contrary to the comparable measurements, as shown in Figure 17 and Figure 18, with NaCl as background electrolyte no pronounced decrease of the intrinsic fluorescence intensity could be observed upon addition of Eu(III) ions. As the intrinsic fluorescence of HS is very broad and featureless – a result of their complex and heterogeneous structure – it is not the best observable to study interactions between Ln(III) ions and HS in detail. In contrast, some Ln(III) ions have a distinct luminescence emission, which is altered due to changes in their chemical environment, for example due to complexation reactions.

Eu(III) was used as luminescence probe in the experiments and was excited indirectly via HS molecules. Consequently, only Eu(III) complexed to chromophors of the HS are monitored. Here, the humic substance molecules act as a so called antennae, which collect the excitation light and transfer it to the Eu(III) ion. The excitation of the Eu(III) via HS is more efficient than a direct excitation of the Eu(III) ions as the extinction coefficients of the latter are very low (ε < 3 L·mol^{-1}·cm^{-1})[6].

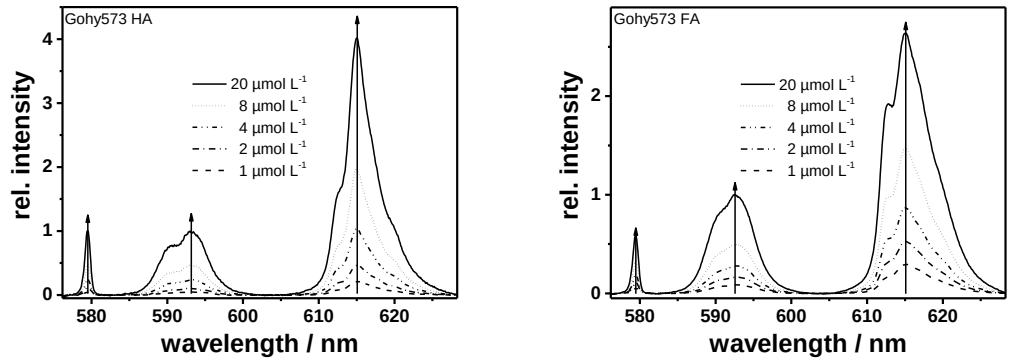

Figure 20: Luminescence spectra of Eu(III) at different Eu(III) concentrations in solution with 12.5 mg·L^{-1} HS and 0.1 mol·L^{-1} $MgCl_2$ at p*H* = 5, λ_{ex} = 356 nm.

In Figure 20 luminescence spectra of Eu(III) in solutions with Gohy573 HA and Gohy573 FA are shown after indirect (sensitized) excitation via HS at λ_{ex} = 356 nm. By increasing the Eu(III) concentration also the intensity of the Eu(III) luminescence increases. Due to the excitation scheme, only Eu(III) ions, which are complexed to humic substance molecules, will show luminescence. Therefore, an increase in luminescence intensity means also that more Eu(III) ions are complexed to the humic substance.

The Eu(III) luminescence spectra show differences for the complexation of Eu(III) by Gohy573 FA and Gohy573 HA. What clearly can be seen is that the intensity of the $^5D_0 \rightarrow ^7F_2$ transition (around 615 nm) is higher relative to the intensity of the $^5D_0 \rightarrow ^7F_1$ transition (around 592 nm) for Eu(III) complexed to Gohy573 HA. For the highest Eu(III) concentrations, the relative intensity of the $^5D_0 \rightarrow ^7F_2$ transition increases up to four for Gohy573 HA and only to 2.6 for Gohy573 FA. Also the coordination geometry of the complexes formed must be different as the luminescence spectra looks different. In Eu(III) Gohy573 HA complexes, the $^5D_0 \rightarrow ^7F_0$ transition has nearly the same intensity as the $^5D_0 \rightarrow ^7F_1$ transition, whereas for Eu(III) Gohy573 FA complexes the $^5D_0 \rightarrow ^7F_0$ transition has only half of the relative intensity compared to the $^5D_0 \rightarrow ^7F_1$ transition. In addition, the splitting of the $^5D_0 \rightarrow ^7F_1$ and $^5D_0 \rightarrow ^7F_2$ transition show slightly differences for FA and HA as complexing ligands. For comparison both luminescence spectra at the highest Eu(III) concentration (20 µmol·L^{-1}) are plotted in one diagram (cf. Figure 21).

Each ^7F_J states split in a ligand field in up to *2J+1* energetically different sublevels, known as Stark levels. Depending on the energy differences of these Stark levels and the symmetry, in which the Eu(III) ion is embedded, the splitting can also be seen in the luminescence spectra. Görller-Wallrand and Binnemans summarized, how luminescence excitation or emission spectra can be used to derive the symmetry of the Eu(III)'s ligand field in single crystals.[26]

However, this approach to deduce the symmetry of Eu(III) species in the presence of HS will fail, as it cannot be expected that only one specific Eu(III) complex will be formed. Nevertheless, from the luminescence emission spectra shown in Figure 21 differences in the splitting of

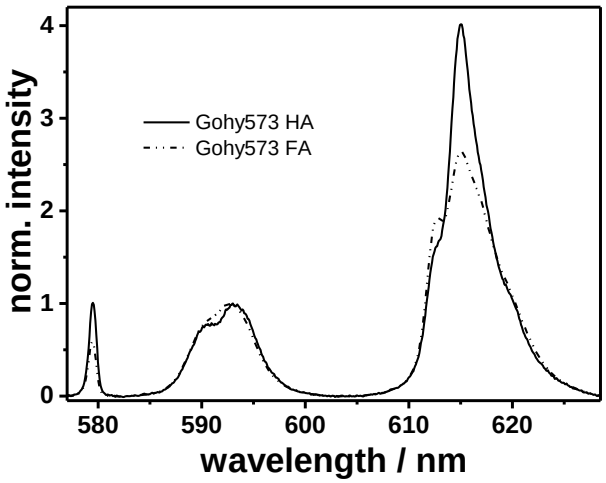

Figure 21: Comparison of the normalized luminescence spectra of Eu(III) complexed by Gohy573HA and Gohy573 FA, respectively, *c*(Eu(III) = 20 µmol·L^{-1}.

the $^5D_0 \rightarrow {}^7F_1$ and $^5D_0 \rightarrow {}^7F_2$ transitions depicted. Interestingly enough, in the luminescence spectrum of Eu(III) Gohy573 HA complexes the splitting of the $^5D_0 \rightarrow {}^7F_1$ transition is better resolved (two local maxima) compared to Eu(III) complexes with Gohy573 FA (one maximum and a shoulder). The opposite trend is found for the luminescence transition $^5D_0 \rightarrow {}^7F_2$. Here, for Eu(III) Gohy573 HA complexes a maximum with two shoulders is found, whereas for Eu(III) Gohy573 FA complexes two local maxima can be seen and a shoulder on the bathochromic side of the peak can be anticipated.

A parameter easier accessible is the asymmetry ratio *r* (cf. eq. (2)), which is more straight forward to compare different Eu(III) luminescence spectra. For the luminescence spectra shown in Figure 20 this parameter was calculated and plotted in Figure 22. For both, complexation by Gohy573 HA or Gohy573 FA, the asymmetry ratio decreases slightly by background electrolyte ($MgCl_2$) concentration of 0.10 mol·L^{-1} with increasing Eu(III) concentration. When increasing the concentration of $MgCl_2$ to 0.85 mol·L^{-1}, the decrease of asymmetry ratio *r* is stronger.

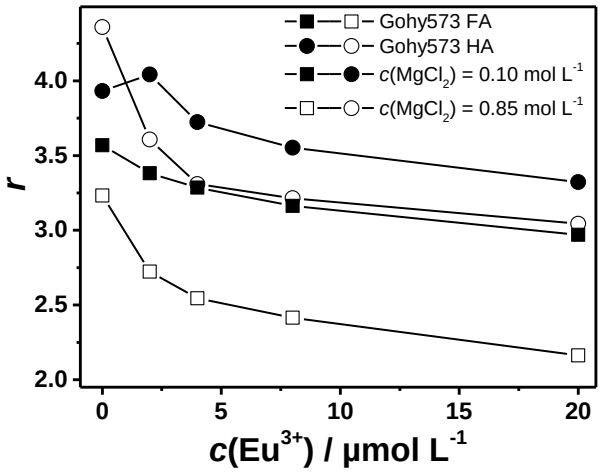

Figure 22: Asymmetry ratio *r* calculated with eq. (2) extracted from luminescence spectra of Eu(II) complexed to Gohy573 FA or Gohy573 HA at different concentration of $MgCl_2$ as background electrolyte. Excitation of the Eu(III) luminescence at 356 nm, p*H* = 5, *c*(HS) = 12.5 mg·L^{-1}.

By increasing the Eu(III) concentration, more and more binding sites of the HS are occupied. One approach to describe the interactions of HS with protons or metal ions is the NICA Donnan model.[27,28] In this model two kinds of binding sites – a stronger and a weaker one – are assumed, which allow specific interactions between humic substance molecules and metal ions. Non-specific interactions are also taken into account by including a Donnan sub-model in this approach. The decreasing trend of the asymmetry ratio can be interpreted in these terms. At low Eu(III) concentrations, most of the Ln(III) ions are expected to be coordinated by strong binding sites, which produce a stronger ligand field and hence a more intense $^5D_0 \rightarrow {}^7F_2$ transition – due to its hypersensitive character – will show up in the luminescence spectrum. With increasing Eu(III) concentration also weaker binding sites are involved in the complexation. This reduces the intensity of the hypersensitive transition and hence the value of the asymmetry ratio *r*.

An increase of the background electrolyte concentration has at least two effects. On one hand, the number of competing metal ions for binding sites is increased. On the other hand, HS can also be understood as polyelectrolytes and consequently the increase in ionic strength will also affect the humic substance conformation. As can be seen in Figure 22 the increase of the background electrolyte concentration leads to a decrease of the asymmetry ratio *r*. At lower $MgCl_2$ concentrations (less than 10 mmol·L^{-1}) no influence on the asymmetry ratio *r* was observed. Both findings are in accordance with the general trends discusses so far. A similar behavior for the complexation of Eu(III) ions by Gohy573 HA in solutions containing Ca(II) was found.[29,30] In these experiments, KNO_3 was used to control the ionic strength and $Ca(NO_3)_2$ was added. At Ca(II) concentration below 1 mmol·L^{-1} the asymmetry ratio *r* remains constant as the amount of bound Eu(III) is not affected. At higher Ca(II) concentrations a decrease of *r* was observed and accounted to a replacement of Eu(III) ions by Ca(II). The changes in *r* was led back to changes in the humic substance conformation.

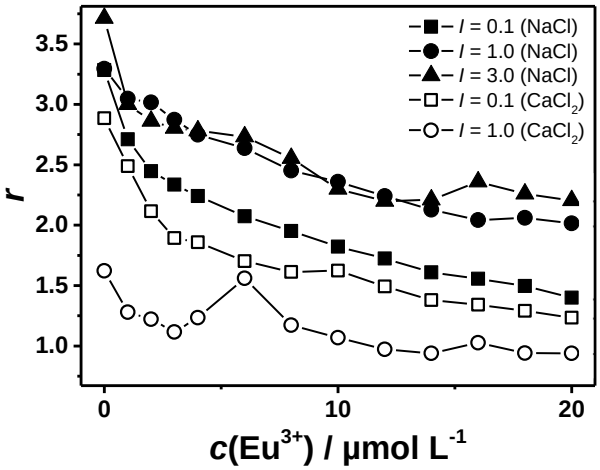

Figure 23: Asymmetry ratio *r* (left) of Eu(II) complexes with SRFA in aqueous solution containing different concentrations of background electrolyte (NaCl or $CaCl_2$) . The ionic strength of *I* = 0.1 mol·L^{-1} (1.0 mol·L^{-1}) for $CaCl_2$ corresponds to *c*($CaCl_2$) = 0.033 mol·L^{-1} (0.33 mol·L^{-1}). λ_{ex} = 325 nm, p*H* = 5.

The background electrolyte acts not only due to the number of ions in solution. In Figure 23 the effect of $CaCl_2$ and NaCl as background electrolytes on the luminescence asymmetry ratio *r* is compared. The ionic strength was chosen to lie within *I* = 0.1 mol·L^{-1} and *I* = 3.0 mol·L^{-1}. The increase of the NaCl concentration leads to a shift of *r* to greater values, whereas increasing of the $CaCl_2$ concentration showed the opposite trend. In this case *r* decreases. At comparable ionic strength for $CaCl_2$ and NaCl (*I* = 1.0 mol·L^{-1}) the value of the asymmetry ratio *r* was distinctly lower in Eu(III) luminescence spectra arising from complexes with SRFA in $CaCl_2$ containing solutions. The main difference in both electrolyte systems is the charge of the cation. A single positive charged ion like Na(I) has only one valency for interaction with opposite charged ions, whereas Ca(II) can interact with more than one opposite charge. It is conceivable that this opens the possibility to link humic substance molecules together, which will have significant effects on further interactions with metal ions like Ln(III) ions. As already discussed, above a certain concentration the cations from the background electrolyte itself become strong competitors for binding sites, which leads to a displacement of the Eu(III) ions.

To account for macromolecular effects, such as changes in conformation, the measurement of distances between binding sites might be a good indicator. But these distances are hardly to measure. A way out is to measure them indirectly by the distances between bound Ln(III) ions. This can be achieved by applying the ILTE.

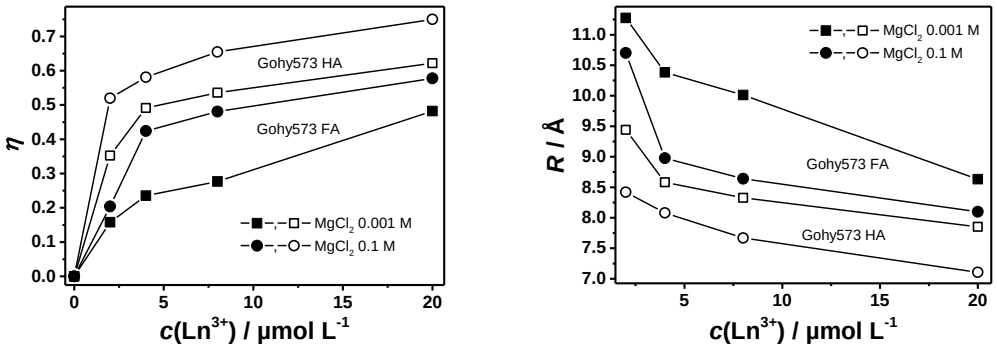

Figure 24: Energy transfer efficiencies (left) as calculated from steady state measurements according eq. (8) and resulting distances using eq. (7) with R_0 = 8.53 Å as published by Horrocks et al.[7]. See text for details of experimental procedure.

To solutions containing Eu(III) and Gohy573 HA or Gohy573 FA, respectively, La(III) or Nd(III) ions were added. It is known, that Nd(III) can quench the Eu(III) luminescence by an ILET based on an Förster resonance energy transfer mechanism depending on the distance between both ions.[7] La(III) itself will not quench Eu(III)'s luminescence as it is no suitable acceptor for such a transfer of energy. In the experiments 5 µmol·L^{-1} of Eu(III) and 12.5 mg·L^{-1} HS were mixed and allowed to form complexes. Subsequently, in two sets of experiments La(III) and Nd(III) ions, respectively, were added. In both cases, the Eu(III) luminescence intensity changes. In case of adding La(III) ions, the changes are due to effects of competition for binding sites and of alteration in the HS conformation, which could have an influence on the sensitization process as well as on the binding site of Eu(III). It is assumed, that the addition of Nd(III) ions has the same impact on the humic substance and on the bound Eu(III). But, additionally Nd(III) can quench the luminescence of Eu(III) due to an operative energy transfer between both ions. To evaluate the efficiency of the energy transfer carefully, measurements with La(III) and Nd(III) are necessary. The changes in luminescence intensity, when adding La(III) reflects the behavior of the Eu(III) luminescence without contribution of an acceptor and is in eq. (8) denoted as I_D. The experiment with adding Nd(III) to the solutions gives the values for I_{DA}. Based on these prerequisites the calculated energy transfer efficiency is shown in Figure 24 (left). With a Förster distance R_0 taken from the literature[7], the energy transfer efficiency could be transformed into distances between bound Eu(III) and Nd(III) as shown in Figure 24 (right). Independent of the HS or of the ionic strength, the addition of Ln(III) ions to the Eu(III) HS complexes results in a decrease of the inter-lanthanide distances. This is reasonable as more binding sites are occupied. Therefore, the mean distance between them has to decrease. An increase in ionic strength yields to an overall decrease of the distances. This could be a result from alterations in the conformation of the HS due to processes like coagulation or folding, both known macromolecular effects.

3.5 Interactions of Europium(III) with natural occurring polymers

One of the main challenge one has to deal with when working with HS is their chemical heterogeneity. A way to overcome this circumstance is to use model substances, which represents substructures of HS and address certain properties. One kind of model substances are low molecular weight compounds, such as substituted benzoic acids or substituted phenyl moieties, which are known as basic structures in HS (cf. Scheffer/Schachtschabel, page 57).[31] It is attractive to assume, that these type of substructures accounts for the photophysical behavior and primary complexation moieties in HS. By investigating complexes of Ln(III) ions with these compounds basic photophysics of Ln(III) HS complexes can be mimicked and studied. But low molecular weight compounds cannot model macromolecular effects involved in the complex formation. For this purpose, another type of model compounds has to be considered. In a first attempt, poly(acrylic acid) (PAA) was chosen.[32(Appendix B-7)] The complexation of Ln(III) ions by PAA was of interest. By making use of the ILET, distances between coordinated Ln(III) ions could be calculated. The calculated distances showed a dependence on p*H* as well as ionic strength. From this an influence due to conformation alterations upon Ln(III) complexation and hence macromolecular effects could be concluded. Although with PAA macromolecular effects could be addressed, effects like sensitization of Ln(III) luminescence could not be mimicked.

Therefore, an attempt to investigate both parameteres, a novel model polymer was utilized, in which macromolecular behavior and a substructure, which accounts for the photophysical behavior of HS, were combined. As monomer 4-vinylbenzoic acid was chosen. In a radical polymerization[g] with 4,4'-azobis(4-cyano-pentanoic acid) as initiator two polymers with different chain length were synthesized. Gel permeation chromatography gave peak molecular weights M_p of 5 200 g·mol^{-1} and 17 000 g·mol^{-1} for the short-chain (PVBA 52 00) and the long-chain (PVBA 17 000) polymer, respectively.

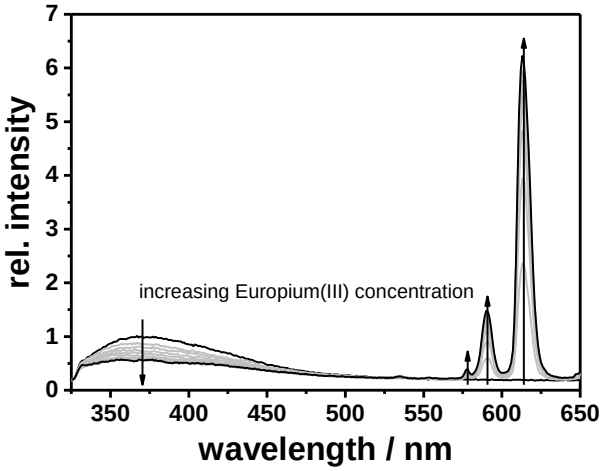

Figure 25: Stationary luminescence spectrum of PVBA 5200 upon addition of Eu(III). c(PVBA 5200) = 50 mg·L^{-1}, λ_{ex} = 288 nm, p*H* = 6.5, 1 mol·L^{-1} NaCl as background electrolyte. Eu(III) concentration was increased from 0 µmol·L^{-1} to 20 µmol·L^{-1}.

[g] see experimental part

The fluorescence emission of the synthesized polymer – plotted in Figure 25 – shows similarities to the fluorescence emission of a humic substance upon addition of Eu(III) ions. A relatively broad fluorescence emitted between 330 nm < λ < 500 nm could be observed after excitation at 288 nm. Compared to HS (cf. Figure 17) the emitted fluorescence is higher in energy and not as broad compared the humic substance fluorescence. Interestingly, a sensitization of the Eu(III) luminescence was observed. Both, the broad fluorescence and sensitization abilities makes PVBA to an interesting polymeric model compound for HS.

In Figure 26 the absorption spectra between 275 nm < λ < 310 nm of Ln(III) ions used in this study are compared. As the extinction coefficients are very small at 288 nm, a direct excitation even at the highest used Ln(III) concentrations c(Ln(III)) = 20 µmol·L^{-1} is very unlikely.

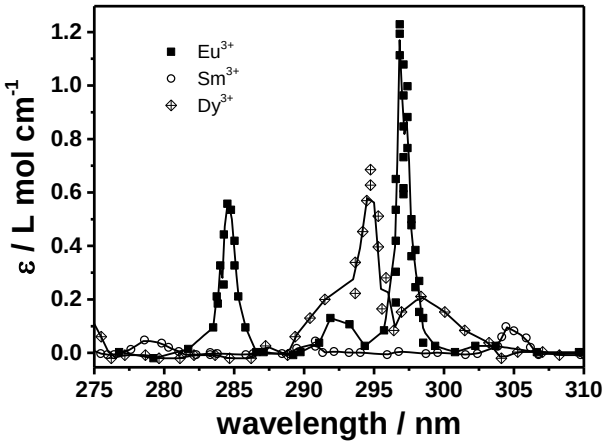

Figure 26: Part of the absorption spectra of Eu(III), Sm(III) and Dy(III) ions in aqueous solution. Data points were extracted from absorption spectra given in literature[6]. The straight lines are the result of a linear interpolation of these data points.

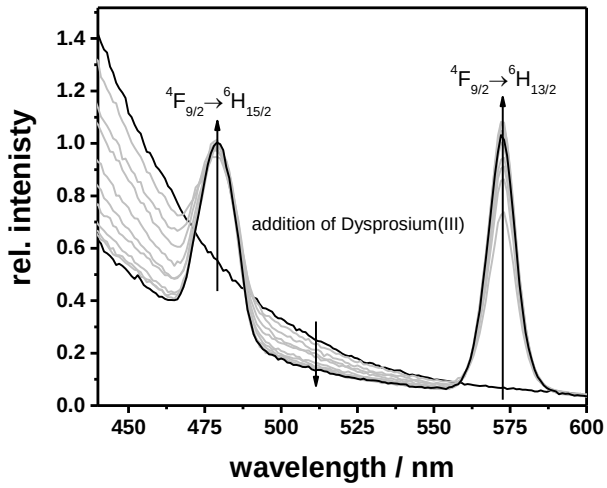

Figure 27: Stationary luminescence spectrum of PVBA 5 200 without and upon addition of Dy(III) ions. Dy(III) concentration was increased up to 20 µmol·L^{-1}. λ_{ex} = 288 nm, pH = 6.5, c(PVBA 5 200) = 50 mg·L^{-1}.

The sensitization experiments were also carried out with Sm(III) and Dy(III). Both Ln(III) ions have much shorter decay times (cf. Table 2) due to a more effective quenching of their luminescence in aqueous solution. Comparable to the measurements with Eu(III) the luminescence

of Sm(III) or Dy(III) could be sensitized via the PVBA as well. As an example, this is depicted for Dy(III) and PVBA 5 200 in Figure 27. The intrinsic PVBA fluorescence is quenched upon addition of Dy(III) ions. The excitation energy is transferred to the complexed Dy(III) ions, which thereupon show luminescence. In the shown spectral region, Dy(III) has two transitions from $^4F_{9/2} \rightarrow {}^6H_{15/2}$ and $^4F_{9/2} \rightarrow {}^6H_{13/2}$. The intrinsic PVBA fluorescence overlaps with the luminescence resulting from the higher energy transmission in Dy(III). For further evaluation the luminescence intensity arising from the $^4F_{9/2} \rightarrow {}^6H_{13/2}$ transition was used.

The dependence of the luminescence sensitization on the Ln(III) ion concentration was similar for the different Ln(III) ions used in this study as shown in Figure 28. Up to a concentration of 11 µmol·L^{-1} the luminescence intensity increases and at higher concentrations the luminescence intensity stays constant (in case of Dy(III)) or slightly decreases (Eu(III) and Sm(III)).

The measurements shown in Figure 28 were needed to define the Ln(III) ion concentrations for the measurements making use of the ILET to evaluate distances of coordinated Ln(III) ions. To find a compromise between sufficient luminescence intensity and metal loading, which allows the coordination of further Ln(III) ions (e.g., acting a acceptor) 5 µmol·L^{-1} was chosen. The highest total Ln(III) ions concentration was 20 µmol·L^{-1}.

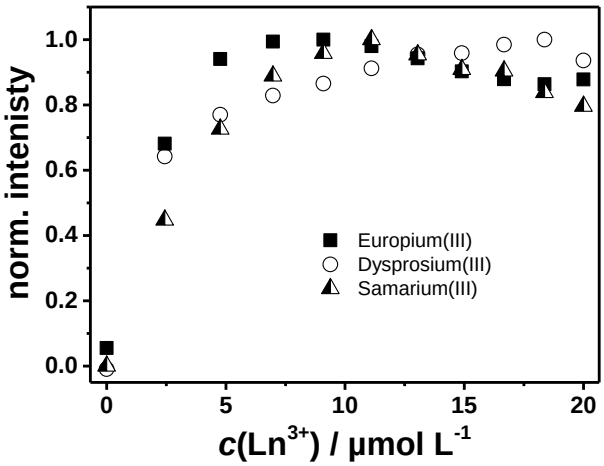

Figure 28: Normalized luminescence intensity of Ln(III) added to a solution containing 50 mg·L^{-1} upon excitation at λ_{ex} = 288 nm (sensitized excitation conditions). The intensities are normalized to their specific maximum intensity. The intensities of the $^5D_0 \rightarrow {}^7F_1$ (Eu(III)), $^4F_{9/2} \rightarrow {}^6H_{13/2}$ (Dy(III) and $^4G_{5/2} \rightarrow {}^6H_{7/2}$ (Sm(III)), respectively, transition were evaluated. Ionic strength of the solutions was 0.1 mol·L^{-1} NaCl.

In Figure 29 the effect of the addition of La(III) ions to solutions containing PVBA 5 200 and Eu(III) on the luminescence asymmetry ratio *r* – calculated according to eq. (2) – is compared for different ionic strengths (NaCl: 0.1 mol·L^{-1}, 1.0 mol·L^{-1} and 3 mol·L^{-1}). For the lowest concentration of background electrolyte, no effect on *r* can be concluded. Obviously, the coordinated Eu(III) is not affected by the addition of further metal ions. For the higher ionic strengths, the values of the asymmetry ratio scatter a little, but in principle, it remains constant. Comparable results (0.1 mol·L^{-1} and 1.0 mol·L^{-1} NaCl, respectively) were found for the higher molecular weight polymer PBVA 17 000.

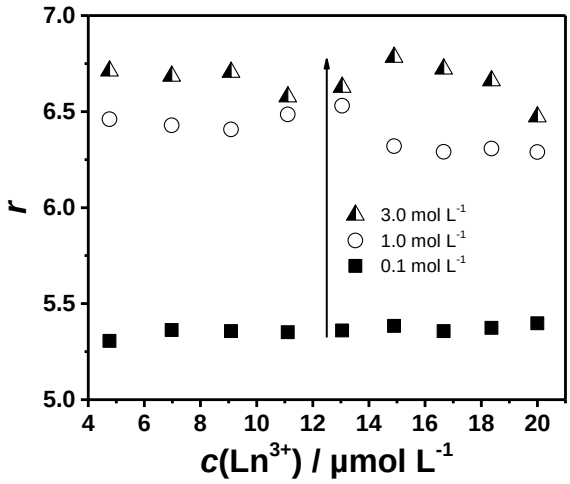

Figure 29: Asymmetry ratio *r* of the Eu(III) luminescence in complexes with PVBA 5 200 upon addition of La(III) ions. The Eu(III) concentration was 5 µmol·L^{-1}. Given is the total luminescence concentration. λ_{ex} = 288 nm, p*H* = 6.5.

If coordinated Eu(III) ions will be expelled from binding site due to competition, it will have no effect on the asymmetry ratio as only complexed Eu(III) ions can be excited via sensitization by the polymer. But to account for that, measurements with La(III) are indispensible, as they reflect influences only resulting from the increased Ln(III) ions concentration, which is shown in Figure 30. For the short-chain polymer PVBA 5 200 the Eu(III) luminescence intensity increases for ionic strength 1.0 mol·L^{-1} and 3.0 mol·L^{-1}, when La (III) ions are added. At lower ionic strength, an opposite trend was observable. For the long-chain polymer PVBA 17 000, the general dependency of the Eu(III) luminescence intensity upon addition of La(III) was the same for an ionic strength of 0.1 mol·L^{-1} and 1.0 mol·L^{-1}, respectively. The addition of Nd(III) quenches the Eu(III) luminescence intensity as a result of the aforementioned ILET. The luminescence intensities plotted in Figure 30 can be used, to calculate the energy transfer efficiency according to eq. (8) with I_{DA} as the luminescence intensity in presence of Nd(III) and I_D as the corresponding luminescence intensity in presence of La(III).

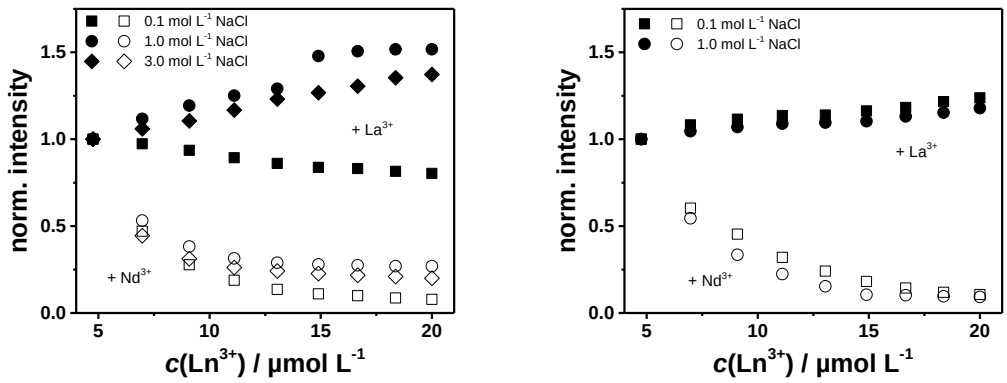

Figure 30: Change of Eu(III) intensity upon addition of La(III) and Nd(III), respectively. To a PVBA 5 200 (left) or a PVBA 17 000 (right) solution containing 5 µmol·L^{-1} of Eu(III). The concentration of the polymer was 50 mg·L^{-1} and p*H* = 6.5.

Besides Eu(III) also Dy(III) and Sm(III) were used as donors. In these experiments Nd(III) was used as an acceptor. For all chosen donor-acceptor-pairs a luminescence quenching of the

donor was found. The measurements were carried out for PVBA 5 200 and PVBA 17 000 as polymers in 0.1 mol·L^{-1} NaCl solution. For the measurements with Eu(III) as donor, the I_D values results from titration with La(III) ions as shown in Figure 30. For measurements with Sm(III) or Dy(III) as donor, the I_D values were taken from their resulting luminescence intensity upon their increasing concentration.

Figure 31 gives the energy transfer efficiencies calculated according to eq. (8) for relevant donor-acceptor-pairs are shown. The highest transfer efficiencies from the above mentioned experiments can be found for Eu(III) as donor. Dy(III) shows smaller and Sm(III) the smallest η values. Eq. (7) tells, that the energy transfer efficiency depends on the distance between the involved donor and acceptor ion as well as on the Förster distance R_0. The distances of the complexed Ln(III) ions should be very similar independent from the donor ion. Therefore, the differences in energy transfer efficiency have to result from different Förster radii. This is the key issue of this analysis. If no Förster distances are available from literature, they have to be calculated for each donor-acceptor-pair from photophysical parameters

$$\boldsymbol{R_0} = \sqrt[6]{\frac{\mathbf{9\ln(10)\kappa^2\Phi_D J}}{\mathbf{128\pi^5 N_A n^4}}}. \qquad (22)$$

Necessary parameters are the luminescence quantum yield Φ_D, the overlap integral of donor emission and acceptor absorption J, refractive index n and the orientation factor κ^2. Whereas J can be derived from absorption and stationary luminescence measurements, the determination of Φ_D is crucial.

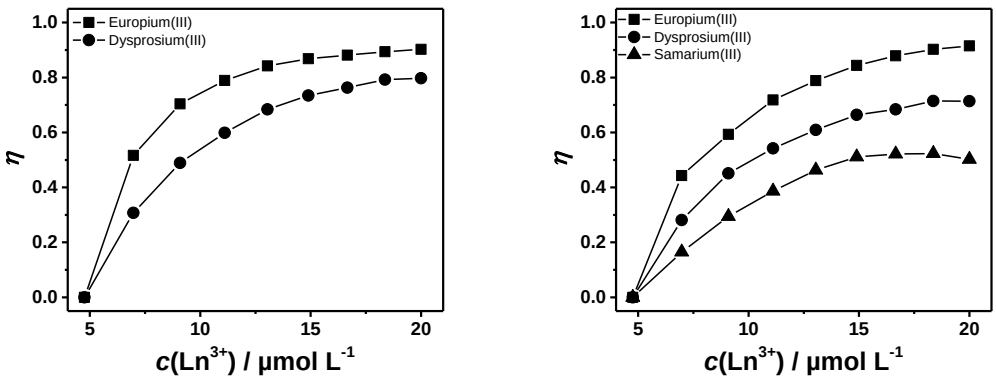

Figure 31: Energy transfer efficiencies η calculated according eq. (8) from stationary luminescence measurements for Ln(III)ions complexed to PVBA 5 200 (left) and PVBA 17 000 (right), respectively. The ionic strength was set to 0.1 mol·L^{-1} using NaCl. *c*(polymer) = 50 mg·L^{-1}, p*H* = 6.5. Details of the calculation are given in the text.

Dependent on how exact the energy transfer efficiency can be determined, a distance interval from $0.6 \cdot R_0 < R < 1.6 \cdot R_0$ corresponding to $0.95 < \eta < 0.05$ is accessible. By choosing a donor-acceptor-pair determinations of distances within a specific distance interval (governed by R_0) becomes possible.

So far, only results from stationary luminescence measurements were shown. The investigations dealing with the ILET were also performed by time-resolved measurements. Hereby, a

second photophysical parameter – the luminescence decay time – is at hand, which is sensitive to energy transfer processes. In these experiments Eu(III) was mainly used as donor as changes in its luminescence decay time are easier to measure with a required accuracy compared to Dy(III) or Sm(III).

For both, the short-chain and the long-chain polymer, the addition of La(III) ions results in an increase of Eu(III) luminescence decay time. Upon addition of Nd(III) ions the luminescence decay time of Eu(III) decreases. In Figure 32 (a) – (c) the luminescence decays of Eu(III) in complexes with PVBA are shown. Figure 32 (d) summarizes the derived luminescence decay times of Eu(III). The luminescence decays were fitted to a stretched exponential equation to account for the restricted dimension of the energy transfer.[33]

$$\boldsymbol{I = I_0 + A_1 \exp\left(-\frac{t}{\tau} - C\left(\frac{t}{\tau}\right)^{\gamma}\right) + A_2 \exp\left(-\frac{t}{\tau}\right)} \qquad (23)$$

In this equation, *I* is the measured luminescence intensity and τ the decay time of the donor (Eu(III)). *T*he time after laser flash is given by *t*. Background intensity resulting from noise of the detection system is reflected by I_0. The parameter *C* is proportional to the acceptor concentration and γ accounts for the local geometry. The third term was included to account for donor ions, which were not quenched by an acceptor. During the fitting procedure of the decays given in Figure 32 (a) – (c) comparable γ value arised (cf. Table 7). Independent of the

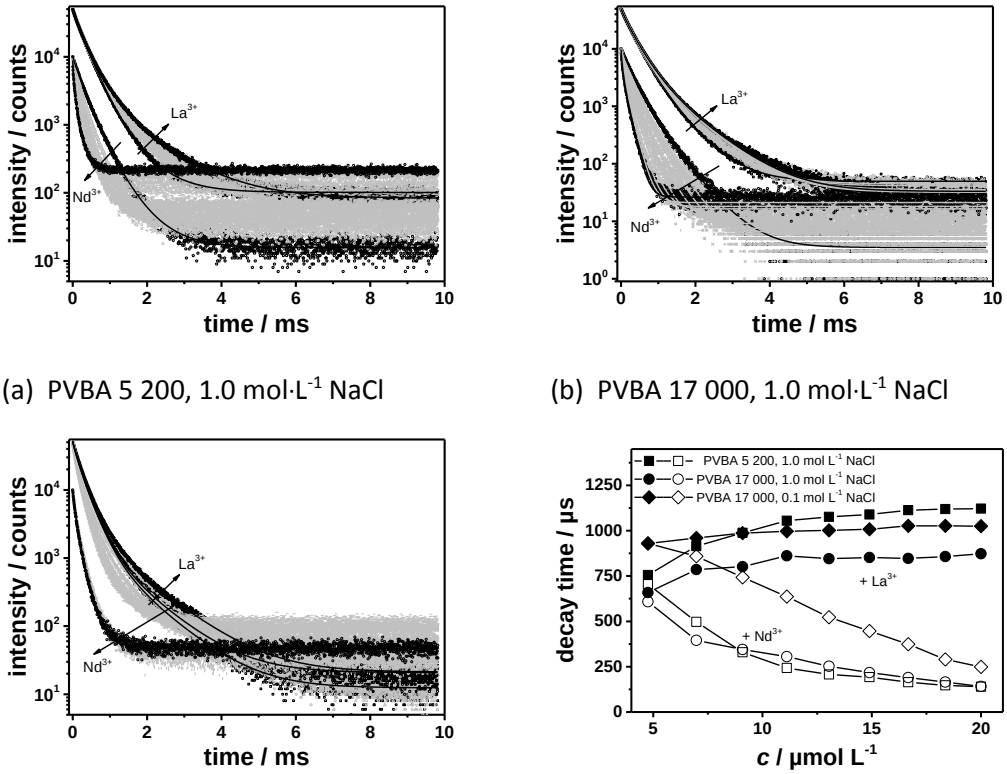

(a) PVBA 5 200, 1.0 mol·L^{-1} NaCl

(b) PVBA 17 000, 1.0 mol·L^{-1} NaCl

(c) PVBA 17 000, 0.1 mol·L^{-1} NaCl

(d) Decay times.

Figure 32: Luminescence decay kinetics and luminescence decay time of Eu(III) luminescence complexed to PVBA in presence of La(II) and Nd(III), respectively. *c*(Polymer) = 50 mg·L^{-1}, p*H* = 6.5, λ_{ex} = 288 nm, λ_{em} = 615 nm.

molecular weight of the polymer and the ionic strength, the measure of the local geometry γ is comparable.

Table 7: Measure of local geometry parameter γ resulting from the fitting of the decay curves given in Figure 32 (a) – (c) to eq. (23).

c(NaCl) / mol·L^{-1}	PVBA 5 200	PVBA 17 000
0.1	—	0.85
1.0	0.83	0.88

By comparing Figure 32 (d) with Figure 30 the same trend can be concluded. For the short-chain polymer PVBA 5 200 and an ionic strength of 1.0 mol·L^{-1} NaCl, for the luminescence decay time as well as for the luminescence intensity of Eu(III) a pronounced increase by increasing La(III) concentration can be found. An increase of Eu(III)'s luminescence intensity and luminescence decay time, respectively, can also be found for the long-chain polymer PVBA 17 000 at ionic strength of 0.1 mol·L^{-1} or 1.0 mol·L^{-1} NaCl, but only to a lesser extent. The effect to the Eu(III) complexed to the lower molecular weight polymer is stronger.

Up to now, for the donor-acceptor pairs the results of stationary and time-resolved experiments were presented. In all cases a quenching of the donor luminescence either decay time or intensity, when increasing the acceptor concentration was found. For the donor-acceptor-pair Eu(III)-Nd(III) is a Förster distance known from literature.[7] The first step is to calculate the energy transfer efficiency η from the luminescence intensities plotted in Figure 30 or the luminescence decay time given in Figure 32. With eq. (7) and a Förster distance of R_0 = 8.53 Å from literature distances between the Ln(III) ions complexed to the polymer were derived.

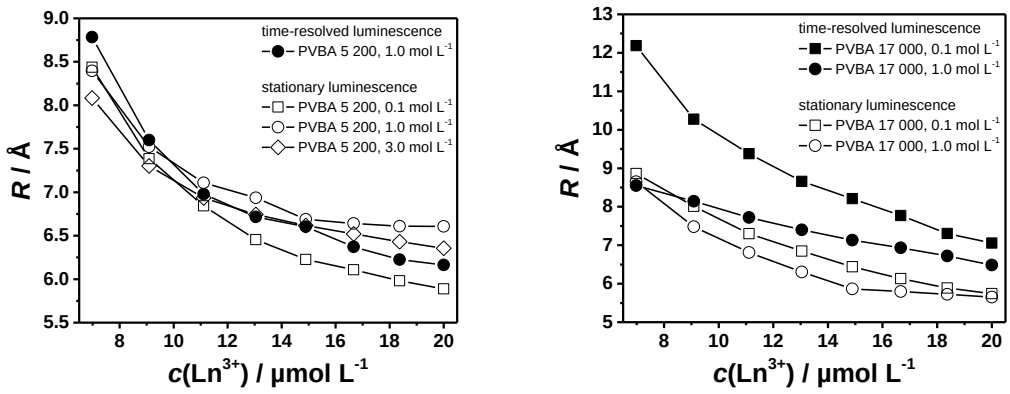

Figure 33: Derived distances *R* between Ln(III) ions coordinated by the short-chain polymer (left) and the long-chain polymer (right), respectively (c(Polymer) = 50 mg·L^{-1}, p*H* = 6.5).

In Figure 33 for both polymers (PVBA 5 200 and PVBA 17 000) distances *R* between coordinated Ln(III) ions are plotted. For the short-chain polymer (PVBA 5 200) no clear trend can be concluded. Independent on the ionic strength the distances decrease from (8.4 ± 0.3) Å down to (6.3 ± 0.3) Å. For PVBA 17 000, stationary and time-resolved luminescence measurements give different results. Whereas from stationary measurements, almost no effect from the ionic strength can be found, the time-resolved measurements show an effect of the ionic strength.

Here, the distances decreases by increasing ionic strength. This can be explained, if the polymer is understood as a polyelectrolyte. An increase in ionic strength lead to a charge compensation along the polymer chain, what subsequently alters the confirmation of the polymer. A possible alteration can be the folding of the polymer, which is connected to a reduction in size and hence decrease of distances between coordinated Ln(III) ions.

3.6 Vibrational spectroscopy on mineral surfaces

Kaolin and intercalation of LMWC

Before the vibrational spectra of intercalation compounds can be discussed, the vibrational spectra of the source clays Kaolin KGa-1b and Kaolin KGa-2 have to be analysed. In this study Raman microscopy and SFG spectroscopy were combined to obtain complementary information for a chemical speciation at mineral interfaces.

From each Kaolin sample Raman spectra at three different points of the sample were measured. The spectra were background corrected. Averaging of the three spectra gave a mean Raman spectrum. The averaged Raman spectra for KGa-1b and KGa-2 are depicted in Figure 34.

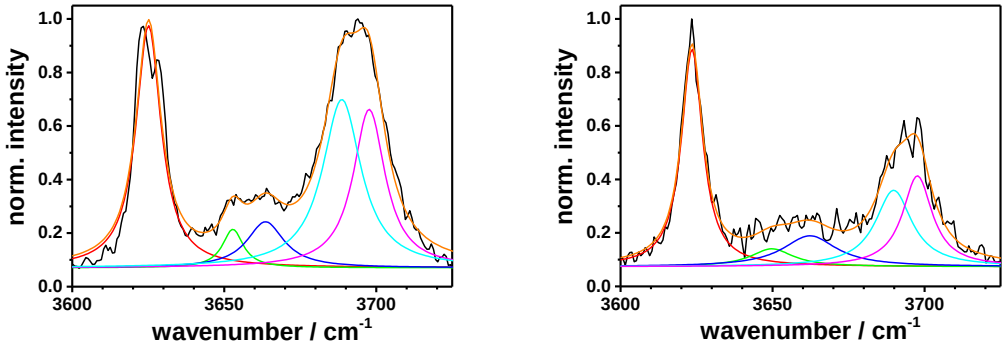

Figure 34: Averaged Raman spectra (black) of Kaolin KGa-1b (left) and KGa-2 (right). To each underlying vibration a Lorentzian function was fitted. Five vibration could be resolved: ν_1 (red), ν_2 (green), ν_3 (blue), ν_4 (cyan) and ν_5 (magenta). The sum of all single Lorentzian functions gives the cumulated fit (orange).

For both Kaolin samples five peaks could be observed. Fitting of the data to Lorentzian functions gave the peak positions and areas of the single vibrational transitions. The results are summarized in Table 8. For both samples the vibrational frequencies are slightly different, but an assignment to expected OH vibrations in kaolinite was possible.[34,35] The inner hydroxyl group originates the vibration around 3625 cm^{-1}. The inner surface hydroxyl groups have vibrations around 3650 cm^{-1}, 3665 cm^{-1}, 3689 cm^{-1} and 3698 cm^{-1}. The values found are in good agreement with the values reported by Frost et al.[34] The fitting of the peaks around 3650 cm^{-1} and 3665 cm^{-1}, especially for KGa-2, was challenging as the intensities of these vibrational transitions are rather low.

Table 8: Results of fitting the Raman spectra of both Kaolin samples to a sum of Lorentzian functions. Given are the peak positions and the relative peak areas (rel. area).

Vibration	KGa-1b		KGa-2	
	Peak position / cm^{-1}	rel. area / %	Peak position / cm^{-1}	rel. area / %
ν_1	3625 ± 1	30.1 ± 0.6	3623 ± 1	35.5 ± 0.8
ν_2	3653 ± 1	4.0 ± 1.7	3650 ± 3	11.7 ± 5.4
ν_3	3664 ± 1	8.5 ± 2.8	3666 ± 3	10.3 ± 5.9
ν_4	3689 ± 1	32.3 ± 5.8	3689 ± 1	14.9 ± 4.8
ν_5	3698 ± 1	25.2 ± 7.1	3697 ± 1	27.6 ± 4.3

The next step was to use SFG spectroscopy to monitor the OH vibration region of the same kaolinite samples. Following eq. (15) the intensity of a SFG signal depends as well on the probability for a Raman as for an IR transition. Additionally, SFG spectra stems from interfaces in the material, whereas Raman spectroscopy gives signals from a bulk phase. Therefore, some differences between Raman and SFG spectra are to be expected.

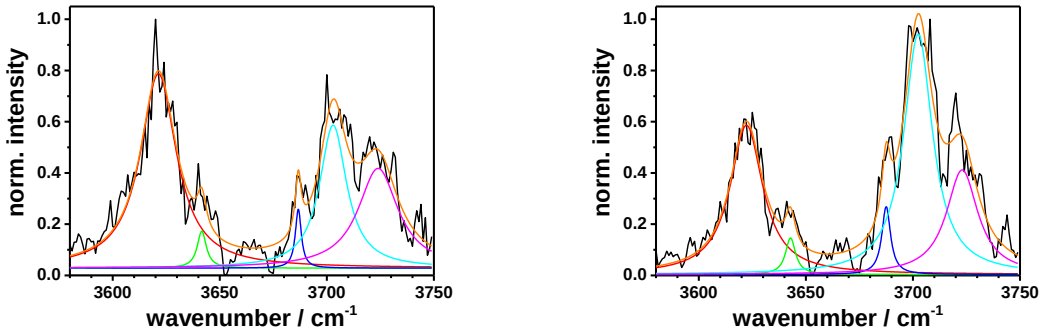

Figure 35: SFG spectra of Kaolin KGa-1b (left) and KGa-2 (right) corrected for intensity of vis (I_{vis}) and IR (I_{IR}) laser beam. The measured spectrum (black) was fitted to a sum of Lorentzian functions. As fitting result, the peak position and peak area of the vibrational transitions could be obtained. In the fitting five vibrational transitions were assumed, giving vibrations ν_1 (red), ν_4 (blue) and ν_5 (cyan). Deviating from the Raman spectra shown in Figure 35, vibrations at ν_x (magenta) and ν_z (green) were found.

Comparable to the Raman spectra, also the SFG spectra (cf. Figure 35) show two strong peaks, one around 3620 cm^{-1} and the other one around 3700 cm^{-1}. These transitions can be assigned to the ν_1 and ν_5 transition, respectively. The exact values of the vibration frequencies, given by the peak positions resulting from fitting with a sum of Lorentzian functions, are listed in Table 9. In both kaolinites KGa-1b and KGa-2, the transitions ν_1 and ν_5 are slightly shifted < 5 cm^{-1} in the SFG compared to Raman spectra. Also at a frequency around 3688 cm^{-1} a transition, denoted with ν_4, was present, which is almost not shifted compared to the Raman spectra. At 3642 cm^{-1} a vibrational transition shows up, but its origin is not that clear. Possibly, this signal could be i) the vibration ν_2 shifted about 10 cm^{-1} or ii) a signal arising from surface adsorbed water, condensed from air.

The intensity of SFG signals is direct proportional to the intensity of the IR light reaching the sample. The shown SFG spectra are corrected for both, I_{vis} and I_{IR}. For technical reasons, the intensity of the laser beams are measured in a given distance from the sample surface, what

is no problem for the visible light as it does not interact with the air. In contrast, the IR light, needed to probe the range of OH vibrations, can be absorbed by present water vapor. This makes a correction for the intensity of the IR light challenging. Here, the SFG setup has to be improved. Therefore, the apparent transition at 3642 cm^{-1} could be an artefact, resulting from a dip in the higher energetic edge of the ν_1 transition due to an absorption of the corresponding IR light by ambient water vapor.

In the SFG spectra also a transition around 3665 cm^{-1} can be observed, but it was not possible to include it in the fitting procedure. This weak transition can be related to the vibration ν_3 known from Raman spectra. In the SFG spectra an additional peak around 3723 cm^{-1} could be observed. The origin of this vibration is yet not clear. A quantitative analysis of SFG spectra is difficult, because of the aforementioned uncertainties in the determination of the actual IR intensity reaching the sample. The weak intensity of the vibration ν_4 is clear by comparing IR and Raman spectra. In IR spectra of kaolinites the transition at 3688 cm^{-1} is only weak.[36] As the probability of a SFG process is directly proportional to the IR transition momentum, also the intensity of this transition in a SFG spectrum is expected to be low.

Table 9: Results of fitting the SFG spectra of both Kaolin samples to a sum of Lorentzian functions. Given are the peak positions and the relative peak areas (rel. area).

Vibration	KGa-1b		KGa-2	
	Peak position / cm^{-1}	rel. area / %	Peak position / cm^{-1}	rel. area / %
ν_1	3621 ± 1	45.1 ± 3.2	3622 ± 1	30.4 ± 2.7
ν_z	3642 ± 1	2.2 ± 1.0	3643 ± 1	2.3 ± 1.0
ν_4	3687 ± 1	2.3 ± 0.9	3688 ± 1	3.7 ± 1.3
ν_5	3703 ± 1	24.9 ± 3.6	3702 ± 1	43.1 ± 3.8
ν_x	3724 ± 1	25.6 ± 4.4	3723 ± 1	20.6 ± 3.4

Under some conditions, small organic material can intercalate into kaolinite lattice layers. The intercalation happens at the inner surface hydroxyl groups, which affects the vibrational spectrum.[37,38] Additionally, also the distance between layers in the kaolinite structure will increase upon intercalation.[37]

In Figure 36 the Raman spectra received at three different points of an intercalated Kaolin KGa-1b sample are plotted. For the intercalation potassium acetate was used. As can be seen, the spectra are different. Using the spatial resolution of the Raman microscope, a chemical imaging of the clay surfaces becomes possible. From the three spectra plotted in Figure 36 differences in the intercalation at the probed spots of the sample can be extracted.

The Raman spectrum plotted in green reflects the highest degree of intercalation. Due to the intercalation an additional band at ν_{Ac} = 3607 cm^{-1} in the Raman spectrum can be observed. This band arises from the interactions of the inner surface hydroxyl groups with acetate. During intercalation hydrogen bonds between layers of the kaolinite were broken and new hydrogen bonds to the acetate were formed.[37] As only the inner surface hydroxyl groups are affected by this interaction, the vibration frequency ν_1 of the inner hydroxyl group remained

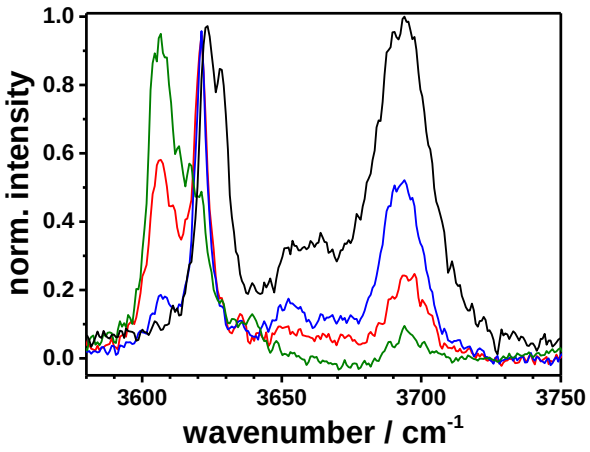

Figure 36: Raman microscopy spectra of three different spots (blue, red and green) of an intercalated KGa-1b sample. For comparison, also the Raman spectrum of an untreated KGa-1b sample (black) is plotted.

unchanged. From Figure 36 it is obvious, that with increasing intensity of ν_{Ac} the intensities of ν_2 to ν_5 decreased. For a complete intercalation, the intensities of these vibrations can become zero.[38]

The intercalation could also be shown with SFG spectroscopy. In Figure 37 a SFG spectrum of an intercalation formed between KGa-1b and potassium acetate is shown. The intensity of the vibrational transition at 3620 cm^{-1} is reduced compared to the SFG spectrum received for a pure KGa-1b sample (plotted in gray). Nonetheless, in the intercalated sample a transition around 3606 cm^{-1} can be seen. Compared to the pure KGa-1b samples, the intensity of the ν_3 vibration as well as the vibrations around 3700 cm^{-1} were almost not changed, which is a clear difference to the Raman measurements. After intercalation of potassium acetate a decrease in the intensities of these vibrations is expected. Contrary to Raman measurements, for the formation of a SFG signal, the probability for an IR transition plays a role, too. When water is adsorbed at the surface of the Kaolinite, this will influence the SFG signal, as the water itself has a strong IR absorption. Hence, the unchanged SFG signal at wavenumbers above 3650 cm^{-1} may be a result of adsorbed water.

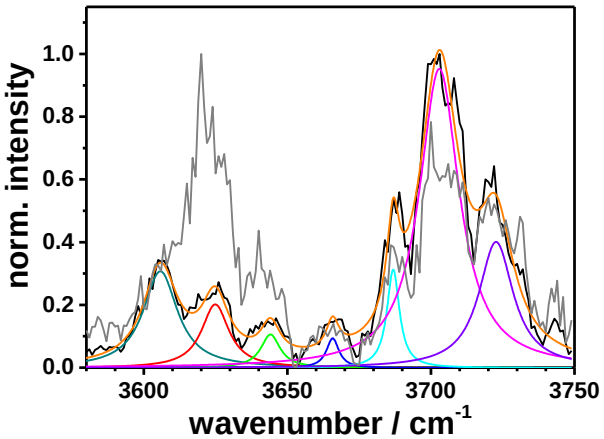

Figure 37: SFG spectra (black) of an intercalation complex of KGa-1b and potassium acetate. In addition to the vibrational bands ν_1 (red), ν_z (green), ν_5 (magenta) and ν_x (violet) fitting to a sum of Lorentzian functions gave ν_3 (blue) and ν_{Ac} (dark cyan). For comparison, the SFG spectrum of the pure KGa-1b (gray) is plotted.

A complementary approach to study the intercalation is the use of X-ray powder diffraction (XRD) measurements. An intercalation changes the distances of the lattice layers of the Kaolinite, which subsequently alters the positions of the reflexes in an XRD spectrum.

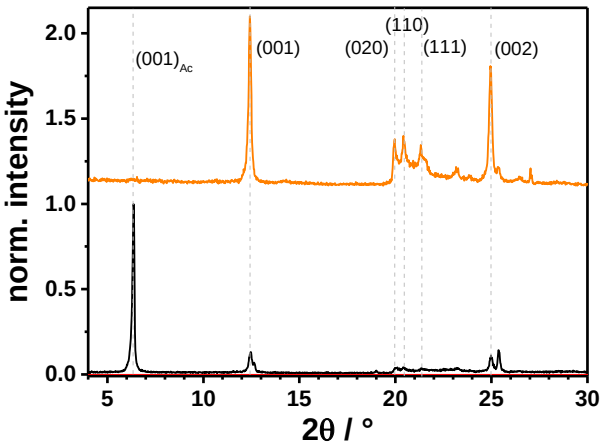

Figure 38: XRD spectra of potassium acetate intercalated KGa-1b (black) and pure KGa-1b (orange). For clarity, the XRD of the pure Kaolinite was shifted about one unity to higher intensities. The assignment of the reflexes to the lattice planes followed data from literature.[39]

In the pure Kaolinite KGa-1b, the reflex of the (001) plane is at 2θ = 12.4 °, shown in Figure 38. Applying the Bragg equation[h] and a wavelength of the copper anode of λ_{Cu} = 1.5405 Å gives a distance of 7.13 Å, which is very near to a literature known value of 7.14 Å.[3] The (001) basal reflex shifts to a lower value (2θ = 6.4 °) upon intercalation (cf. Figure 38). This translates in a distance of 13.8 Å, which is a little bit shorter than reported values.[40] Intercalation happens within the kaolinite layers, which changes the position of the reflexes originated by (00*l*) planes. The lattice in *a* and *b* direction are not influenced by intercalation. In the XRD spectrum of the intercalated KGa-1b sample the reflex from the (001) plane of the non-intercalated KGa-1b can be observed. This shows that no completed intercalation occurred.

To figure out, how fast potassium acetate intercalates into kaolinite, the contact time of the potassium acetate solution and the kaolinite was varied. As parameter for the evaluation the degree of intercalation d*I* was chosen, which can be calculated by the relative appearance of the reflex originating from intercalated $I_{(001),\ \text{intercalated}}$ and non-intercalated $I_{(001),\ \text{non-intercalated}}$ kaolinite, respectively.[3]

$$\mathrm{d}I = \frac{I_{(001),\ \text{non-intercalated}}}{I_{(001),\ \text{non-intercalated}} + I_{(001),\ \text{intercalated}}} \qquad (24)$$

[h] $2d_{hkl}\sin\theta = n\lambda$

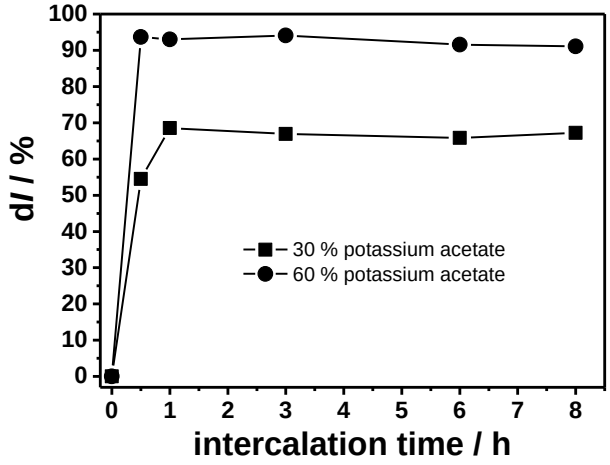

Figure 39: Degree of intercalation after certain impact times between potassium acetate and Kaolin KGa-1b. For analyzing the time dependence, a 60 weight percent (bullets) and a 30 weight percent (squares) potassium acetate solution was used.

In Figure 39 the degrees of intercalation for impact time between 30 minutes and 8 hours are compared. It turned out, that the degree of intercalation was almost independent of the contact time. Only for the 30 weight percent potassium acetate solution, an increase from d*I* = 55 % to d*I* = (67 ± 1) % was found. For the potassium acetate solution the degree of intercalation is (93 ± 2) % independent on contact time. Due to the sample preparation, contact times smaller than half an hour were hardly accessible as after stirring, the suspensions were centrifuged for 30 minutes. During the centrifugation process, ongoing intercalation might be possible. In additional experiments with 30 weight percent potassium acetate solutions and shorter contact times, with 10 minutes (20 minutes) of stirring and subsequently, 30 minutes centrifugation a d*I* of around 42 % (41 %) was found. That there is no difference in d*I* for both contact times, supported the mentioned imitation in time resolution. Above contact times of 40 minutes d*I* approaches a plateau. Obviously, the formation of the intercalation compound reaches an equilibrium.

Besides XRD also Raman microscopy and SFG spectroscopy were used to evaluate the time dependence of the intercalation process. The attempt was made to derive degrees of intercalation d*I* also from Raman and SFG measurements. In analogy to the XRD measurements (eq. (24)) also from vibrational spectroscopy a discrimination between intercalated and pure kaolinite is possible. As discussed earlier, the vibrations ν_2, ν_3, ν_4 and ν_5 can be assigned to the pure kaolinite, whereas ν_{Ac} reflects a vibration of the intercalated KGa-1b. The degree of intercalation d*I* can be calculated with

$$\mathrm{d}I = \frac{I(\upsilon_{Ac})}{I(\upsilon_{Ac})+I(\upsilon_2)+I(\upsilon_3)+I(\upsilon_4)+I(\upsilon_5)}, \qquad (25)$$

where $I(\nu_i)$ is the intensity of the *i*th vibration. As can be seen in Figure 40 (left) for an impact time of 50 minutes between potassium acetate solution and kaolinite KGa-1b, Raman microscopy gives for certain sample spots different vibrational spectra. The high spatial resolution is an advantage for chemical imaging, but is an obstacle for comparing d*I* values deduced from

XRD with them derived from Raman microscopy measurements. XRD reflects bulk information and Raman microscopy information from a very specific point at the sample surface. Therefore, Raman spectra were recorded at five different positions of the sample and the degree of intercalation was calculated from every measurement. Finally, from all five d*I* values a mean value and a standard deviation were computed. This approach was applied for all samples with different impact times. The results are plotted in Figure 40 (right). The values for d*I* are smaller than for the degree of intercalation calculated from XRD measurements (cf. Figure 39). Possibly, the differences originate from the measuring arrangement. It is known, that the crystallinity of kaolinite decreases upon intercalation.[3] For Raman microscopy, the scattered light is measured in reflection. The lower the crystallinity the higher the amount of diffuse reflection. Light, which is diffusely scattered from the surface will not be collected from the objective and will not contribute to the measured Raman spectrum. Therefore, in the Raman spectrum scattered light originating from crystalline regions will predominate. But, this might be regions, in which intercalation will take place to a lesser extent.

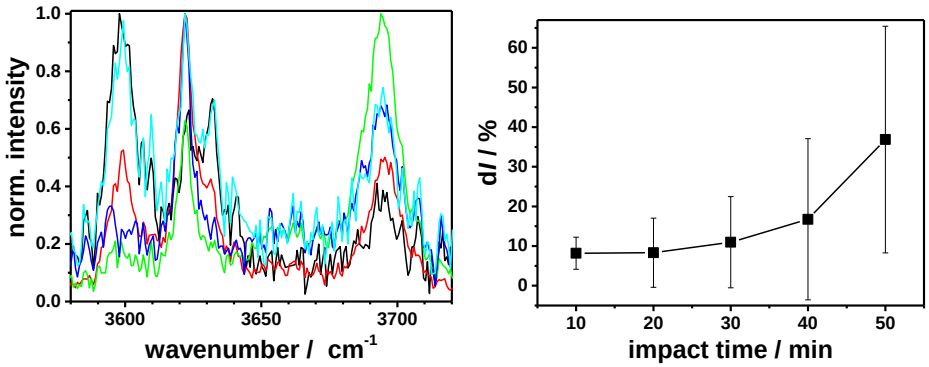

Figure 40: (left) Raman spectra of a sample with an impact time for intercalation of 50 minutes taken at different positions of the sample. (right) Degree of intercalation d*I* calculated from Raman measurements.

A direct intercalation of longer-chain molecule is not possible. A way out, is an indirect intercalation.[41,42] Here, an already intercalated kaolinite is necessary. During the indirect intercalation the guest molecule is expelled and replaced by the longer-chain molecule. A possible precursor for an indirect intercalation is a DMSO kaolinite intercalation complex.

An intercalation of KGa-1b with potassium hexanoate was studied as well. A DMSO KGa-1b intercalation compound was used as precursor. In Figure 41 and Table 10 the vibrational spectra and vibrational frequencies for both, Raman and SFG, of this compound are shown. In both spectra, the main OH vibration expected for kaolinite samples can be observed. The peak position of certain vibrations differ slightly in SFG and Raman spectra. For comparison, also the vibrational spectrum of the pure KGa-1b is plotted in Figure 41. In the SFG spectrum a pronounced vibration at ν_{DMSO} = 3667 cm^{-1} can be observed, which is also observable in the Raman spectrum at ν_{DMSO} = 3664 cm^{-1}. These vibration can be assigned in accordance with literature to the vibration of the intercalated DMSO.[43] In the Raman spectrum, the assignment is not as straightforward as ν_{DMSO} overlaps with the ν_3 vibration of the pure kaolinite, which is only weak present in the SFG spectrum. In accordance with the published Raman spectra, the intensity of the vibration ν_4 and ν_5 also decreases upon intercalation of DMSO.[43]

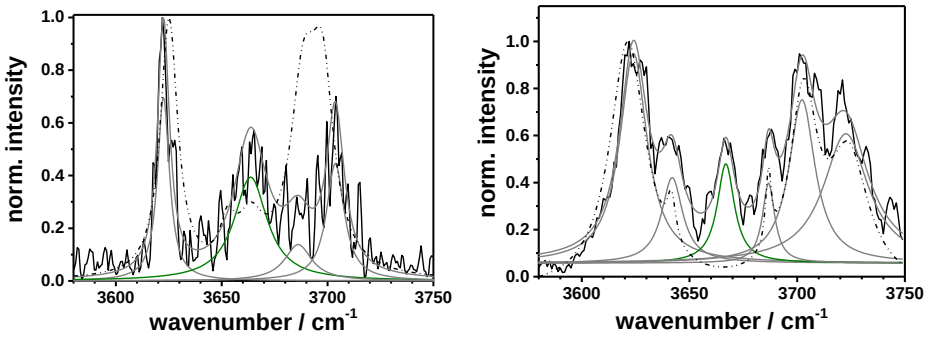

Figure 41: Vibrational spectra of the DMSO KGa-1b intercalation compound. The vibrational spectrum of pure KGa-1b is plotted with a dashed-dotted line. Due to intercalation a vibration (dark green) around 3664 cm^{-1} (Raman, left) and 3667 cm^{-1} (SFG, right) arising from the intercalated DMSO was detectable. To the measure data a sum of Lorentzian functions was fitted. The single Lorentzian as well as their sum are plotted with gray lines.

The intercalation could also be monitored by XRD measurements (cf. Figure 42). Here, the reflex from the (001) plane shifts to $2\theta = 8.0$ °, which corresponds to a layer distance of 11.04 Å – a value consistent with a published value of 11.21 Å.[42]

Table 10: Peak positions and relative peak intensities (rel. intensity) of the DMSO KGa-1b intercalation compound. The peak maxima and relative intensities were derived by fitting the measured data to a sum of Lorentzian functions.

	Raman		SFG	
	peak position / cm^{-1}	rel. Intensity / %	peak position / cm^{-1}	rel. intensity / %
ν_1	3622 ± 1	25.2 ± 2.0	3624 ± 1	28.3 ± 1.7
ν_2	—	—	3642 ± 1	8.8 ± 1.5
ν_{DMSO}	3664 ± 1	39.5 ± 6.2	3667 ± 1	8.4 ± 0.9
ν_4	3686 ± 3	11.3 ± 7.8	3687 ± 1	4.9 ± 1.1
ν_5	3704 ± 1	24.0 ± 4.2	3702 ± 1	21.0 ± 2.9
ν_X	—	—	3723 ± 1	28.6 ± 3.2

With the DMSO intercalated kaolinite precursor compound an indirect intercalation should be possible. In Figure 42 the XRD spectrum of the potassium hexanoate intercalated KGa-1b kaolinite and for comparison also the XRD spectrum of pure and DMSO intercalated KGa-1b are shown. The indirect intercalation results in the formation of the (001) reflex at $2\theta = 4.8$ °, which correlates with a layer distance of 18.4 Å. But, also the intensity of the reflex at $2\theta = 12.4$ ° increases. Obviously, a de-intercalation competes with the desired indirect intercalation. The reflex at 12.4 ° not only increases in intensity, but also is broadened to smaller reflection angles. This behavior is known from de-intercalation, when some layers do not shrink to their original distance.[44] As can be seen from Figure 42, the intensity of reflexes originated from de-intercalated KGa-1b are higher than the reflex from the potassium hexanoate intercalated KGa-1b, which indicates a low degree of intercalation. Applying eq. (24), the degree of intercalation is about $dI = 10$ %. The low degree of intercalation is also reflected by SFG and Raman measurements as the received spectra looks like the vibrational spectra of the pure Kaolin KGa-1b.

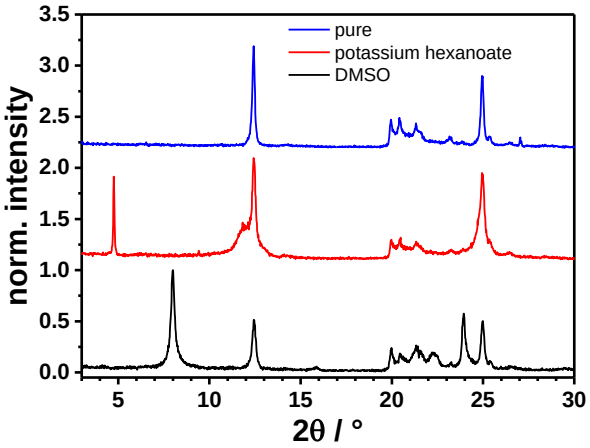

Figure 42: XRD spectra of the pure KGa-1b, DMSO intercalated and potassium hexanoate intercalated KGa-1b. For clarity, the XRD spectra are vertically shifted.

Lanthanide(III) complexes with LMWC

In addition to luminescence measurements also Raman spectroscopy was used to study the interaction between Ln(III) and LMWC. For these investigations glycolic acid was chosen. Because the luminescent Ln(III) ions interfered with the Raman measurements they were substituted by the (under the experimental conditions applied) non-luminescence Gadolinium(III) (Gd(III)). Due to the low Raman intensity, glycolic acid was used in a concentration of

Table 11: Complexation constants for Eu(III) LMWC complexes at an ionic strength of *I* = 0.1 mol·L^{-1}. Values are taken from literature.[22]

Ln(III):acid	lg *K*				
	formic acid	acetic acid	propionic acid[#]	glycolic acid	
1:1	1.44	2.13	2.23	2.93	2.54[##]
1:2	1.94	3.64	3.75	5.07	4.48[##]
1:3	–	4.24		6.52	5.85[##]

[#] *I* = 0.1

[##] *I* = 1, Ln(III) = Gd(III)

0.5 mol ·L^{-1} to receive a decent Raman signal. To achieve a considerable complexation (cf. Table 11) Gd(III) concentrations from 0.01 mol·L^{-1} to 1.0 mol·L^{-1} were chosen.

With the literature values for the complexation constants given in Table 11 a speciation calculation was carried out. The result of this calculation is shown in Figure 43 left. At p*H* = 5 and a Gd(III) concentration of 0.01 mol·L^{-1} most of the glycolic acid is in its deprotonated form and the Gd(III) is almost completely complexed as [Gd(glycolate)$_3$]. With higher the Gd(III) concentration the amount of 1:3 Gd(III) glycolate complexes decreases and a 1:1 complex is favorable at *c*(Gd(III) = 1 mol·L^{-1}. Under this experimental conditions almost no free glycolate is expected.

This shift in the equilibrium concentrations can be monitored by Raman spectroscopy. Corresponding Raman spectra are plotted in Figure 43 right. At low Gd(III) concentration a peak around 915 cm^{-1} can be observed. This peak can be assigned to the C-C vibration.[45] With in-

creasing Gd(III) concentration, a distinct shift of this vibration to higher wavenumbers is observed. Quantum mechanical calculations[i] showed, that the differences in the position of the C-C stretching vibration in the different Gd(III) glycolate complexes are relatively small and therefore hardly to resolve with Raman spectroscopy. The changes in the Raman spectrum are in good agreement with the speciation diagram.

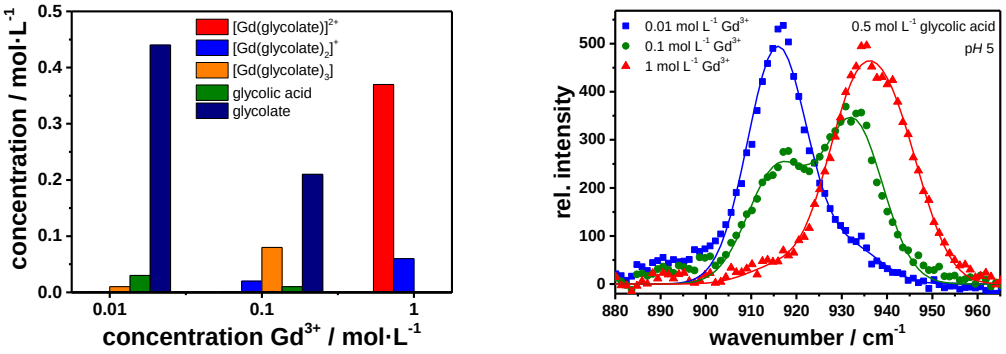

Figure 43: Left: Speciation diagram for the expected concentrations of the different Gd(III) glycolate complexes. The calculation of the speciation was done with the ChemEQL package[j] and based on the stability constants given in Table XX1.[23] Right: Raman spectra at different concentrations of Gd(III). *c*(glycolic acid) = 0.5 mol·L^{-1}, p*H* = 5.

[i] Calculations performed by Dr. Thomas Ritschel, now Gonotech GmbH. Calculations were carried out using Gaussian 09 program suite[48]. The geometries were fully optimized at the B3LYP level of theory using the polarized triple zeta split valence 6-311+G(d,p) basis set for the light atoms (C, O and H). For Gd(III) the MWB53 basis together with an effective core potential (ECP) for the inner shells (up to and including 4*f*) was utilized. The effect of the solvent was taken into account by the use of polarizable continuum model (PCM).

[j] An actual version of this software package can be found at http://www.eawag.ch/en/department/surf/projects/chemeql/.

3. 7 Europium(III) complexes with LMWC and Kaolinit

The interaction of Eu(III) with kaolinite Kaolin KGa-2 in the presence of different LMWC was investigated. LMWC used were formic, acetic, propionic, and glycolic acid, respectively. When taking a $4 \cdot 10^{-4}$ mol·L^{-1} Eu(III) solution with increasing concentration of LMWC at p*H* = 5 the luminescence decay time increases as can be seen in Figure 44 (left). Only at LMWC concentrations above 10^{-4} mol·L^{-1} a change of the luminescence decay time compared to Eu(III) in water can be noticed. This is due to the weak complexes, which are generally formed between Ln(III) and LMWC. In Table 11 the stability constants for Eu(III) (and Gd(III)) complexes with LMWC investigated are listed. By comparing the stability constants for the 1:1 complexes, the trend of the luminescence decay time upon increasing LMWC concentration can be understood.

Formic acid has the lowest stability constant and therefore forms the weakest complexes. By direct excitation of Eu(III) at λ_{ex} = 394 nm ($^5L_6 \leftarrow {}^7F_0$-transition), both, the complexed and the aqueous Eu(III) are excited and contribute to the observed luminescence. Therefore, the luminescence decay time is measured as a mean value of free and bound Eu(III). For acetic and propionic acid, the stability constants are nearly the same. A similar value for Eu(III) luminescence decay is found. The strongest complexes are formed with glycolic acid, which give raise to the highest luminescence decay time, reaching a value of τ = 218 µs ± 2 µs. The same conclusions can be drawn from the asymmetry ratios *r*, which are plotted in Figure 45. For the ligands investigated the complex formation will mainly occur via the carboxylic group. Therefore, a similar influence on the Eu(III) luminescence is expected.

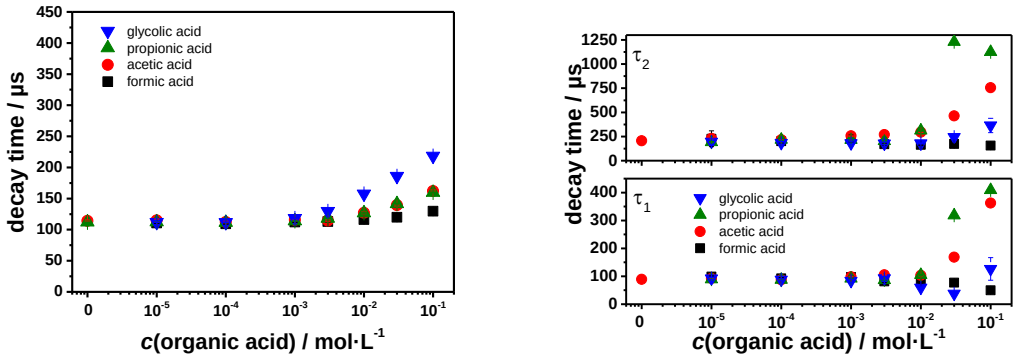

Figure 44: Decay time of Eu(III) derived from time-resolved measurements. Left: Resulting decay times of the Eu(III) in solutions with LMWC before mixing with Kaolin KGa-2, *c*(Eu(III)) = $4 \cdot 10^{-4}$ mol·L^{-1}, p*H* = 5, λ_{ex} = 394 nm. Right: Decay-times of Eu(III) in solutions with LMWC after sorption onto Kaolin KGa-2. Experimental details: p*H* = 5, background electrolyte 0.01 mol·L^{-1} $NaClO_4$.

For the dried Eu(III) LMWC complexes with Kaolin KGa-2 samples the kinetic of the Eu(III) luminescence was more complex compared to aqueous solutions (vide supra). The luminescence decays could be reasonably well fitted by a biexponential rate law and the extracted (operationally defined) luminescence decay times are shown in Figure 44 (right). Formic acid as well as glycolic acid has apparently no or only a minor impact on the luminescence decay times, whereas acetic and propionic acid have a distinct influence on the luminescence decay time.

A second parameter is the asymmetry ratio *r*. In Figure 45 left, the luminescence spectra for an adsorbed Eu(III) species after mixing of Kaolin KGa-2 and acetic acid at different concentrations is shown. At acetic acid concentration above 10^{-3} mol·L^{-1} the Eu(III) luminescence spectrum is altered and subsequently also the asymmetry ratio. These changes are a consequence of sorption of Eu(III) to the clay phase and are also observed for the other solids received from ternary solutions as can be seen in Figure 45. For all LMWC the asymmetry ratio increases from around r = 1.3 up to r = 5, depending on the LMWC. Comparable to the trends found with the binary mixtures, formic acid has the weakest effect on *r*. For the solids, separated from ternary mixture with one of the other three acids, respectively, the alteration of the asymmetry ratio with LMWC concentration is roughly the same.

Both, the multi-exponential luminescence decay as well as the changes in the asymmetry ratio point to a sorption of Eu(III) on the kaolinite. Due to adsorption the Eu(III) asymmetry ratio increases to about r = 1.3 compared to r = 0.6 for the Eu(III) aqueous species (cf. Figure 45 (right)). Also in the presence of LMWC Eu(III) is adsorbed to the mineral surface. Here, the asymmetry ratio points to adsorbed Eu(III) LMWC complexes. From both, luminescence decay times and asymmetry ratio, the adsorbed Eu(III) species in presence of acetic acid and propionic acid, respectively, is subjected to the strongest alteration.

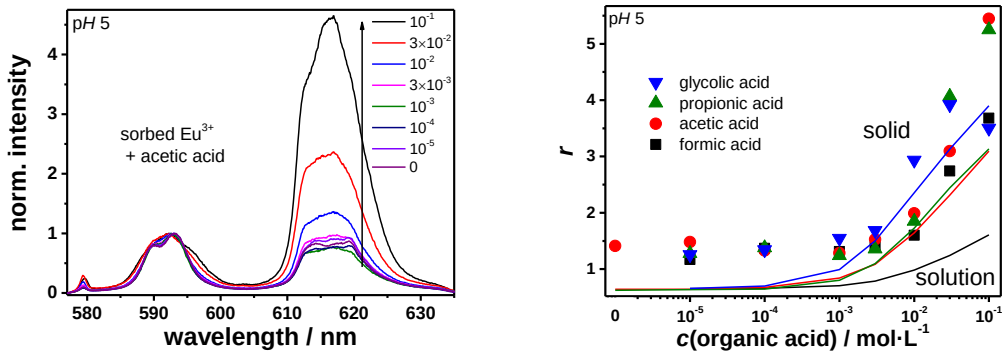

Figure 45: Left: Luminescence spectra of sorbed Eu(III) species after mixing with acetic acid at given concentration and Kaolin KGa-2. From these luminescence spectra the asymmetry ratio can be calculated from the intensities of the transitions around 592 nm ($^5D_0 \rightarrow {}^7F_1$) and around 615 nm ($^5D_0 \rightarrow {}^7F_2$) (cf. eq. (2)). Right: Asymmetry ratio *r* of the Eu(III) in presence of LMWC in solution (lines) and adsorbed to Kaolin KGa-2. *c*(Eu(III)) = $4 \cdot 10^{-4}$ mol·L^{-1}, p*H* = 5, λ_{ex} = 394 nm, background electrolyte 0.01 mol·L^{-1} $NaClO_4$.

4. Research achievements during the project period

Publications

- J. Schott, J. Kretzschmar, M. Acker, S. Eidner, M.U. Kumke, B. Drobot, A. Barkleit, S. Taut, V. Brendler, Th. Stumpf, "Formation of a Eu(III) borate solid species from a weak Eu(III) borate complex in aqueous solution", *Dalton Transactions* 43(30), 11516-11528 (2014).
- A. Demetriou , I. Pashalidis , A.V. Nicolaides, M.U. Kumke, "Surface mechanism of the boron adsorption on alumina in aqueous solutions", *Desalination and Water Treatment* 51(31-33), 6130-6136 (2013).
- H. Lippold, S. Eidner, M.U. Kumke, J. Lippmann-Pipke, "Diffusion, degradation or on-site stabilisation – Identifying causes of kinetic processes involved in metal-humate complexation", *Applied Geochemistry* 27, 250-256 (2012).
- P.-A. Primus, M.U. Kumke, "Flash Photolysis Study of Complexes between Salicylic Acid and Lanthanide Ions in Water", *Journal of Physical Chemistry A* 116(4), 1176-1182 (2012).
- Th. Schäfer, F. Huber, H. Seher, T. Missana, U. Alonso, M.U. Kumke, S. Eidner, F. Claret, F. Enzmann, "Nanoparticles and their influence on radionuclide mobility in deep geological formations", *Applied Geochemistry* 27, 390-403 (2012).
- S. Antoniou, I. Pashalidis, A. Gessner, M. U. Kumke, "The effect of humic acid on the formation and solubility of secondary solid phases ($Nd(OH)CO_3$ and $Sm(OH)CO_3$)", *Radiochimica Acta* 99(4), 217-223 (2011).
- S. Antoniou, I. Pashalidis, A. Gessner, M.U. Kumke, "Spectroscopic investigations on the effect of humic acid on the formation and solubility of secondary solid phases of $Ln_2(CO_3)_3$", *Journal of Rare Earth* 29, 516-521 (2011).

PhD Thesis

- Bettina Marmodée, "Fluorescence Line-Narrowing-Spektroskopie zur Charakterisierung von Eu(III) in Komplexen mit kleinen organischen Liganden", Dissertation, Universität Potsdam (2012).
- Stefanie Kuke, "Lanthanoide(III) in Komplexen mit niedermolekularen Säuren – Spektroskopische Betrachtung komplex-spezifischer Löschmechanismen in Eu(III)- und Tb(III)-Komplexen", Dissertation, Universität Potsdam (2013).

Bachelor, Diploma and Master Thesis

- Christina Schimmeck (2011, Bachelorarbeit) "Lumineszenzspektroskopische Charakterisierung von Tropolon und substituierten Benzoesäuren in Komplexen mit Europium.
- Marian Süßmann (2012, Bachelorarbeit) "Einfluss von Temperatur und Ionenstärke auf die Komplexierung von Europium(III) mit Huminstoffen."

- Melissa-Jane Monks (2012, Bachelorarbeit) „Lumineszenz-basierte Speziation von Europium(III)-Borat-Komplexen“
- Madlen Rühlmann (2013, Bachelorarbeit) "Einfluss der Ionenstärke und des pH-Wertes auf die Konformation von Polymeren."

- Max L. Schütte (2014, Bachelorarbeit) "Lumineszenzspektroskopische Untersuchung der Europium-Huminstoff-Wechselwirkung in Abhängigkeit der Elektrolytzusammensetzung."
- Michel Wehrhold (2014, Bachelorarbeit) "Lumineszenzuntersuchungen an Uranyl-Acetat-Proben."
- Manuela Haupt (2012, Diplomarbeit) "Speziation niedermolekularer Säuren in Gegenwart von Eu(III) und Mineralphasen mittels Raman-Spektroskopie."
- Julia Prinz (2013, Masterarbeit) "Untersuchung der Sorption von organischen Substanzen an Alumosilikat-Modelloberflächen mittels Schwingungsspektroskopie."
- Katja Burek (2014, Diplomarbeit) "Temperatur- und Ionenstärke-Einflüsse auf die Lumineszenz von Lanthanoiden in Komplexen mit niedermolekularen organischen Liganden."
- Tobias Garling (2015, Masterarbeit) "Untersuchung der Sorption von niedermolekularen organischen Stoffen an Mineraloberflächen mittels SFG-Spektroskopie."

References

1. BGR. *Endlagerung radioaktiver Abfälle in Deutschland - Untersuchung und Bewertung von Regionen mit potenziell geeigneten Wirtsgesteinsformationen*. (2007).
2. Clay Mineral Society. *http://www.clays.org/SOURCE%20CLAYS/SCdata.html* , last access on 5th December 2015
3. Cheng, H., Liu, Q., Yang, J., Du, X. & Frost, R. L. Influencing factors on kaolinite–potassium acetate intercalation complexes. *Appl. Clay Sci.* **50,** 476–480 (2010).
4. Li, Y., Sun, D., Pan, X. & Zhang, B. Kaolinite intercalation precursors. *Clays Clay Miner.* **57,** 779–786 (2009).
5. Kimura, T., Nagaishi, R., Kato, Y. & Yoshida, Z. Luminescence study on solvation of americium(III), curium(III) and several lanthanide(III) ions in nonaqueous and binary mixed solvents. *Radiochim. Acta* **89,** 125–130 (2001).
6. Carnall, W. T. in *Handbook on the Physics and Chemistry of Rare Earth* (1979).
7. Horrocks, W. D. & Sudnick, D. R. Lanthanide ion luminescence probes of the structure of biological macromolecules. *Acc. Chem. Res.* **14,** 384–392 (1981).
8. Ryan, D. K. & Weber, J. H. Copper(II) complexing capacities of natural waters by fluorescence quenching. *Environ. Sci. Technol.* **16,** 866–872 (1982).
9. Ryan, D. K. & Weber, J. H. Fluorescence quenching titration for determination of complexing capacities and stability constants of fulvic acid. *Anal. Chem.* **54,** 986–990 (1982).
10. IHSS. http://www.humicsubstances.org/acidity.html.
11. Lambert, A. G., Davies, P. B. & Neivandt, D. J. Implementing the Theory of Sum Frequency Generation Vibrational Spectroscopy: A Tutorial Review. *Appl. Spectrosc. Rev.* **40,** 103–145 (2005).
12. Richmond, G. L. Molecular bonding and interactions at aqueous surfaces as probed by vibrational sum frequency spectroscopy. *Chem. Rev.* **102,** 2693–2724 (2002).
13. Demtröder, W. *Laser Spectroscopy 1*. (2014). doi:10.1007/978-3-642-53859-9
14. D'Aléo, A., Pointillart, F., Ouahab, L., Andraud, C. & Maury, O. Charge transfer excited states sensitization of lanthanide emitting from the visible to the near-infra-red. *Coord. Chem. Rev.* **256,** 1604–1620 (2012).
15. Carnall, W. T. Spectral Intensities of the Trivalent Lanthanides and Actinides in Solution. II. Pm3+, Sm3+, Eu3+, Gd3+, Tb3+, Dy3+, and Ho3+. *J. Chem. Phys.* **49,** 4412 (1968).
16. W. T. Carnell, J. V. Beitz, H. Crosswhite, K. Rajnak, J. B. M. in *Systematics and the Properties of the Lanthanides* (ed. Sinha, S. P.) 389 – 450 (D. Reidel Publishing Company, 1983).
17. Stein, G. Energy gap law in the solvent isotope effect on radiationless transitions of rare earth ions. *J. Chem. Phys.* **62,** 208 (1975).
18. Arnaud, N. & Georges, J. Influence of pH, surfactant and synergic agent on the

luminescent properties of terbium chelated with benzoic acid derivatives in aqueous solutions. *Analyst* **125,** 1487–1490 (2000).

19. Panak, P., Klenze, R., Kim, J. I. & Wimmer, H. A study of intramolecular energy transfer in Cm(III) complexes with aromatic ligands by time-resolved laser fluorescence spectroscopy. *J. Alloys Compd.* **225,** 261–266 (1995).

20. Primus, P.-A. & Kumke, M. U. Flash Photolysis Study of Complexes between Salicylic Acid and Lanthanide Ions in Water. *J. Phys. Chem. A* **116,** 1176–1182 (2012).

21. Kuke, S., Marmodée, B., Eidner, S., Schilde, U. & Kumke, M. U. Intramolecular deactivation processes in complexes of salicylic acid or glycolic acid with Eu(III). *Spectrochim. Acta. A. Mol. Biomol. Spectrosc.* **75,** 1333–40 (2010).

22. Martell, A. E. & Smith, R. M. *Critical Stability Constants, Vol. 3: Other Organic Ligands*. (1989).

23. Müller, B. ChemEQL: http://www.eawag.ch/en/department/surf/projects/chemeql/.

24. Schott, J. *et al.* Formation of a Eu(III) borate solid species from a weak Eu(III) borate complex in aqueous solution. *Dalton Trans.* **43,** 11516–28 (2014).

25. Brasser, T. & Brewitz, W. Anwendbarkeit der Indikatoren 'teufenabhängige Mineralisation / Salzgehalt' für die Erfüllung der allgemeinen Anforderung 'keine oder langsame Grundwasserbewegung'. *Bericht an den AKEnd* **GRS-A-2956,** (2002).

26. Görller-Walrand, C. & Binnemans, K. in *Handbook on Physics and Chemistry of Rare Earth* (eds. K. A. Gschneidner, J. & Eyring, L.) **23,** (Elsevier Science B.V., 1996).

27. Milne, C. J., Kinniburgh, D. G., van Riemsdijk, W. H. & Tipping, E. Generic NICA-Donnan Model Parameters for Metal-Ion Binding by Humic Substances. *Environ. Sci. Technol.* **37,** 958–971 (2003).

28. Milne, C. J., Kinniburgh, D. G. & Tipping, E. Generic NICA-Donnan Model Parameters for Proton Binding by Humic Substances. *Environ. Sci. Technol.* **35,** 2049–2059 (2001).

29. Marang, L., Eidner, S., Kumke, M. U., Benedetti, M. F. & Reiller, P. E. Spectroscopic characterization of the competitive binding of Eu(III), Ca(II), and Cu(II) to a sedimentary originated humic acid. *Chem. Geol.* **264,** 154–161 (2009).

30. Marang, L., Reiller, P. E., Eidner, S., Kumke, M. U. & Benedetti, M. F. Combining Spectroscopic and Potentiometric Approaches to Characterize Competitive Binding to Humic Substances. *Environ. Sci. Technol.* **42,** 5094–5098 (2008).

31. Blume, H.-P. *et al. Scheffer/Schachtschabel: Lehrbuch der Bodenkunde*. (2010).

32. in *KIT Scientific Report 7633* (ed. Marquardt, C.) (2013).

33. Tcherkasskaya, O., Ni, S. & Winnik, M. A. Direct Energy Transfer Studies of the Domain-Boundary Interface in Polyisoprene-Poly(methyl methacrylate) Block Copolymer Films. *Macromolecules* **29,** 610–616 (1996).

34. Frost, R. L. & Kloprogge, J. T. Towards a single crystal Raman spectrum of kaolinite at 77 K. *Spectrochim. Acta Part A Mol. Biomol. Spectrosc.* **57,** 163–175 (2001).

35. Rouxhet, P. G., Samudacheata, N., Jacobs, H. & Anton, O. Attribution of the OH stretching bands of kaolinite. *Clay Miner.* **12,** 171–179 (1977).

36. Shoval, S. Hydroxyl-Stretching Bands ‘A’ and ‘Z’ in Raman and Infrared Spectra of Kaolinites. *Clay Miner.* **34,** 551–563 (1999).

37. Ledoux, R. . L. & White, J. L. Infrared study of the OH groups in expanded kaolinite. *Science* **143,** 244–5 (1964).

38. Frost, R. L., Kristof, J., Horváth, E. & Kloprogge, J. T. Raman spectroscopy of potassium acetate-intercalated kaolinites over the temperature range 25-300 °C. *J. Raman Spectrosc.* **32,** 271–277 (2001).

39. Wang, W.-M., Yeh, H.-W., Chen, P.-Y. & Wang, M.-K. Kaolin Mineralogy of Clays in Paleosol Profiles on the Late-Miocene Sediments in Penghu Islands (Pescadores), Taiwan. *Clays Clay Miner.* **46,** 1–9 (1998).

40. Cruz, M. D. R. & Duro, F. I. F. New data on the kaolinite-potassium acetate complex. *Clay Miner.* **34,** 565–577 (1999).

41. Sugahara, Y., Satokawa, S., Kuroda, K. & Kato, C. Kaolinite-Pyridine Intercalation Compound derived from Hydrated Kaolinite. *Clays Clay Miner.* **37,** 143–150 (1989).

42. Gardolinski, J., Peralta-Zamora, P. & Wypych, F. Preparation and Characterization of a Kaolinite-1-methyl-2-Pyrrolidone Intercalation Compound. *J. Colloid Interface Sci.* **211,** 137–141 (1999).

43. Frost, R. L., Kristof, J., Horvath, E. & Kloprogge, J. T. Deintercalation of dimethylsulphoxide intercalated kaolinites - a DTA/TGA and Raman spectroscopic study. *Thermochim. Acta* **327,** 155–166 (1999).

44. Frost, R. L., Kloprogge, J. T., Kristof, J. & Horvath, E. Deintercalation of Hydrazine-Intercalated Low-Defect Kaolinite. *Clays Clay Miner.* **47,** 732–741 (1999).

45. Cassanas, G., Morssli, M., Fabrègue, E. & Bardet, L. Etude Spectrale de l’Acide Glycolique, des Glycolates et du Processue de Polymérisation. *J. Raman Spectrosc.* **22,** 11–17 (1991).

46. Choppin, G. R. & Friedman, H. G. Complexes of Trivalent Lanthanide Ions. III. Bidentate Chelates. *Inorg. Chem.* **5,** 1599–1603 (1966).

47. Wood, S. A. The aqueous geochemistry of the rare-earth elements: Critical stability constants for complexes with simple carboxcylic acids at 25°C and 1 bar and their application to nuclear waste management. *Eng. Geol.* **34,** 229 – 259 (1993).

48. GAUSSIAN 09, Revision A.02, Gaussian Inc., Wallingford CT. (2009).

Supporting Information

Table 1S: Stability constants for Ln(III)-complexes with salicylic acid and Phthalic acid (RT, I = 0 mol·L^{-1}).[46,47]

Ligand	ML_1	ML_2
Tb(III) salicylic acid	2.38	4.75
Tb(III) phthalic acid	4.83	6.96
Sm(III) salicylic acid	2.49	4.71
Sm(III) phthalic acid	5.16	7.39
Dy(III) salicylic acid	2.13	4.65
Dy(III) phthalic acid	4.97	6.75
Eu(III) salicylic acid	2.45	4.73
Eu(III) phthalic acid	3.45	5.17

Table 2S: With ChemEQL 3.1[23] **calculated species distribution (RT, I = 0 mol·L^{-1}).**

	Ln(III) aquo complex / %	Ln(III)-L_1 / %	Ln(III)-L_2 / %
Tb(III) salicylic acid	36	41	23
Tb(III) phthalic acid	4	92	4
Sm(II) salicylic acid	30	41	29
Sm(II) phthalic acid	3	94	3
Dy(III) salicylic acid	41	24	35
Dy(III) phthalic acid	2	95	3
Eu(III) salicylic acid	3	17	80
Eu(III) phthalic acid	1	43	56

Table 3S: pK_a values of model ligands.[47]

Model ligand	p$K_{a\,(1)}$	p$K_{a\,(2)}$
Salicylic acid	2.97	13.74
Phthalic acid	2.89	4.68

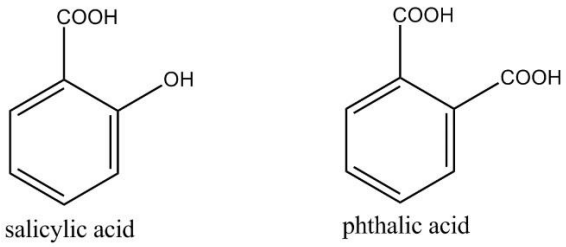

salicylic acid phthalic acid

Figure 1S: structure of model ligands investigated.

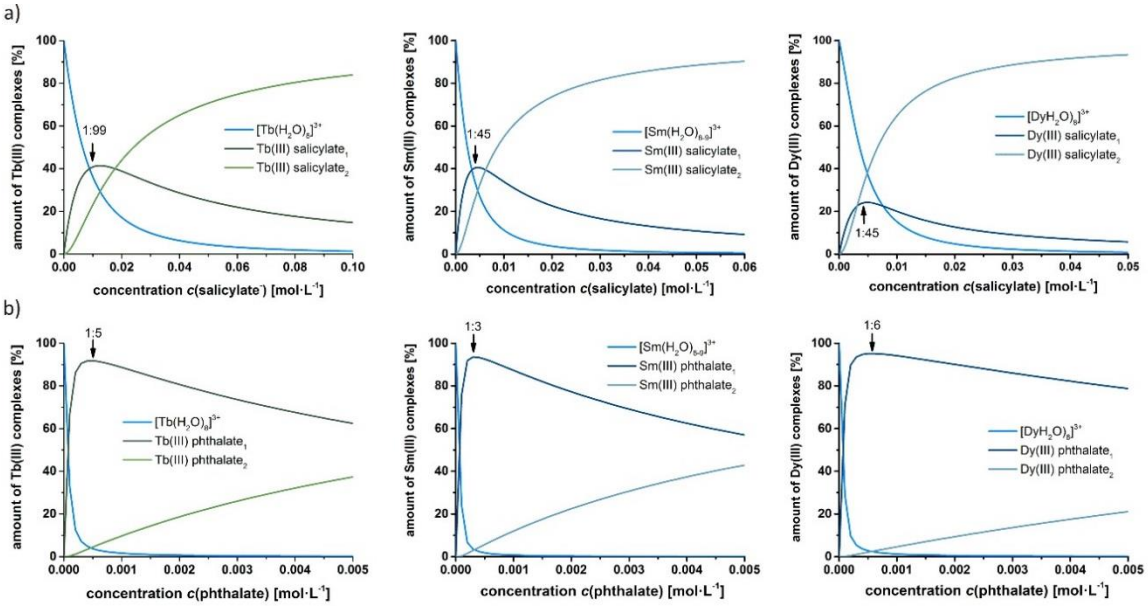

Figure 2S: speciation diagrams of Tb(III), Sm(III) and Dy(III) ($c_{Ln(III)}$ = 10^{-4} mol·L^{-1}) in complexes with a) salicylic acid (p*H* = 5.0) and b) phthalic acid (p*H* = 4.2) (RT, *I* = 0 mol·L^{-1}) (calculated with ChemEQL 3.1[23], stabilitiy constants taken from[47]).

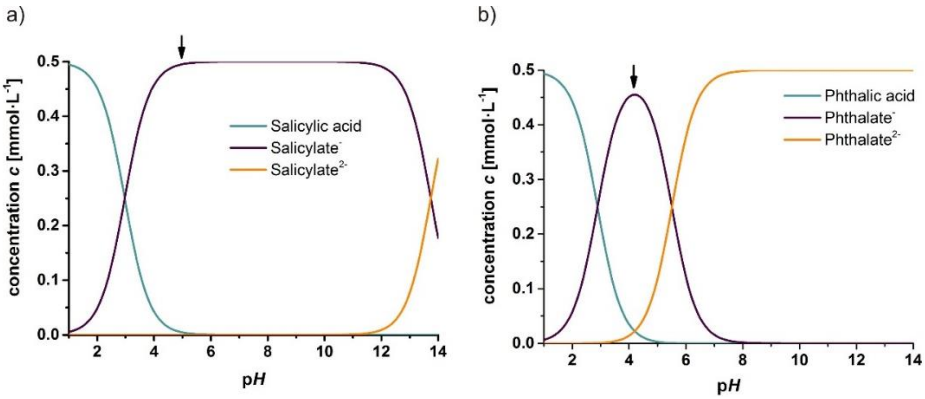

Figure 3S: speciation diagrams of a) salicylic acid and b) phthalic acid (calculaterd with ChemEQL 3.1[23], p*K*a values taken from[47]).

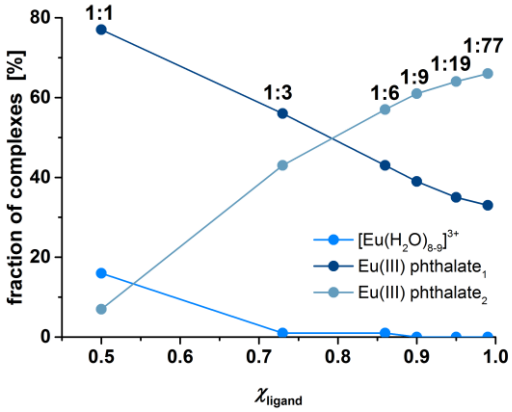

Figure 4S: speciation diagram of Eu(III) in complexes phthalic acid (p*H* = 5.0) (RT, *I* = 0 mol·L^{-1}) (calculated with ChemEGL 3.1[23], stability constants taken from[47]).

Berichtsblatt

1. ISBN oder ISSN Noch nicht bekannt	2. Berichtsart (Schlussbericht oder Veröffentlichung) Schlussbericht

3. Titel

Zum Molekularen Prozessverständnis der Wechselwirkungen von Lanthanoiden mit Komponenten homogener und heterogener salinarer Systeme

4. Autor(en) [Name(n), Vorname(n)]	5. Abschlussdatum des Vorhabens 30.6.2015
K. Brennenstuhl, K. Burek, S. Eidner, M.U. Kumke	6. Veröffentlichungsdatum Eingereicht zur Veröffentlichung
	7. Form der Publikation Forschungsbericht
8. Durchführende Institution(en) (Name, Adresse) Universität Potsdam, Institut für Chemie (Physikalische Chemie) Karl-Liebknecht-Str. 24-25 14476 Potsdam-Golm	9. Ber. Nr. Durchführende Institution nicht bekannt
	10. Förderkennzeichen *) 02E11011
	11. Seitenzahl 68
13. Fördernde Institution (Name, Adresse) Bundesministerium für Wirtschaft und Energie (davor Bundesministerium für Wirtschaft und Technologie) (BMWi) 11019 Berlin	12. Literaturangaben 48
	14. Tabellen 14
	15. Abbildungen 49

16. Zusätzliche Angaben
-

17. Vorgelegt bei (Titel, Ort, Datum)
-

18. Kurzfassung

Europium(III), Terbium(III), Samarium(III) und Dysprosium(III) wie auch Neodym(III) und Holmium(III) wurden als Lumineszenzsonden in Komplexen mit niedermolekularen organischen Verbindungen, Polymeren und Huminstoffen detailliert untersucht, wobei Ionenstärken bis I = 4 M und Temperaturen bis T = 353 K untersucht wurden. Dabei wurden die Liganden-bezogenen strahlungslosen Deaktivierungsprozesse (Energietransfer auf OH-Schwingungen oder Liganden-Triplettzustand) wie auch photoinduzierte Redoxreaktionen als effektive Löschmechanismen identifiziert. Aus der mechanistisch exakten Beschreibung der Lumineszenzlöschprozesse in Lanthanoid-Komplexen kann eine differenziertere Speziation abgeleitet werden. Lumineszenzuntersuchungen am (Poly)Borat zeigten eine schwache Komplexierung, so dass (Poly)Borat als kein effizienter Ligand in einem möglichen Endlager angesehen werden kann. Raman-Mikroskopie und Summen-Frequenz-Erzeugung wurden für die Untersuchung von Mineraloberflächen eingesetzt. Die Sorption und Interkalation von vor allem niedermolekularen Verbindungen wie z.B. Acetat und Metallionen wurden so charakterisiert. Des Weiteren wurden Arbeiten zur konfokalen Lasermikroskopie mit Eu(III) an Diffusionsproben ausgeführt.

Schlagwörter
Zeit- und spektral hochaufgelöste Laserspektroskopie, Lumineszenz, Lanthanoide, Huminstoffe, Modellliganden, Prozessverständnis, Ionenstärke, Methodenentwicklung

20. Verlag	21. Preis
Wissenschaftliche Berichte des KIT	nicht bekannt

*) Auf das Förderkennzeichen des BMBF soll auch in der Veröffentlichung hingewiesen werden.

Document Control Sheet

1. ISBN or ISSN	2. type of document (e.g. report, publication)
not known	Report

3.

Molecular process understanding of interactions between Lanthanide ions and components of homogeneous as well as heterogeneous saline systems.

4. author(s) (family name, first name(s))	5.end of project
K. Brennenstuhl, K. Burek, S. Eidner, M.U. Kumke	30.6.2015
	6. publication date submitted for publication
	7. form of publication scientific report
8. performing organization(s) (name, address) University of Potsdam, Institute of Chemistry (Physical Chemistry) Karl-Liebknecht-Str. 24-25 14476 Potsdam-Golm	9. originator's report no. not known
	10. reference no. 02E11011
	11. no. of pages 68
13. sponsoring agency (name, address) Federal Ministry for Economic Affairs and Energy (BMWi) 11019 Berlin	12. no. of references 48
	14. no. of tables 14
	15. no. of figures 49

16. supplementary notes
-

17. presented at (title, place, date)
-

18. abstract
Different lanthanides (Ln(III)) like Europium(III), Terbium(III), Samarium(III) or Dysprosium(III) were used as luminescence probes in complexes with low molecular weight organic compounds, polymers, and humic substances. The experiments were performed at ionic strength up to I = 4 M and temperatures up to T = 353 K. For the Ln(III) complexes the different ligand-related radiationless deactivation pathways were carefully evaluated for contributions of OH-vibrations, ligand triplet state, and photoinduced electron transfer. From the improved understanding of deactivation processes an improved speciation analysis can be developed. The complexation of Europium(III) by (poly)borates was further investigated, especially at cryogenic conditions under site-selective excitation conditions. It could be shown that complexes with (poly)borates are relatively weak and will play no crucial role in the environment of a potential repository. The surface of minerals and the interaction with organics was characterized using Raman microscopy and sum frequency generation. It could be shown that low molecular weight organic compounds can form intercalation complexes with minerals. Confocal laser scanning microscopy in combination with Europium(III) as luminescence probe was used to monitor metal ion diffusion in mineral cores.

19. keywords
Time and spectral highly resolved laser spectroscopy, luminescence, lanthanides, humic substances, model ligands, process understanding, ionic strength, development of analytical tools

20. publisher	21. price
KIT scientific reports	not known